

SMARTS Optical and infrared monitoring of 12 gamma-ray bright blazars

E. W. Bonning¹, C. M. Urry¹, C. Bailyn², M. Buxton², R. Chatterjee², P. Coppi², G. Fossati⁴, J. Isler¹, L. Maraschi³

ABSTRACT

We present multiwavelength data for twelve blazars observed from 2008-2010 as part of an ongoing optical-infrared photometric monitoring project. Sources were selected to be bright, southern ($\delta < 20^\circ$) blazars observed by the *Fermi* Gamma-Ray Space Telescope, with daily and weekly gamma-ray fluxes made available from the start of the *Fermi* mission. Light curves are presented for the twelve blazars in BVRJK (0.4 to 2.2 μm) at near-daily cadence. We find that optical and infrared fluxes are well correlated in all sources, with no measured lag between bands. Gamma-ray bright flat spectrum radio quasars (FSRQs) in our sample have optical/infrared emission correlated with gamma-rays consistent with inverse Compton-scattering leptonic models for GeV emission. In FSRQs, the variability amplitude decreases towards optical/IR wavelengths, consistent with the presence of a thermal emission component from the accretion disk varying on significantly longer timescales than the jet synchrotron emission. In BL Lac objects, variability is mainly constant across wavelengths, consistent with a weak or radiatively inefficient disk. Also consistent with this picture, FSRQs have redder optical-infrared colors when they are brighter, while BL Lac objects show no such trend. Several objects show complicated color-magnitude behavior: AO 0235+164 appears in two different states depending on whether it is gamma-ray bright or not. OJ 287 and 3C 279 show some hysteresis tracks in their

¹Department of Physics and Yale Center for Astronomy and Astrophysics, Yale University, PO Box 208121, New Haven, CT 06520-8120; erin.bonning@yale.edu

²Department of Astronomy and Yale Center for Astronomy and Astrophysics, Yale University, PO Box 208101, New Haven, CT 06520-8101

³INAF - Osservatorio Astronomico di Brera, V. Brera 28, I-20100 Milano, Italy

⁴Department of Physics and Astronomy, Rice University, Houston, TX 77005

color-magnitude diagrams. Individual flares may be achromatic or otherwise depart from the trend, suggesting different jet components becoming important at different times. We present a time-dependent spectral energy distribution of the bright FSRQ 3C 454.3 during December 2009 flare, which is well fit by an external Compton model in the bright state, although day to day changes in the course of the flare pose challenges to a simple one-zone model. All data from the SMARTS monitoring program are publicly available on our website.

Subject headings: galaxies: active — quasars: general — black hole physics — BL Lacertae objects

1. Introduction

Blazars form a sub-class of active galactic nuclei (AGN) with a bright, relativistic jet viewed closely along our line of sight (Urry & Padovani 1995). Blazars are often very luminous and violently variable over a large range of wave bands from radio to gamma-rays. Spectral energy distributions (SEDs) of blazars are characterized by two broad components: one peaking anywhere from infrared to X-ray frequencies, and a second peak at higher energies, from hard X-rays to TeV gamma-rays. The radio to optical/UV emission in blazars is interpreted as synchrotron radiation by the energetic electrons in the jet (Konigl 1981; Urry & Mushotzky 1982) while the mechanism of the high energy emission (i.e., X-rays and gamma-rays) is less certain. It may be due to the inverse-Compton scattering of seed photons by the same relativistic electrons responsible for the synchrotron radiation (the so-called leptonic models; e.g. Böttcher 2007) or due to synchrotron radiation of protons co-accelerated with the electrons in the jet, interactions of these highly relativistic protons with external radiation fields, or proton-induced particle cascades (hadronic models; e.g. Mücke & Protheroe 2001; Mücke et al. 2003).

Both leptonic and hadronic models can successfully explain the SEDs observed so far, but they have very different implications for the kinetic power of the jet and hence how it is produced and its influence on its environment. In the case of leptonic models, the low-energy seed photons may be the synchrotron photons produced within the jet (synchrotron self-Compton, or SSC; Jones et al. 1974) or thermal emission from outside the jet. External Compton (EC) scenarios produce high energy emission from upscattering photons from the accretion disk, broad line region (BLR), or dusty torus (Sikora et al. 1994; Dermer & Schlickeiser 1993; Ghisellini & Madau 1996; Tavecchio et al. 2000; Ghisellini & Celotti 2001). The jet plasma may consist of electrons and protons, electrons and positrons, or a combination of the two (Ghisellini & Tavecchio 2010; Sikora & Madejski 2000).

Knowing the composition of the jet is necessary to deduce its kinetic power, which in turn reflects how it is launched, accelerated, and collimated. Studying the SED and its variation with time allows us to determine the radiation mechanism, and thus the physical parameters of the emission region, such as the magnetic field, particle number density, and bulk velocity of the plasma.

Until recently, blazar SED studies occurred primarily when the brightness of a blazar significantly increased in one or multiple wave bands. Due to the difficulty of coordinating large multiwavelength campaigns, data in other wavebands were often non-simultaneous. The near-continuous monitoring activity of the Large Area Telescope (LAT) instrument on board the *Fermi Gamma-Ray Space Telescope*, launched in 2008, provides the opportunity to study the variable SEDs of a large sample of blazars with truly simultaneous multi-frequency data. Although many blazars radiate most of their energy in the gamma-ray band, it is the characterization of both broad components of the blazar SEDs and their relative variation with time that allows us to infer the physics of these sources. Specifically, correlations between variations in gamma-ray flux and those at lower energies are useful indicators of the relative locations of emission regions and the radiation mechanism(s).

Fermi/LAT provides regular and well sampled gamma-ray light curves of a large sample of blazars. Obtaining the same quality data at optical and infrared wavelengths is equally important. We use the meter-class telescopes of the Small and Moderate Aperture Research Telescope System (SMARTS) to carry out photometric monitoring of bright southern gamma-ray blazars on a regular cadence, at both optical and near-infrared wavelengths.

In this paper, we report on the Yale/SMARTS blazar monitoring program for the years 2008-2010. We present light curves for the blazars with the greatest coverage, and refer the reader to our website⁵ for the full data set. In addition, we report on gamma-ray/optical-IR cross-correlation functions for several blazars and show an example of how a variable SED has the potential to constrain the physics of a jet and/or accretion disk. Finally, we discuss the color-magnitude diagrams for blazars and how these can yield broad inferences about particle acceleration and radiative losses in blazar jets.

In § 2 we present the sample selection and data reduction and present the multi-wavelength light curves. In § 3, we discuss the variability characteristics of the blazars in our sample, including cross-correlations between gamma-ray and optical-IR variations, frequency-dependent variability amplitude, and color-magnitude relations for our sample of blazars. We discuss SED fits for a sample blazar flare in § 5. In § 6 we present the summary and conclusions.

⁵<http://www.astro.yale.edu/smarts/fermi>

2. Sample Selection and Data Analysis

The SMARTS blazar sample was initially (in 2008) defined to include all LAT-monitored blazars on the initial public release list with declination $< 20^\circ$. Prior to the launch of Fermi, the list of sources which were to have fluxes made publicly available consisted mainly of bright blazars observed by EGRET. Additional sources were added to our monitoring campaign as they were added to the public LAT source list or were the target of a multi-wavelength campaign. We observed the twelve sources presented here with a cadence of approximately once every three days. Brighter or flaring sources were observed nightly. The SMARTS source list, including positions, redshifts, and observation timeframe, is given in Table 1. Each of the blazars is identified by its spectral class: flat-spectrum radio quasar (FSRQ), low frequency-peaked BL Lac object (LBL), or high frequency-peaked BL Lac (HBL). These form a rough sequence of decreasing continuum luminosity and emission line luminosity (Fossati et al. 1998). The most luminous blazars (FSRQ and LBL) have their synchrotron peak at IR/optical wavelengths and the inverse Compton peak in GeV gamma-rays so they form the bulk of our monitored sample.

The 12 blazars were observed with the SMARTS 1.3m telescope and ANDICAM instrument (DePoy et al. 2003). ANDICAM is a dual-channel imager with a dichroic that feeds an optical CCD and an IR imager, which can obtain simultaneous data from 0.4 to 2.2 μm . Observations were taken in B, V, R, J, and K bands, except for two sources: PKS 0528+134 and 3C 273, for which K-band images were not obtained. The former was below the K-band detection limit; the latter, being very bright, had very short exposure times in optical bands. Since IR images are taken simultaneously with optical, there was only sufficient time for J-band images to be obtained for 3C 273. Additionally, spectra were obtained for a number of the brighter sources, using the SMARTS RCSPEC+1.5-meter telescope. These data will be discussed in forthcoming paper (Isler et al. *in prep*).

Optical data were bias-subtracted, overscan-subtracted, and flat fielded using the CCD-PROC task in IRAF. Infrared data were sky-subtracted, flat fielded, and dithered images combined using in-house IRAF scripts. Slight blemishes reflecting the dither pattern are apparent in the final images, but introduce at most a 0.1% photometric error.

Optical and infrared aperture photometry was performed using the PHOT task in IRAF. Non-variable comparison stars with comparable magnitude to the blazar were chosen in each field. The raw photometry of comparison stars in the field of the blazar was calibrated using photometric zeropoints that were measured from ANDICAM observations during 2008-2009 of optical (Landolt 1992) and near-infrared (Persson et al. 1998) primary standards for each filter, correcting for atmospheric extinction derived from all the standards taken together. The number of photometric nights available for the calibration for each field and each filter

differs, but ranges from 40-128 nights in the optical, and 13-98 nights for the near-infrared. The average of the comparison stars was used as a basis of differential photometry with respect to the blazar for all observations.

We compared our calibrated comparison star magnitudes to values reported in the literature where available. In the large majority of cases, our values agree with previous photometric sequences measured for these fields to within a typical $1\text{-}\sigma$ error of ~ 0.05 mag with an occasional discrepancy of ~ 0.1 mag. Our optical magnitudes for the comparison stars in the field of AO 0235+164 are consistent with values reported by Smith et al. (1985), Fiorucci et al. (1998), and González-Pérez et al. (2001). In the field of PKS 0528+134, our comparison star magnitudes match extremely well with those published by González-Pérez et al. (2001) with the exception of V -band for star 1, where we differ by 0.1 mag. When compared to the values published by Raiteri et al. (1998), we agree in R -band; however our B and V magnitudes are fainter by 0.1 mag in B and 0.2 mag in V compared to those of Raiteri et al. In the case of OJ 287, our comparison stars are in good agreement with González-Pérez et al., with the largest discrepancy being ~ 0.07 mag. Likewise, our V and R measurements for the comparison stars for OJ 287 are in close agreement with those measured by Fiorucci & Tosti (1996, who do not report B -band.) The comparison star of 3C 273 is within uncertainties reported by Smith et al. (1985). 3C 279 is in close agreement with the values published by Smith & Balonek (1998) with R -band being the only one to differ by more than $3\text{-}\sigma$ (0.1 mag). Our comparison stars for PKS 1510-089 generally agreed within the uncertainties with the values published by González-Pérez et al. (2001), with the exception of B -band for our star 1, which differed by 0.1 mag. In the field of PKS 1622-297, our stars 1 and 2 are stars 10 and 14 of González-Pérez et al. (2001), and they are in excellent agreement in V and R band. (González-Pérez et al. do not report B -band for this source). The comparison star in our field for PKS 2155-304 is in excellent agreement with the photometry of Hamuy & Maza (1989). In the case of 3C 454.3, comparison star magnitudes have been reported for this well-studied source also by Angione (1971) and Fiorucci et al. (1998). We agree extremely well with the results of Fiorucci et al. (1998) in V and R , and again find a ~ 0.1 mag (fainter) discrepancy with Raiteri et al. (1998) in B , a discrepancy which only occurs for some stars reported by Angione (1971).

In general, we find that in those sources with multiple photometric sequences available (PKS1510-089, 3C 273, 3C 454.3), published comparison star values frequently differ on the level of ~ 0.1 magnitude. This is consistent with a comparison of our data to the literature. For our remaining sources, PKS 0208-512, PKS 1406-076, and PKS 1730-130, existing photometric values for comparison stars (given, for example, by the finding charts at <http://www.lsw.uni-heidelberg.de/projects/extragalactic/charts>) are taken from the USNO B1.0 catalog (Monet et al. 2003). Our calibrated magnitudes are generally fainter than

USNO by 0.2-0.4 mag. The USNO B1.0 catalog was designed to be a proper-motion catalog. Although photometry was obtained, it has an accuracy of 0.3 mag (Monet et al. 2003) which is significantly greater than the errors found for our photometry.

The optical and IR light curves for the monitored blazars through July 2010 are shown in Figure 1. (At the time of writing, some third-year SMARTS data are already available online but the basic scientific results do not change for the 12 blazars discussed here.) These figures include daily and weekly gamma-ray fluxes from the *Fermi*/LAT public light curves for those sources bright enough in the gamma-ray that these are measureable⁶. The optical and infrared light curves and calibrated magnitudes are available online at the Yale SMARTS Blazar site⁵. Optical and infrared finding charts are shown in Appendices A and B. Calibrated magnitudes for the comparison stars in each blazar field are given in Appendix C.

The error in calibrating the secondary star magnitudes was found by calculating the 1- σ standard error of the mean over the number of photometric nights mentioned above. Results that were greater than $\pm 3\sigma$ from the mean were rejected and the mean and σ were recalculated. This procedure was repeated until no more rejections were made. The resulting errors are given in Tables C.1. and C.2. These errors do not account for systematic errors associated with effects such as the difference in effective filter responses between SMARTS and the standard system. Such systematics are likely to contribute a few hundredths of a magnitude of calibration error.

Previous work with SMARTS photometry (Buxton et al. 2011, *submitted*) has led to an understanding of the errors in differential photometry for point sources as a function of count rate. Based on this work, we find errors as low as 0.01 magnitudes in the optical and 0.02 magnitudes in the IR for bright sources (<16 mag in the optical and <13 mag in IR), and up to ten times that for sources near the detection limit, which varies depending on the exposure time. We note that these errors are random errors in the individual points, rather than systematic offsets in the magnitude system, as is the case for the calibration errors.

⁶List of *Fermi*/LAT monitored sources is at <http://fermi.gsfc.nasa.gov/ssc/data/access/lat/msl1c/>

⁷<http://ned.ipac.caltech.edu/> The NASA/IPAC Extragalactic Database (NED) is operated by the Jet Propulsion Laboratory, California Institute of Technology, under contract with the National Aeronautics and Space Administration.

Name	R.A. & Dec. (J2000)		Class	z	Dates
	[h:m:s]	[d:m:s]			(MJD)
PKS 0208–512	02:10:46.2	–51:01:01	FSRQ	1.003	54640 – 55282
AO 0235+16	02:38:38.9	+16:36:59	LBL	0.940	54662 – 55487
PKS 0528+134	05:30:56.4	+13:31:55	FSRQ	2.060	54701 – 55511
OJ 287	08:54:48.8	+20:06:31	LBL	0.306	54777 – 55500
3C 273	12:29:06.7	+02:03:09	FSRQ	0.158	54603 – 55412
3C 279	12:56:11.1	–05:47:21	FSRQ	0.536	54603 – 55416
PKS 1406–076	14:08:56.5	–07:52:27	FSRQ	1.494	54501 – 55385
PKS 1510–08	15:12:50.5	–09:06:00	FSRQ	0.360	54603 – 55464
PKS 1622–29	16:26:06.0	–29:51:27	FSRQ	0.815	54501 – 55481
PKS 1730–130	17:33:02.6	–13:04:49	FSRQ	0.902	54603 – 55494
PKS 2155–304	21:58:52.0	–30:13:32	HBL	0.112	54603 – 55557
3C 454.3	22:53:57.7	+16:08:54	FSRQ	0.859	54640 – 55545

Table 1:: The SMARTS blazar sample. Coordinates and redshifts from NED⁷. Dates indicate limits of R -band observations reported here. Other bands may have slightly different date ranges. Full data are available online.

3. Results and Discussion

3.1. Multiwavelength Cross-Correlation Results

Every blazar in our sample is highly variable in gamma-rays and, in many cases, in the optical/IR as well; only 3C273 shows minimal variations in the optical/IR. The optical, near-infrared and gamma-ray light curves are shown in Figure 1.

We investigate the correlation between optical and near-IR bands through the discrete correlation function (DCF, Edelson & Krolik 1988) with the corrections of White & Peterson (1994). Figure 2 shows the $B - J$ band DCF for each source in our sample. (We also show the $R - J$ band DCF for PKS 0528+134. This is the only source for which the DCF was significantly different in shape between bands.) Examining the DCFs for each source we find that, apart from 3C 273 which has no strong variations, all DCFs have a peak at zero lag. No source shows a significant peak at any non-zero lag. Note that given our daily cadence, we are sensitive only to lags longer than a couple of days. Figure 3 shows two examples of the correlation between optical (B -band) and IR (J -band) for two blazars: PKS 2155-304 (an HBL, Fig. 3a), and 3C 279 (an FSRQ, Fig. 3b). Fig. 3b also shows distinct tracks that reflect changes in the optical/IR spectral shape of 3C 279 over time (*cf.* Fig. 5b).

Six blazars — four FSRQs, one LBL, and one HBL — were bright enough during 2008–2010 to be regularly detected by Fermi LAT in one-day time bins. The gamma-ray - infrared discrete correlation functions for these sources are shown in Fig. 4). In three cases, the optical-IR variability has been shown to be reasonably well-correlated with the gamma rays: 3C454.3 (Bonning et al. 2009), PKS 1510-089 (Marscher et al. 2010), and AO 0235+164 (Agudo et al. 2011). The FSRQs 3C 273 and 3C 279 show weak (if any) correlations between infrared and gamma-rays, while the optical/IR emission of the HBL PKS 2155-304 is clearly uncorrelated with gamma-ray emission. The strongly disk-dominated FSRQ 3C 273, shows little to no variability in the optical/IR bands (fluctuations on the order of 1%) compared to the variations by a factor of several to 10 in gamma-rays. The small fractional variation at optical/IR frequencies in 3C 273 may be due to the relatively large luminosity of the accretion disk (Ramos et al. 1997), since the disk probably does not vary in the optical/IR over time scales as short as the gamma rays. For 3C 279, optical/IR-gamma ray correlations have been reported by Abdo et al. (2010) who note the coincidence of a gamma-ray flare with a strong change in optical polarization angle. However, our SMARTS data show larger amplitude changes (by several orders of magnitude) than the gamma-ray data, over both the first and second years of *Fermi* observations. The one HBL with high enough gamma-ray flux to appear consistently in the LAT daily fluxes, PKS 2155-304, shows variations of a factor of 2-3 in gamma-rays, along with longer-timescale variations in the optical-IR, but the two appear to be uncorrelated.

The close correlation of optical/IR and gamma-ray fluxes strongly favors leptonic models over hadronic models. In the latter, the two broad components of the SED should vary almost independently, while in leptonic models, the two peaks should vary together. In the FSRQs, the peak of the low energy component of the SED is in the far-IR, longward of the SMARTS bands, while the high-energy component peaks in or near the Fermi LAT energy range. In terms of simple homogeneous leptonic models, the SMARTS data generally sample emission from higher energy electrons than the Fermi LAT data. (this can obviously change if the SED peak moves, as in a major acceleration event, e.g. Pian et al. 1998, for the case of Mrk 501) More realistic electron distributions and/or geometries will complicate this picture, but in any case, as discussed in Section 4, there are multiple plausible reasons for variations in the strength of the optical-IR versus gamma-ray correlations among the FSRQs in our sample.

3.2. Excess Variance

Most blazars are strongly variable at gamma-ray energies and in the optical/IR. To quantify and compare the degree of variability in different blazars, and in different bands for the same blazar, we calculate the “excess variance,” which is the fractional root-mean-squared variability amplitude normalized by the mean flux:

$$F_{\text{var}} = \sqrt{\frac{S^2 - \overline{\sigma_{\text{err}}^2}}{\bar{x}^2}} \quad , \quad (1)$$

where S is the variance, σ_{err} is the observational uncertainty, and \bar{x} is the mean of the data (Nandra et al. 1997; Edelson et al. 2002; Vaughan et al. 2003). The values of F_{var} calculated for SMARTS and Fermi LAT data are listed in Table 2. In cases where K -band observations did not cover the same time periods as the other filters, we omit the K -band values.

The IR/optical/UV emission from blazars is a combination of thermal emission from a (possibly weak) accretion disk and relativistically beamed nonthermal emission from a jet. The disk emission peaks in the UV band so its relative contribution in optical/IR bands decreases toward longer wavelengths. Since the disk emission comes from $\gtrsim 10^4 r_g$ (Malkan 1983; Sun & Malkan 1989), it is almost certainly less rapidly variable than from the jet. Therefore, on the timescales considered here, we expect the variability amplitude for FSRQs (blazars with strong emission lines implying a radiatively efficient accretion disk) in the optical/IR to increase with wavelength, i.e., infrared bands to vary more than the optical. In general, this effect is seen in Table 2. For the FSRQs, J-band is more variable than B-band in all objects except 3C 279, in which the trend is reversed. In Section 4 and Figure 4f, it is shown that the changes in spectral shape of 3C 279 are also not consistent with a simply varying jet component overlaid on a constant blue accretion disk. The BL Lac objects do not show greater variability towards the IR: the two LBLs are more variable towards the B-band, and the HBL PKS 2155-304 shows no frequency-dependent variability changes. BL Lacs, having weak emission lines, are likely to have weakly accreting or radiatively inefficient disks, so it is not surprising that they do not behave as the majority of our FSRQs. However, this is a small sample, which includes the unusual source AO 0235+164 in which broad emission lines have been observed, the strength of which calls into question its status as an LBL (Cohen et al. 1987; Nilsson et al. 1996). Nevertheless, the SED of AO 0235+164 shows a strong and variable UV component in addition to the synchrotron and inverse-Compton peaks (Raiteri et al. 2008), which may explain its variability behavior observed here.

Name	Class	K	J	R	V	B	γ
PKS 0208-512	FSRQ	0.48	0.52	0.45	0.40	0.43	–
AO 0235+16	LBL	1.10	1.22	1.33	1.31	1.33	0.38
PKS 0528+134	FSRQ	–	0.53	0.28	0.24	0.35	–
OJ 287	LBL	0.45	0.37	0.43	0.45	0.46	–
3C 273	FSRQ	–	0.13	0.041	0.044	0.042	0.77
3C 279	FSRQ	0.49	0.79	0.82	0.87	0.86	0.38
PKS 1406-076	FSRQ	–	0.61	0.48	0.49	0.46	–
PKS 1510–08	FSRQ	–	1.04	0.94	0.94	0.83	0.56
PKS 1622-29	FSRQ	0.68	0.54	0.36	0.29	0.27	–
PKS 1730-130	FSRQ	0.58	0.47	0.37	0.34	0.35	–
PKS 2155-304	HBL	0.28	0.33	0.33	0.33	0.33	0.25
3C 454.3	FSRQ	0.68	0.58	0.51	0.47	0.44	1.40

Table 2:: Fractional variability amplitude (as defined in Eqn.(1) for observed IR, optical, and gamma-rays. The gamma-ray values are listed only for blazars bright enough to be detected in daily *Fermi*/LAT averages.

4. Color-magnitude variations

We present in Figure 4 the relation between IR (J -band) magnitude and optical-IR spectral shape of the low-energy peak of the SED (given by $B - J$ color, such that a *larger* value corresponds to a *redder* color). Overall, luminous blazars (FSRQs) are redder when brighter and bluer when fainter. A typical example is shown in Fig. 4i (PKS 1622-29). As the source varies in brightness, the color changes along a narrow locus in the color-magnitude plane, such that when the source is brighter, the color gets redder. Conversely, when the source is fainter, the color gets bluer (although the SED remains synchrotron-dominated and therefore red). This ‘flattening’ of the SED in faint states suggests a strong, blue accretion disk component is mixed with redder jet emission, which may only be visible as a typical ‘blue bump’ in extremely faint states (e.g. as observed in 3C 454.3 by Raiteri et al. 2007). Most of our FSRQs (with exceptions noted below) follow this redder-when-brighter track, consistent with FSRQs having luminous accretion disks as also evidenced by their typically strong emission lines.

Although the FSRQs mostly show redder-when-brighter trends, they can also show more complicated behavior. For example, the May 2010 flare in PKS 1510-089 (indicated by arrows in Fig. 4h) was essentially achromatic and, unlike its other flares, had a much larger amplitude than the associated gamma-ray flare (cf. Fig. 1h). Such anomalous flares indicate the interplay of distinct components in the source; in the case of PKS 1510-089, the

sharp achromatic flare could be caused by a plasma blob hitting a transverse shock in the jet (Marscher et al. 2010). (More speculatively, achromatic flares could be caused by gravitational microlensing in the halo of our galaxy, as in the MACHO experiment (Alcock et al. 2000), since these blazar jets are effectively point sources, but the probability of such an event should be vanishingly small.) Similarly, the December 2009 flare of 3C 454.3 (Fig. 4l) moved off the standard red-bright track, although it was not as obviously achromatic.

In contrast to FSRQs, the lower luminosity BL Lac objects do not show the same color-magnitude trend, consistent with BL Lacs having weak accretion disks. The HBL PKS 2155-304 is shown in Fig. 4k; its variations are more random with respect to color, and smaller in amplitude.

Somewhat more complicated is the color behavior of the LBL OJ 287 (Fig. 4d), which shows some redder-when-brighter changes but also variations that are bluer-when-brighter, and still other color changes at fixed magnitude. OJ 287 is known for a striking series of double-peaked outbursts occurring approximately every 12 years over the last century (Sillanpaa et al. 1988; Lehto & Valtonen 1996). Our observing period begins after the last double outburst in 2005-2007. We find that OJ 287 is brighter and more variable post-burst than it was between the 2005 and 2007 peaks. As it was during the double-peaked bursts, OJ 287 remained highly polarized during the early 2009 observing season (see Figure 1 of Villforth et al. 2010), with a strong, stably, underlying optically polarized core. Villforth et al. also found an overall bluer-when-brighter color trend over the time period 2005-2009. Additionally, observations in 1993-1994 showed constant optical colors over a range in optical flux (Sillanpaa et al. 1996; Hagen-Thorn et al. 1998). They suggest that these changes in spectral shape are due to injections of high energy electrons into the jet emitting region. Alternatively, it may be that the accretion disk component in OJ 287 is variable and comparable in magnitude to the jet component. This is suggested by analogy to X-ray binaries, in which this complicated color-magnitude behavior is a known phenomenon, and hysteresis in the X-ray flux–spectral index plane has been interpreted in terms of accretion state changes (Smith et al. 2007; Maccarone & Coppi 2003). (Due to their hotter accretion disks, the thermal peak in X-ray binaries lies in the soft X-ray, compared to the rest-frame UV for LBLs and FSRQs.) On the other hand, hysteresis behavior has also been reported for the HBL PKS 2155-304 (Kataoka et al. 2000), in which the X-rays come from the jet and no disk has been detected. This hypothesis can be tested by observing changes in emission lines; if the disk is varying, the lines should respond in intensity. On balance, it is not obvious what causes the unusual color-magnitude trends in OJ 287.

Still more anomalous behavior is exhibited by AO 0235+164 (Fig. 4b). At the beginning of our monitoring program, for example, increasing intensity was characterized by bluer (not

redder) colors. This was also when AO 0235+164 was detected by Fermi in the daily light curve (i.e., it was gamma ray-bright, cf. Fig. 1b). Later, when the source was much fainter in gamma rays, the color-magnitude trend reverted to the usual redder-when-brighter relation.

AO 0235+164 is an unusually situated source. An AGN sits $2''$ to the south of the blazar as well as an intervening galaxy at $z = 0.525$ (Yanny et al. 1989; Burbidge et al. 1996; Nilsson et al. 1996), which we do not resolve in our imaging. The AGN has a fairly blue spectrum ($B = 21.4, V = 20.9, R = 20.5$) which has not been observed to vary strongly (Raiteri et al. 2005). The extinction due to the intervening galaxy is nearly a magnitude greater than the Galactic extinction ($A_B = 1.268$ vs 0.341 , Junkkarinen et al. 2004), resulting in a very intrinsically red spectrum. We removed the contribution from this AGN in the B band before plotting the color-magnitude relation in Fig. 4b, so the bluer-when-fainter behavior of AO 0235+164 is not due to the underlying blue colors of the nearby AGN.

If the observed optical-IR emission is a combination of jet and accretion disk, and if the gamma rays are produced by inverse Compton scattering of disk or line photons, then the two trends can be explained self-consistently. When the jet becomes brighter, the color of the combined emission gets redder since the jet synchrotron emission is intrinsically redder than that of the blue accretion disk. Alternatively, if the jet is constant and the disk emission increases, then the summed emission becomes bluer. Moreover, an increase in disk emission would be accompanied by a strong increase in gamma rays, due to the increased scattering of disk/line photons, hence the association of a bright gamma-ray state with the bluer-when-brighter trend. In addition, when the jet is quite bright ($J \gtrsim 14$ in this case), further brightening of the jet may be due to emission from an even higher energy population of electrons; this would also result in a bluer color. 3C 279 (Fig. 4b) has a very similar (i.e., hybrid) color-magnitude diagram, roughly achromatic in the optical when bright in gamma rays but much fainter in gamma rays when it moves along the more usual FSRQ bluer-when-fainter trend.

In the examples of AO 0235+16 (Fig. 4b) and 3C 279 (Fig. 4f), different loci in the optical/IR color-magnitude diagram are associated with different gamma-ray intensities. This bimodal behavior has some similarity to the Galactic X-ray binaries. For example, the X-ray binary GX 339-4 has been observed to change from a bluer-when-brighter state (associated with the high/soft X-ray state) to a redder-when-brighter state (associated with the hard X-ray state — see Buxton et al. 2011 submitted). X-ray binary emission is a combination of soft X-rays from a disk and hard X-rays from a power-law component (likely from a hot corona). In the canonical “high-soft” state, the X-ray spectrum is disk-dominated and hence, softer, but the intensity is higher, while in the canonical “low-hard” state the intensity is lower but the spectrum is dominated by the power-law component, hence, harder

(Remillard & McClintock 2006). There is a third so-called “very high state” in which the XRB spectrum is dominated by the power-law component at a very high intensity. For these anomalous FSRQs, the gamma-ray bright times may correspond to the “very high state,” in which case the optical emission will also be very bright and will get bluer when brighter because it is totally jet dominated.

5. The time-dependent spectral energy distribution

Figure 5 shows the variable broadband spectral energy distribution for 3C 454, with quasi-simultaneous data (within hours) for UT 2009 Dec. 03 (*blue*) and UT 2009 Dec. 04 (*red*), when the source was near the peak of its large December 2009 flare. A representative SED for a non-flaring state is shown for UT 2009 Aug. 12 when the source was relatively faint (*black*). The X-ray (*Swift* XRT and BAT) and gamma-ray (*Fermi*) data points shown are taken from the analysis in the paper of Bonnoli et al. (2011). The NIR-optical points shown are the SMARTS monitoring data presented in this paper, dereddened using the extinction relations in Cardelli et al. (1989), with the value for A_B given by Schlegel et al. (1998). Magnitudes were converted into flux densities using the zero-point fluxes given by Bessell et al. (1998) and Beckwith et al. (1976). The observing conditions were photometric with good seeing on the nights shown in Fig. 5. The near-IR part of the spectrum shows a significant change between the two nights, turning over between J and K bands. We searched the light curve of 3C 454.3 for similar behavior and found similar turnovers in the NIR SED on 12 nights, generally also with good observing conditions. This flattening of the SED occurred in faint states as well as bright states.

The gamma-ray (inverse Compton) and optical-NIR spectra (presumably the high-energy end of the synchrotron emission component) both varied significantly during the 3-4 Dec 2009 flare, but in opposite senses. That is, the gamma-ray spectrum flattened and declined slightly while the optical/IR steepened and increased in flux. This definitely points to complex physical changes beyond a simple electron acceleration event. Note that the SMARTS data are extended enough in energy coverage that one can see that the synchrotron spectrum is not consistent with a power law and that the synchrotron emission peak likely moved. On the other hand, if one ignored the NIR (J, K band) points, then one might conclude from the small spectral changes in the optical and gamma-rays that the underlying electron energy distribution and source parameters were roughly similar. This was the conclusion of Bonnoli et al. (2011), who focused on fitting the X-rays and gamma-rays and only roughly matched the optical intensity of the source. Thus the ability of SMARTS to cover both optical and IR bandpasses constrains the physical interpretation in ways that

gamma-ray or optical monitoring alone does not.

The SEDs on the two nights of the December 2009 flare were modeled using the one zone code of Coppi (1992). This model injects electrons with a power-law distribution in energy, turning over at the high energy end, giving effectively a maximum and minimum γ , as also used in the models of Ghisellini et al. (cf. Ghisellini et al. (2007)). We assume a soft photon field with a black body temperature of $kT \sim 1-10$ eV that is isotropic in the jet frame. The electron distribution is convolved with the synchrotron spectrum and thermal photon field to produce gamma-rays. The key difference between the Coppi (1992) code and others is that the electron spectrum changes through both synchrotron and Compton cooling. In the Klein-Nishina limit, Compton cooling becomes inefficient while synchrotron cooling is not affected, thus producing more power in the high-frequency end of the synchrotron radiation. This may be what is seen in the $J - K$ band peak.

If we assume the optical-NIR emission is produced in the same source region as the gamma-rays (which is not unreasonable as this is a very bright flare and the gamma-ray and optical variations are correlated), then our preliminary SED modeling of the NIR to gamma-ray data (shown by the solid red and blue curves in Fig. 5) indicates that the source variations must be significant. For source parameters similar to Bonnoli et al. (2011) ($R_{source} \sim 10^{17}$ cm, $\delta \sim 20$, $B \sim 1$, $\gamma_{peak} \sim 500$), we find that the electrons responsible for the optical-NIR emission are likely higher in energy than those responsible for the gamma-ray emission, and that Klein-Nishina effects are thus important for them. This means that in order to produce a *steeper* yet higher amplitude synchrotron spectrum, the external photon field seen by the emitting electrons must have changed to include more lower-temperature photons than the BLR; see Moderski et al. (2005b) and Moderski et al. (2005a) for a discussion of the dependence of Klein-Nishina effects on the external photon field. Varying the ambient photon field alone, however, is not enough to explain all the observed spectral changes: in the context of traditional one-zone synchrotron-Compton models, some combination of peak electron energy, the magnetic field, and the Doppler beaming factor must have changed by factors of two or more.

We note here that this is not a systematic exploration of parameter space, but merely a demonstration that the short-term variations in the SED cannot be produced merely through changing the maximum value of γ , or the strength of the magnetic field alone. The change in model parameters has to be more complicated. Further exploration of multiwavelength spectral variability will be presented in a forthcoming paper (Chatterjee et al. *in prep.*). We further note that if our preliminary conclusions are correct, namely that gamma-ray and optical emission comes from somewhat different energy electrons, and that the mapping from electron energy to synchrotron and Compton photon energy may change during the

flare, then this might explain why we see general but not exact correlations between the variability in gamma-ray and lower energy bands. One-zone models may still have some relevance during bright flares, if one region of the jet dominates the overall emission. Finally, this implies that the lore that Fermi spectra do not change much during flares appears to be at best a coincidence in 3C 454.3: the underlying electron and target photon spectra probably change significantly.

6. Conclusions

Systematic monitoring of southern blazars with the SMARTS optical+infrared ANDICAM has generated BVRJK light curves for a dozen blazars, all of which were contemporaneously observed with the Fermi gamma-ray satellite. All of the SMARTS blazar photometry is available on a publicly accessible web site, <http://www.astro.yale.edu/smarts/fermi>. This paper reported on the 12 blazars that have well defined optical/IR light curves over the first 2 years of the Yale/SMARTS blazar monitoring project, which commenced in August 2008.

Not all twelve blazars are significantly detected in gamma-rays on \sim day timescales. For the first two years of data (through July 2010), six SMARTS-monitored blazars were bright enough to be well detected in one-day averages at gamma-ray energies: the FSRQs 3C 454.3, 3C 273, 3C 279, and PKS 1510-089; the LBL AO 0235+164; and the HBL PKS 2155-304. Detailed multiwavelength analysis was presented for these six.

We find the optical/IR and gamma-ray light curves for these six southern blazars are generally well correlated, with lags of less than 1 day for most FSRQs (roughly the sampling interval for the SMARTS and Fermi data). This strongly supports leptonic models in which ambient photons — perhaps from the accretion disk or broad emission-line clouds — are up-scattered to gamma-ray energies by synchrotron-emitting electrons in the relativistic blazar jet. Hadronic models, in which the gamma-rays come from energetic protons that ultimately decay into synchrotron-emitting electrons, do not have the same natural explanation for correlated optical/IR and gamma-ray variability.

The multiwavelength variability for the six blazars shows two types of behavior. In luminous blazars like FSRQs, the amplitude of optical/IR variability decreases towards shorter wavelengths, as if that wavelength range had a significant underlying contribution from a more slowly varying thermal disk peaking in the UV. In BL Lac objects, the optical/IR variability is similar in different bands, consistent with little or no contribution from a (radiatively inefficient) disk.

Color-magnitude variations in these six blazars can be explained in part by highly

variable jet emission mixed with slower varying disk emission. Gamma-ray flares can result from particle acceleration in the jet or from secular increases in disk/line emission, hence the somewhat complicated trajectories of blazars in color-magnitude space. Analogous multiple-state behavior has been observed in Galactic X-ray binaries. Meanwhile, individual jet flares in a given source can also follow different color-color tracks because of, for example, standing shocks in different parts of the jet.

The best-studied blazar, the FSRQ 3C 454.3, has had a strong flare in each year of SMARTS-*Fermi* monitoring. Its optical/IR and gamma-ray light curves are well correlated, with no measureable lag longer than one day. Its broad-band SED in the bright state is well fit by an external Compton model; in its faint state, the disk contributes a larger fraction of the light and the SED is flatter. Day-to-day changes are difficult to explain with a simple one-zone model, however, unless there are large changes (factors of two or more) in Doppler factor, electron energy, and/or magnetic field. More generally, our simple analysis of the 3C 454.3 SED suggests that optical/IR radiation comes from slightly higher energy electrons than the GeV gamma rays, and that Klein-Nishina effects are important in shaping both SED components.

SMARTS monitoring of southern blazars continues, with the goal of producing additional rich multiwavelength data sets that will advance our further understanding of blazar emission mechanisms and energy transport. In more than three years of monitoring several dozen blazars, only 6 sources - in three different classes - have produced multiwavelength data of sufficient quality for detailed analysis. Only some of these showed distinct flares over this period. The rarity of blazars being bright while visible from ground (often there have been dramatic gamma-ray flares while the sources had not yet risen in the night sky) suggests that continued dedicated optical-infrared monitoring is essential during the lifetime of the *Fermi* gamma-ray observatory.

SMARTS observations of LAT-monitored blazars are supported by Fermi GI grant 011283 and by Yale University. CDB, MMB and the SMARTS 1.3m observing queue receive support from NSF grant AST-0707627. RC is supported by Fermi GI grant NNX09AR92G. GF is supported by Fermi GI grant NNX10A042G. JI is supported by the NASA Harriet Jenkins Fellowship program and NSF Graduate Research Fellowship under Grant No DGE-0644492. This research has made use of the NASA/IPAC Infrared Science Archive, which is operated by the Jet Propulsion Laboratory, California Institute of Technology, under contract with the National Aeronautics and Space Administration.

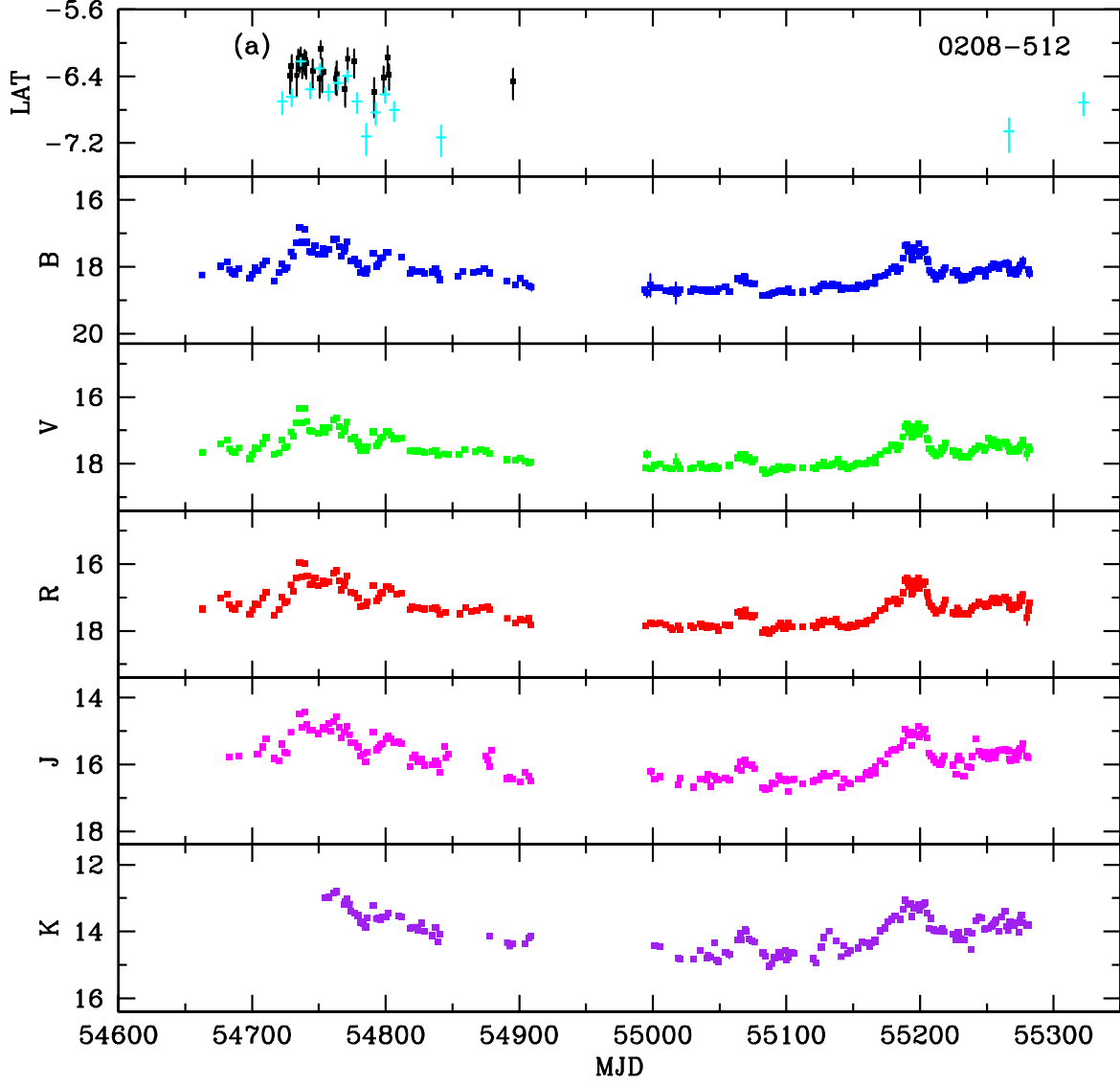


Figure 1a: SMARTS optical and near-infrared light curves for PKS 0208-512. *Fermi*/LAT fluxes are taken from the public daily (black points) and weekly (cyan points) light curves and are in units of $\log(\text{photons sec}^{-1} \text{ cm}^{-2})$.

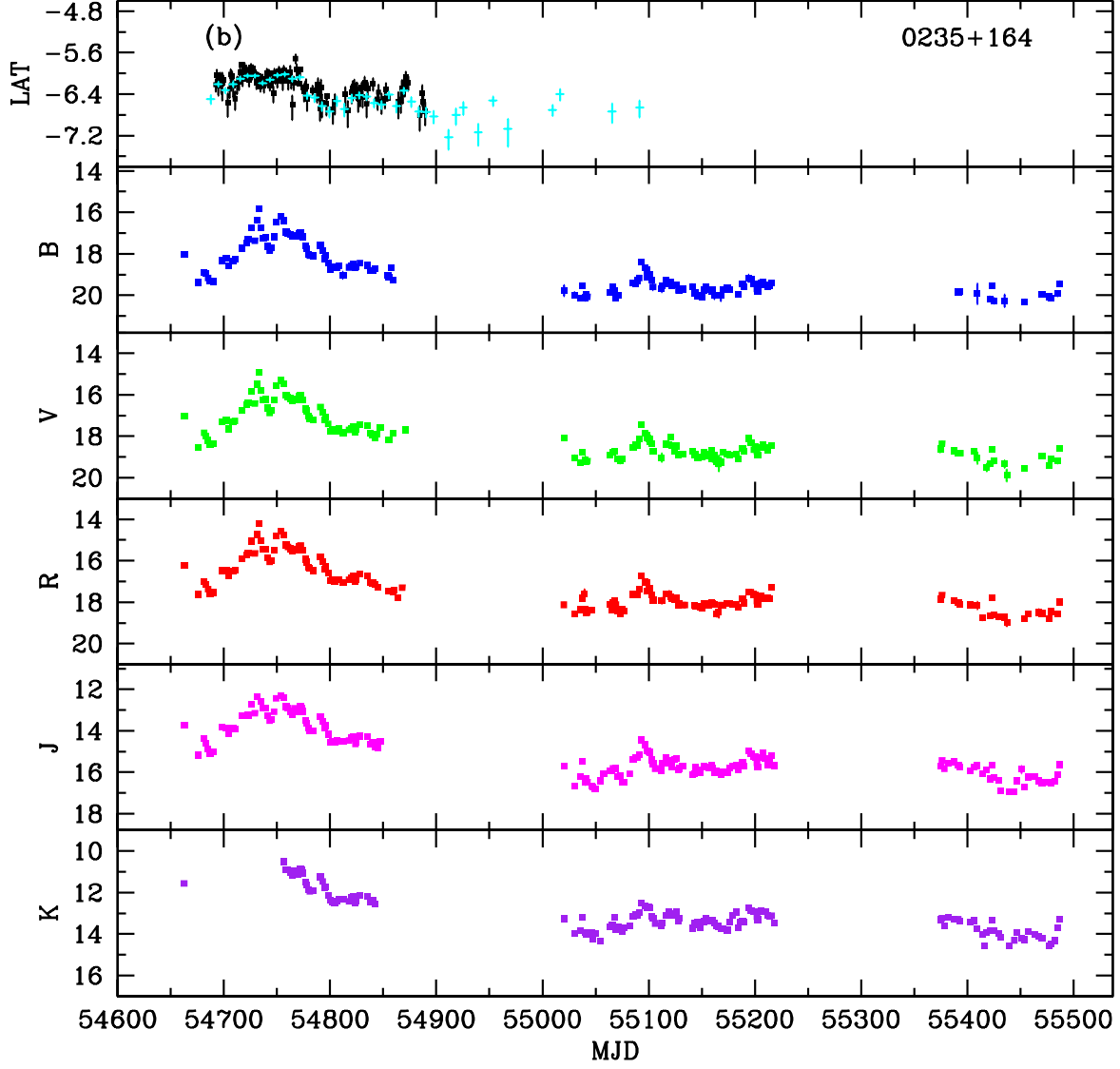


Figure 1b: SMARTS optical and near-infrared light curves for AO 0235+164. *Fermi*/LAT fluxes are taken from the public daily (black points) and weekly (cyan points) light curves and are in units of $\log(\text{photons sec}^{-1} \text{ cm}^{-2})$.

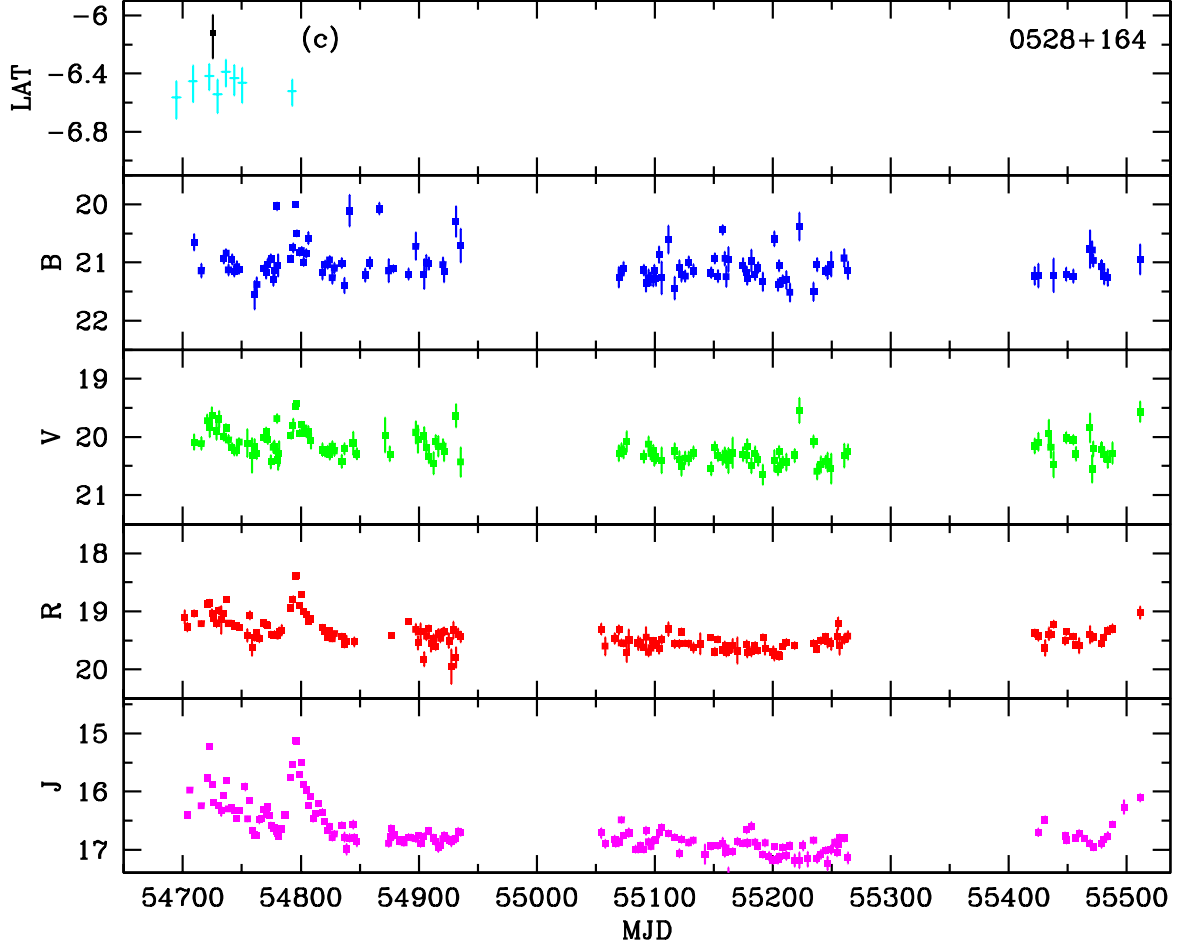


Figure 1c: SMARTS optical and near-infrared light curves for PKS 0528+134. *Fermi*/LAT fluxes are taken from the public daily (black point) and weekly (cyan points) light curves and are in units of $\log(\text{photons sec}^{-1} \text{ cm}^{-2})$.

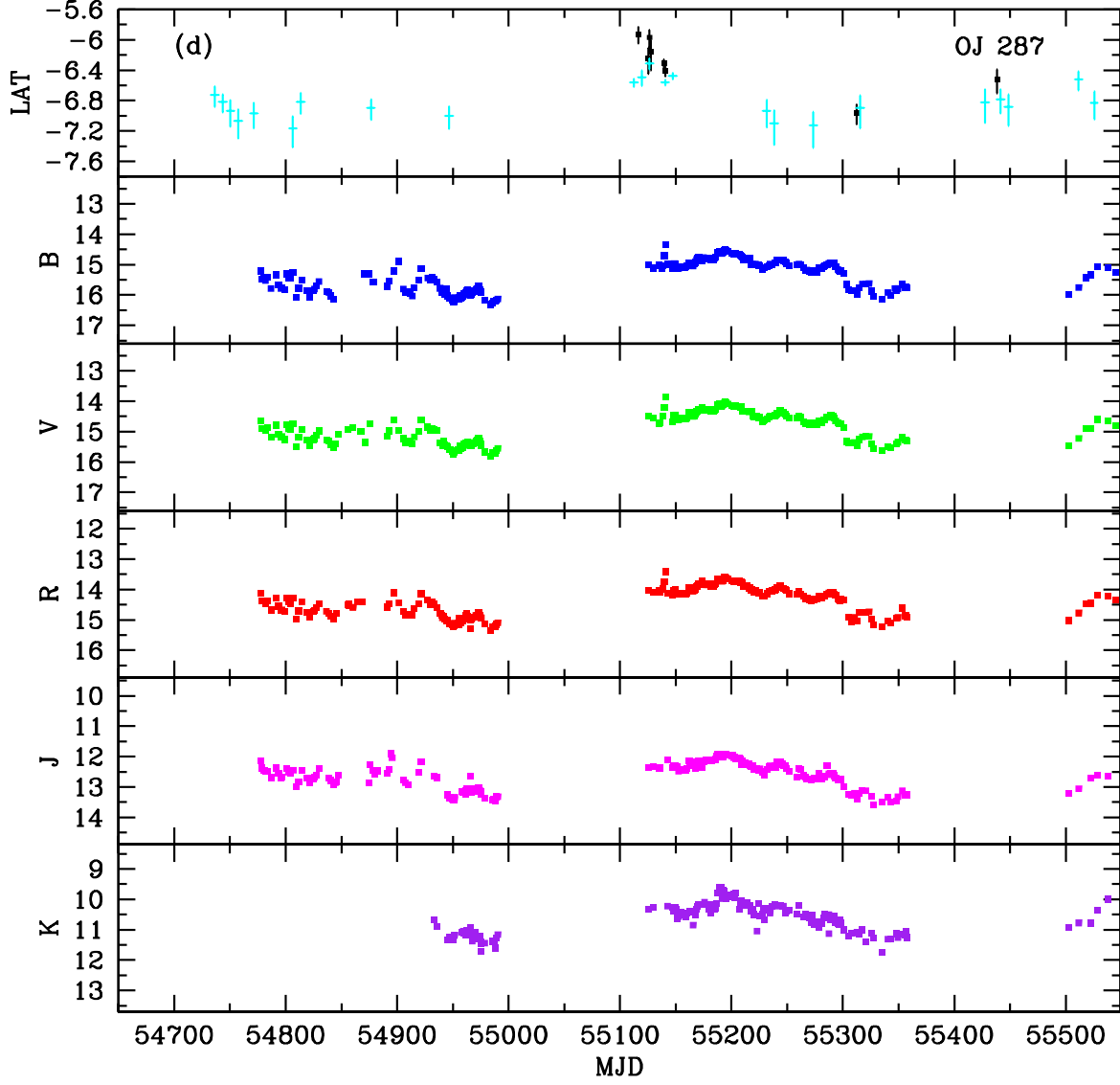


Figure 1d: SMARTS optical and near-infrared light curves for OJ 287. *Fermi*/LAT fluxes are taken from the public daily (black points) and weekly (cyan points) light curves and are in units of $\log(\text{photons sec}^{-1} \text{ cm}^{-2})$.

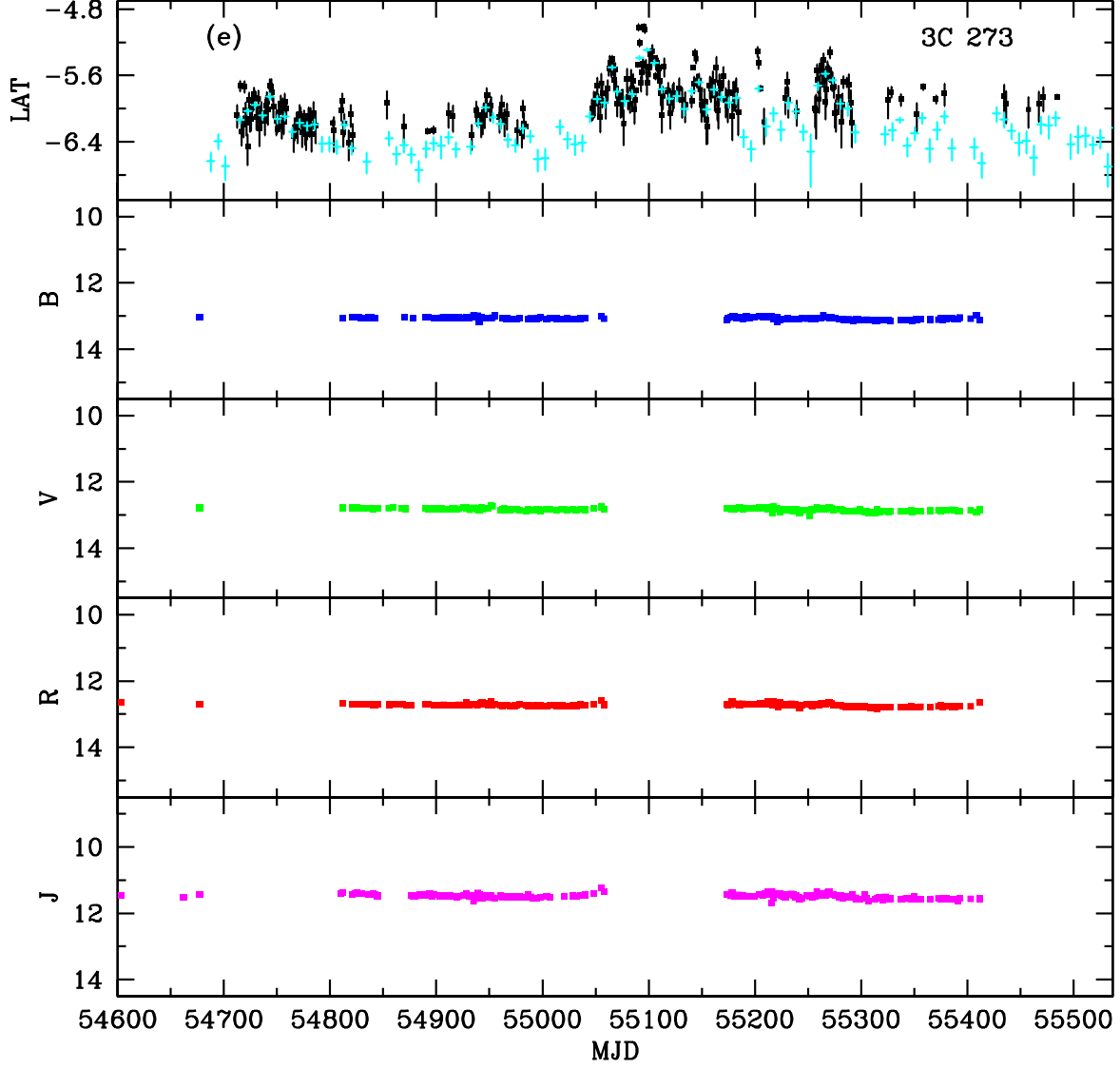


Figure 1e: SMARTS optical and near-infrared light curves for 3C 273. *Fermi*/LAT fluxes are taken from the public daily (black points) and weekly (cyan points) light curves and are in units of $\log(\text{photons sec}^{-1} \text{ cm}^{-2})$.

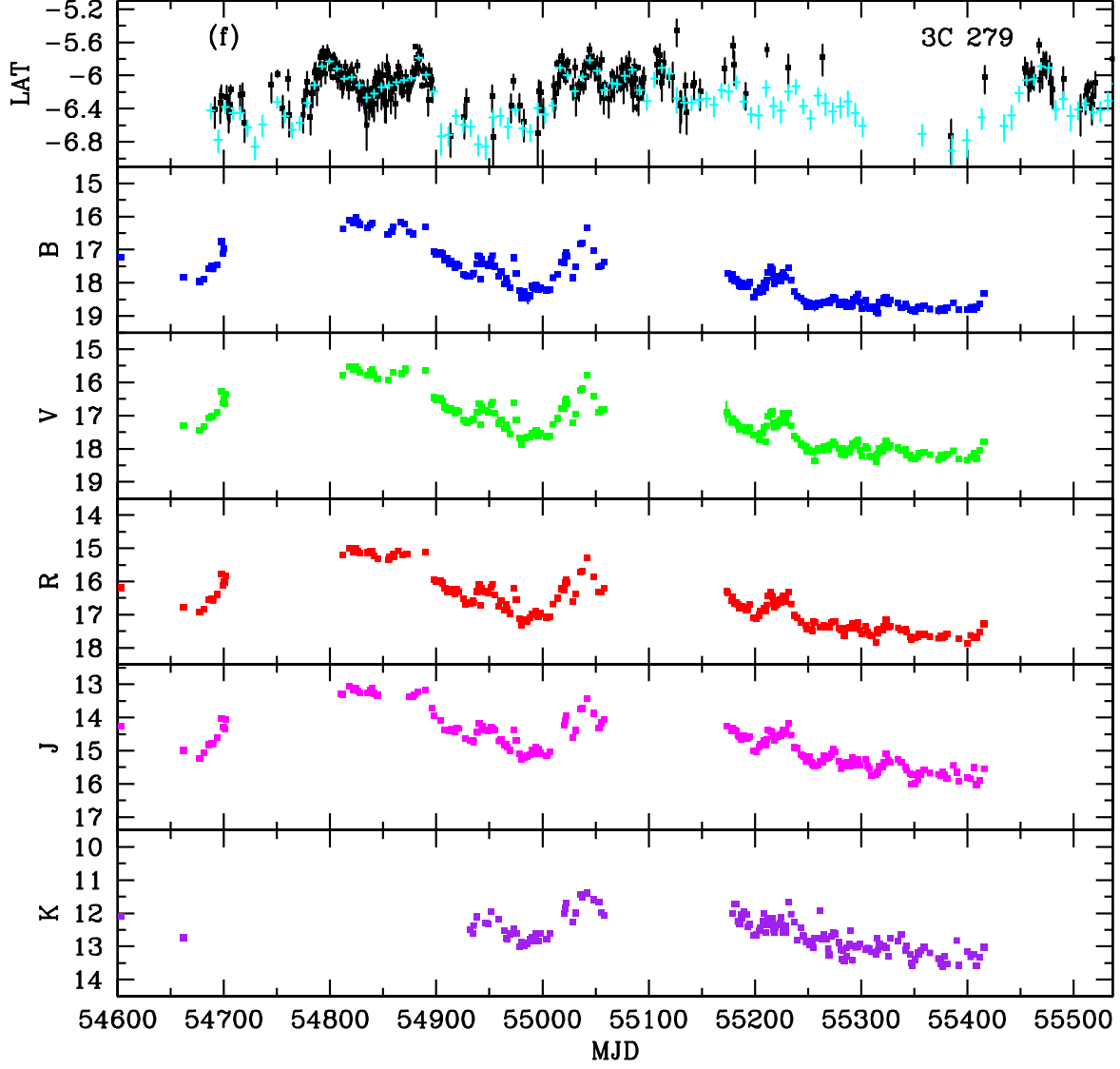


Figure 1f: SMARTS optical and near-infrared light curves for 3C 279. *Fermi*/LAT fluxes are taken from the public daily (black points) and weekly (cyan points) light curves and are in units of $\log (\text{photons sec}^{-1} \text{ cm}^{-2})$.

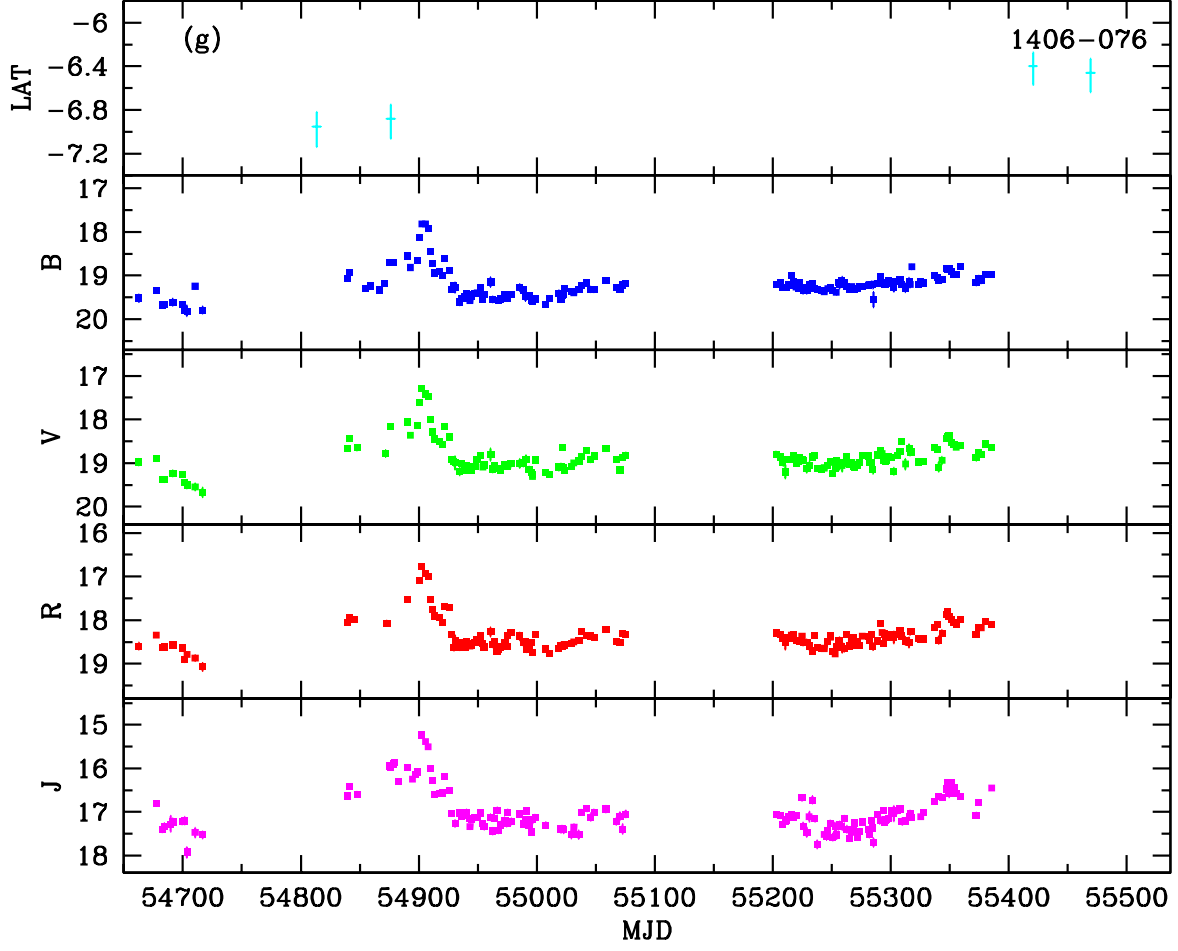


Figure 1g: SMARTS optical and near-infrared light curves for PKS 1406-076. *Fermi*/LAT fluxes are taken from the public weekly (cyan points) light curves and are in units of $\log(\text{photons sec}^{-1} \text{ cm}^{-2})$.

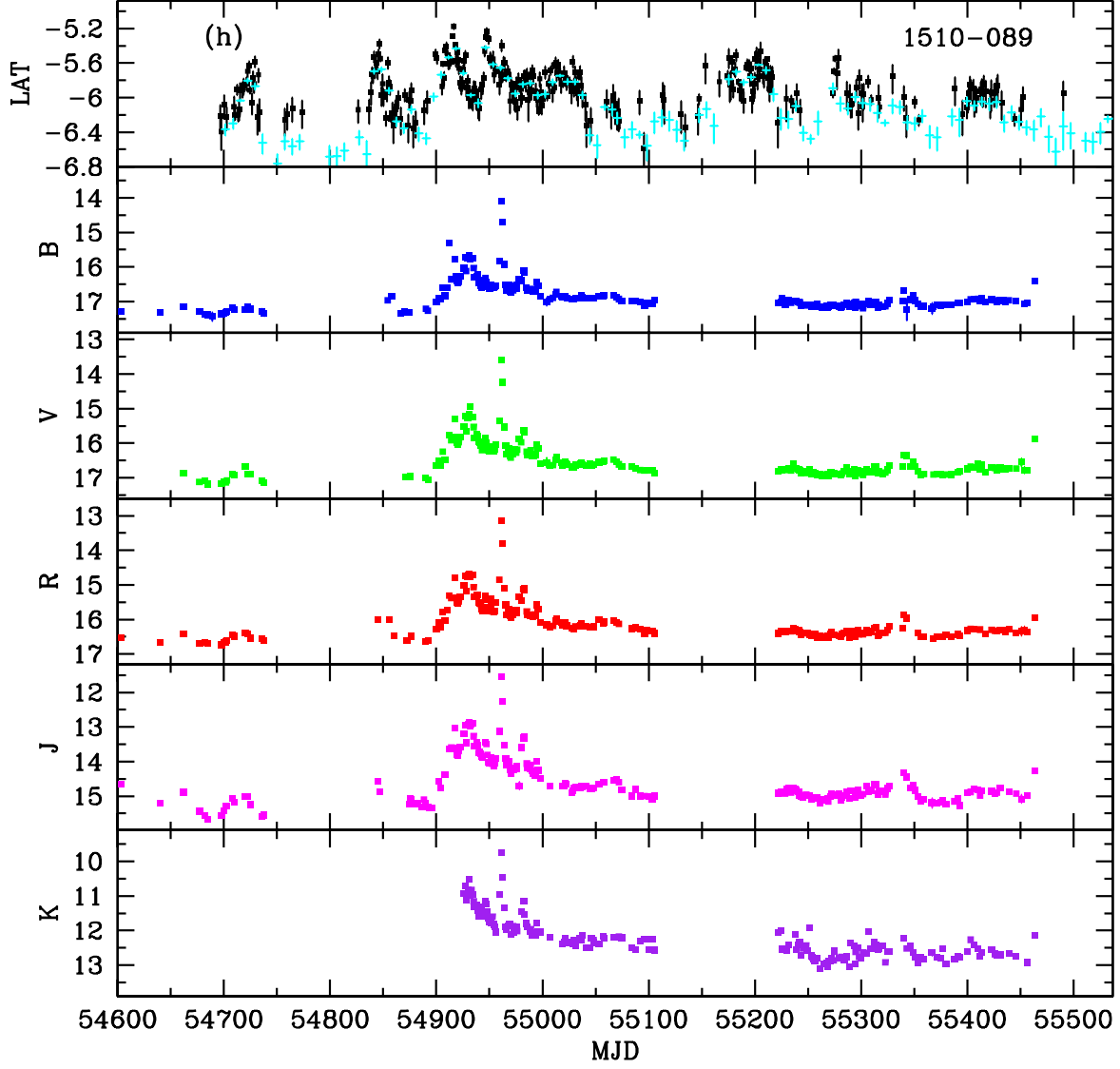


Figure 1h: SMARTS optical and near-infrared light curves for PKS 1510-089. *Fermi*/LAT fluxes are taken from the public daily (black points) and weekly (cyan points) light curves and are in units of $\log (\text{photons sec}^{-1} \text{ cm}^{-2})$.

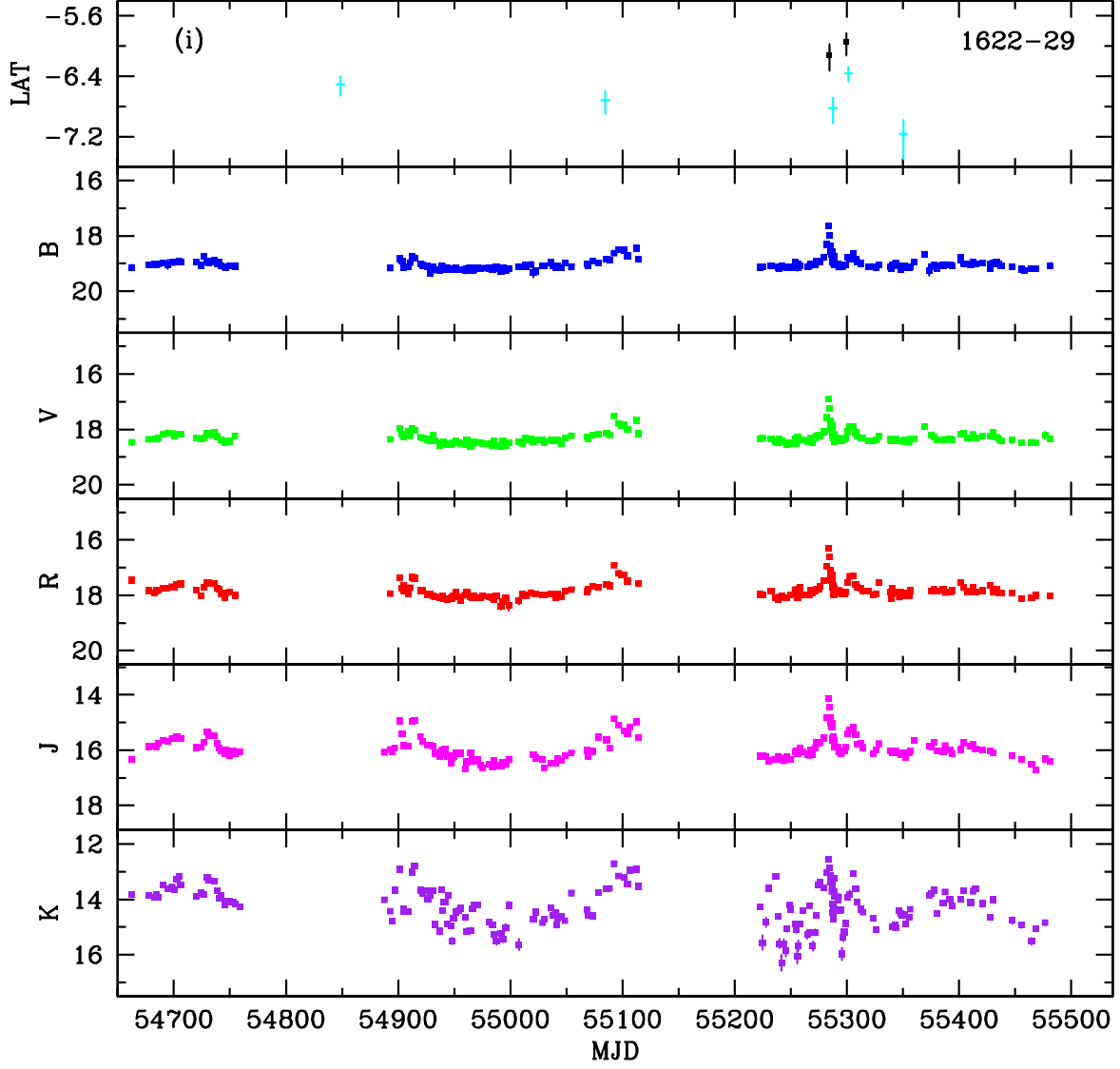


Figure 1i: SMARTS optical and near-infrared light curves for PKS 1622-297. *Fermi*/LAT fluxes are taken from the public daily (black points) and weekly (cyan points) light curves and are in units of $\log(\text{photons sec}^{-1} \text{ cm}^{-2})$.

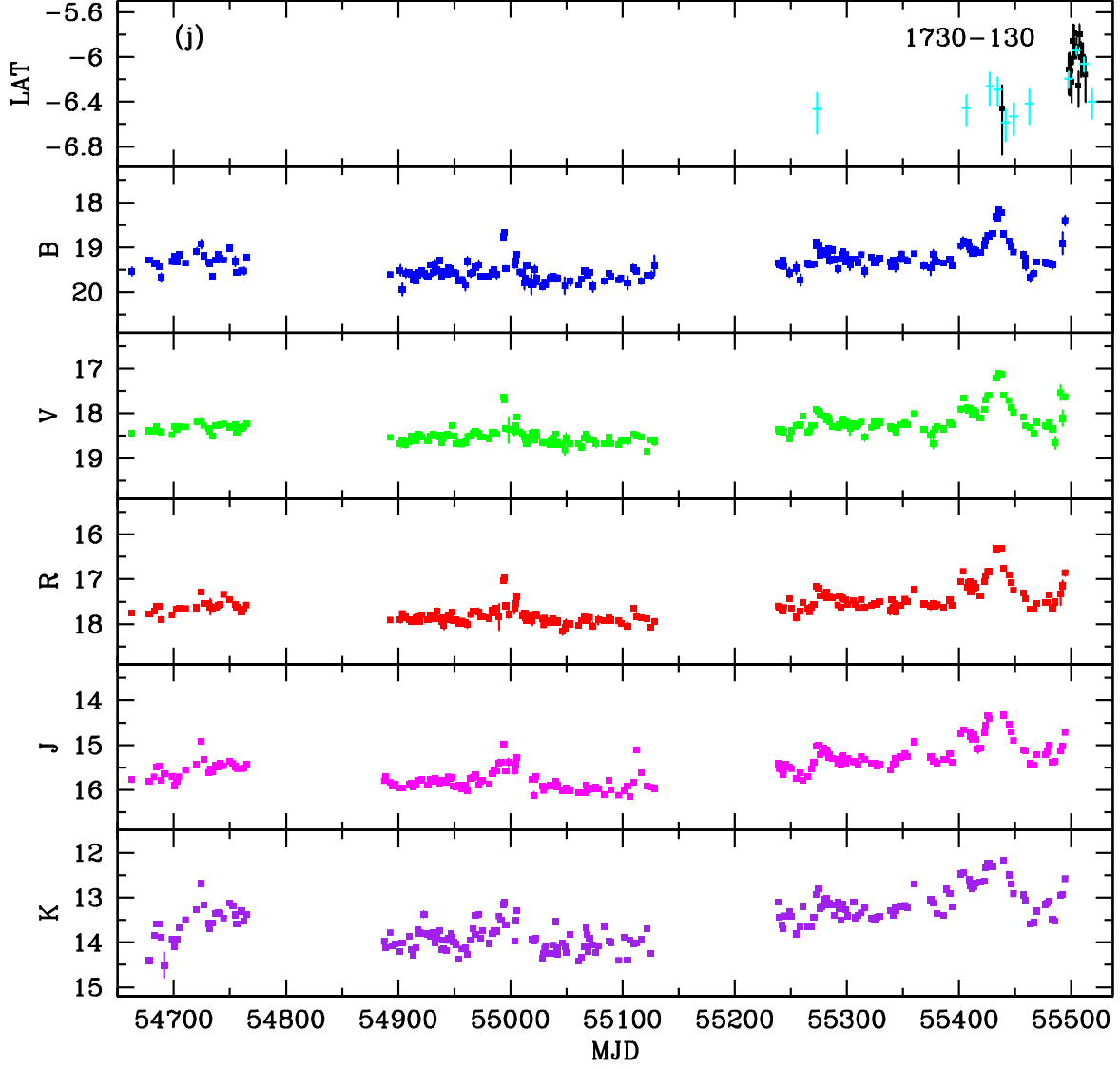


Figure 1j: SMARTS optical and near-infrared light curves for PKS 1730-130. *Fermi*/LAT fluxes are taken from the public daily (black points) and weekly (cyan points) light curves and are in units of $\log(\text{photons sec}^{-1} \text{ cm}^{-2})$.

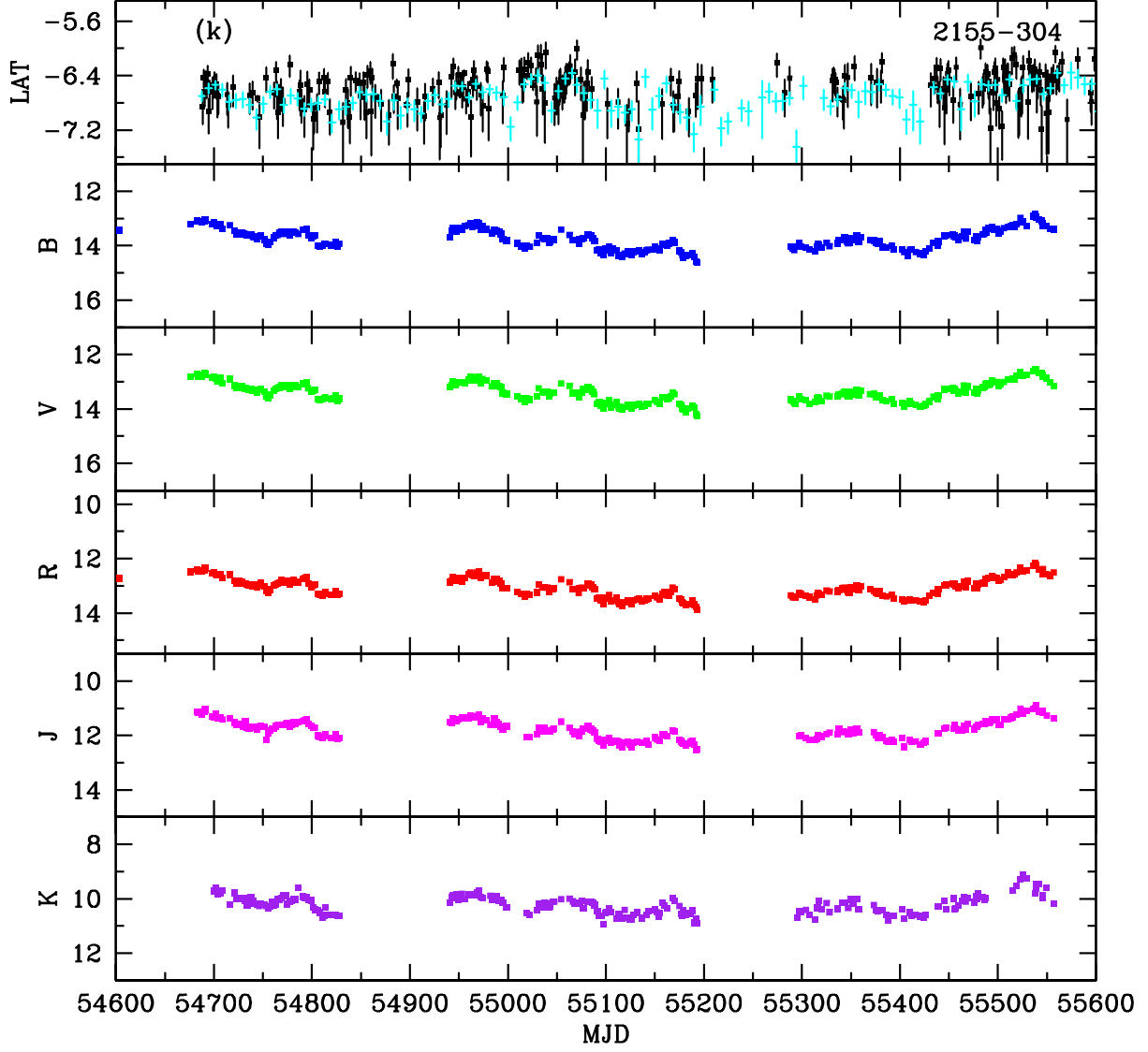


Figure 1k: SMARTS optical and near-infrared light curves for PKS 2155-304. *Fermi*/LAT fluxes are taken from the public daily (black points) and weekly (cyan points) light curves and are in units of $\log(\text{photons sec}^{-1} \text{ cm}^{-2})$.

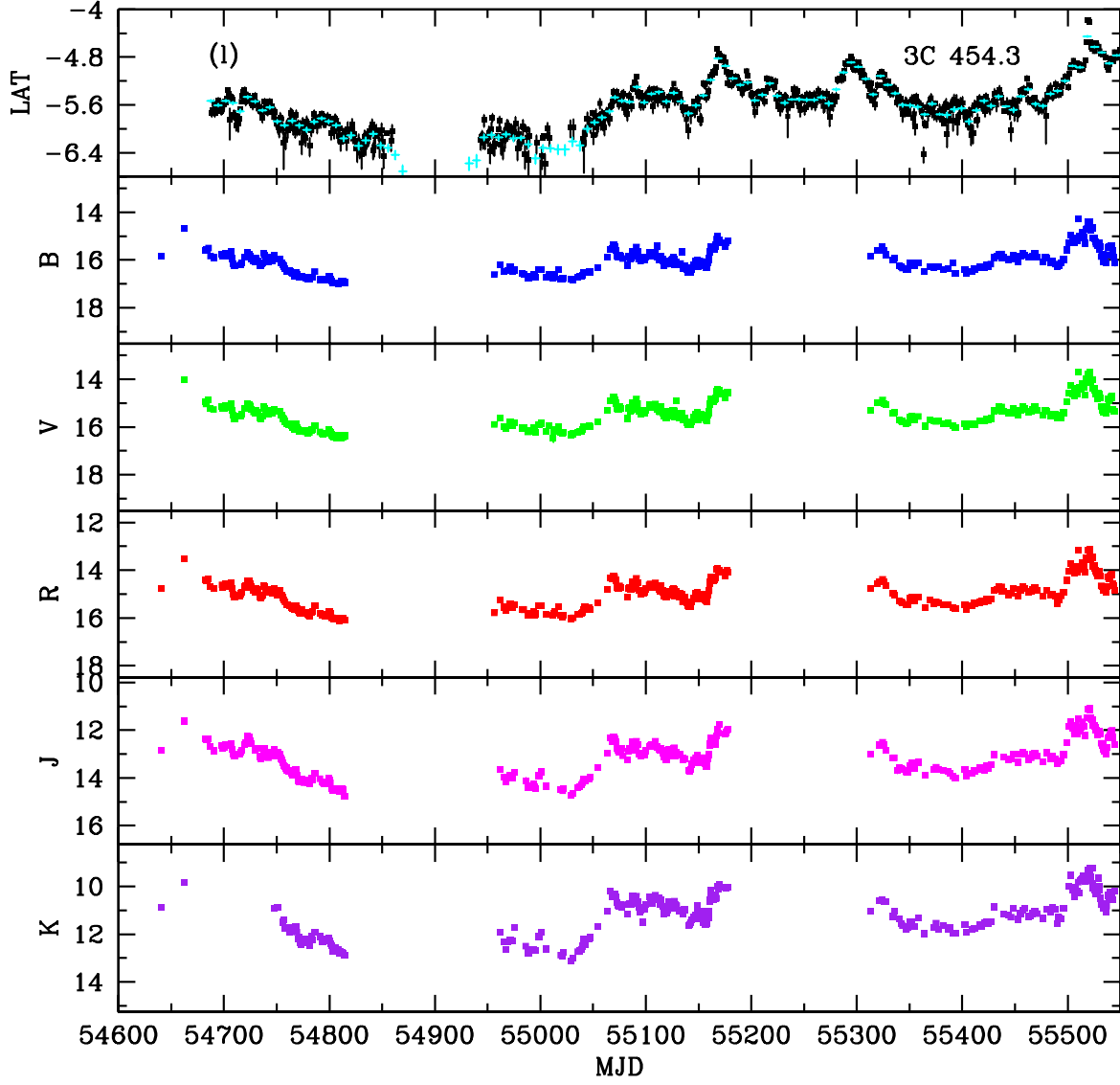


Figure 11: SMARTS optical and near-infrared light curves for 3C 454.3. *Fermi*/LAT fluxes are taken from the public daily (black points) and weekly (cyan points) light curves and are in units of $\log(\text{photons sec}^{-1} \text{ cm}^{-2})$.

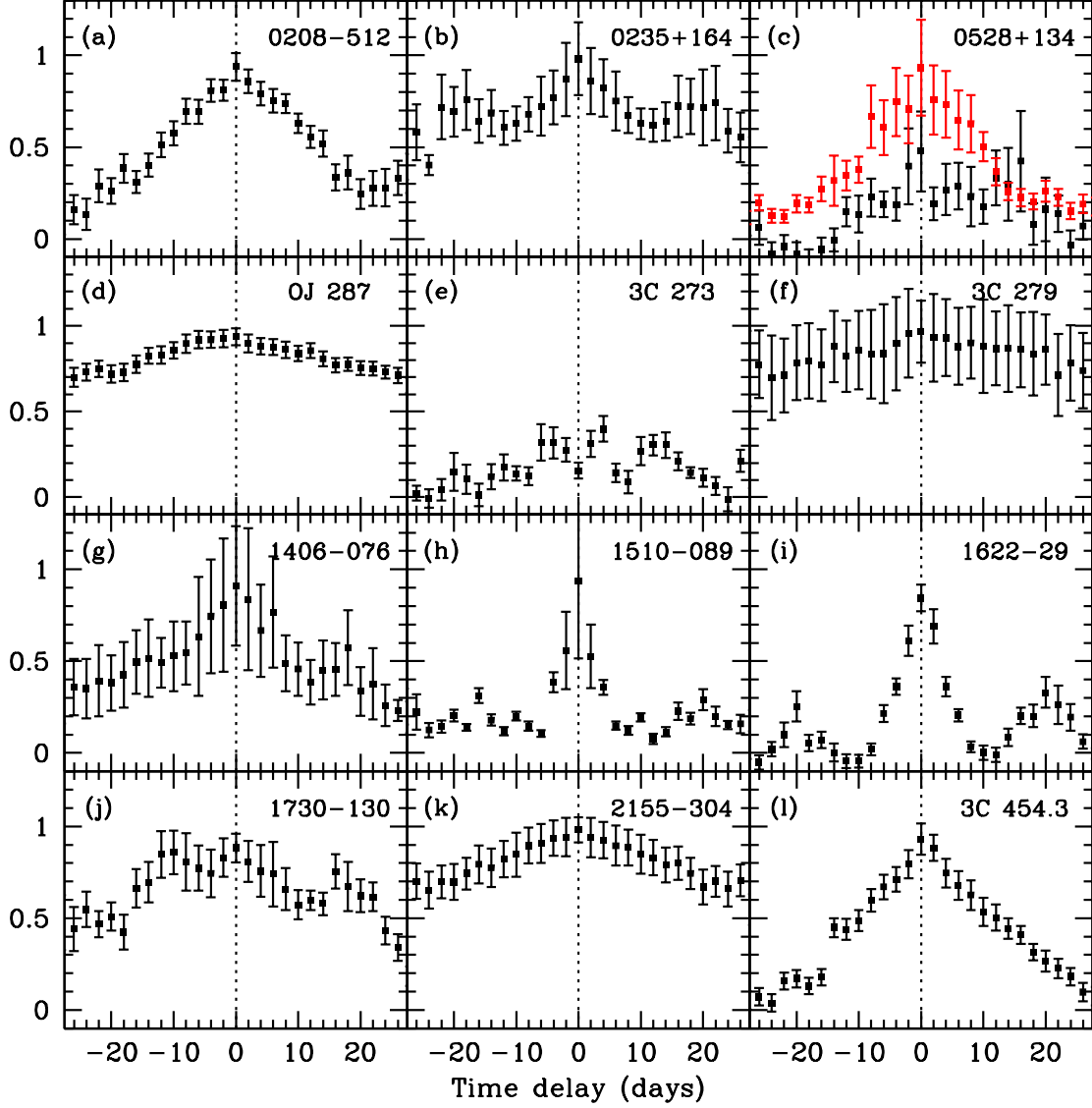


Fig. 2: Discrete correlation functions (DCF) for B vs J -band light curves shown in Figure 1. With the exception of the minimally varying quasar 3C 273, all DCFs show a maximum at zero lag. Figure 2c also shows the R vs. J DCF for PKS 0528+134 (in red). It is the only source for which the R vs. J DCF has a significantly different shape than $B - J$, although it too peaks at zero lag.

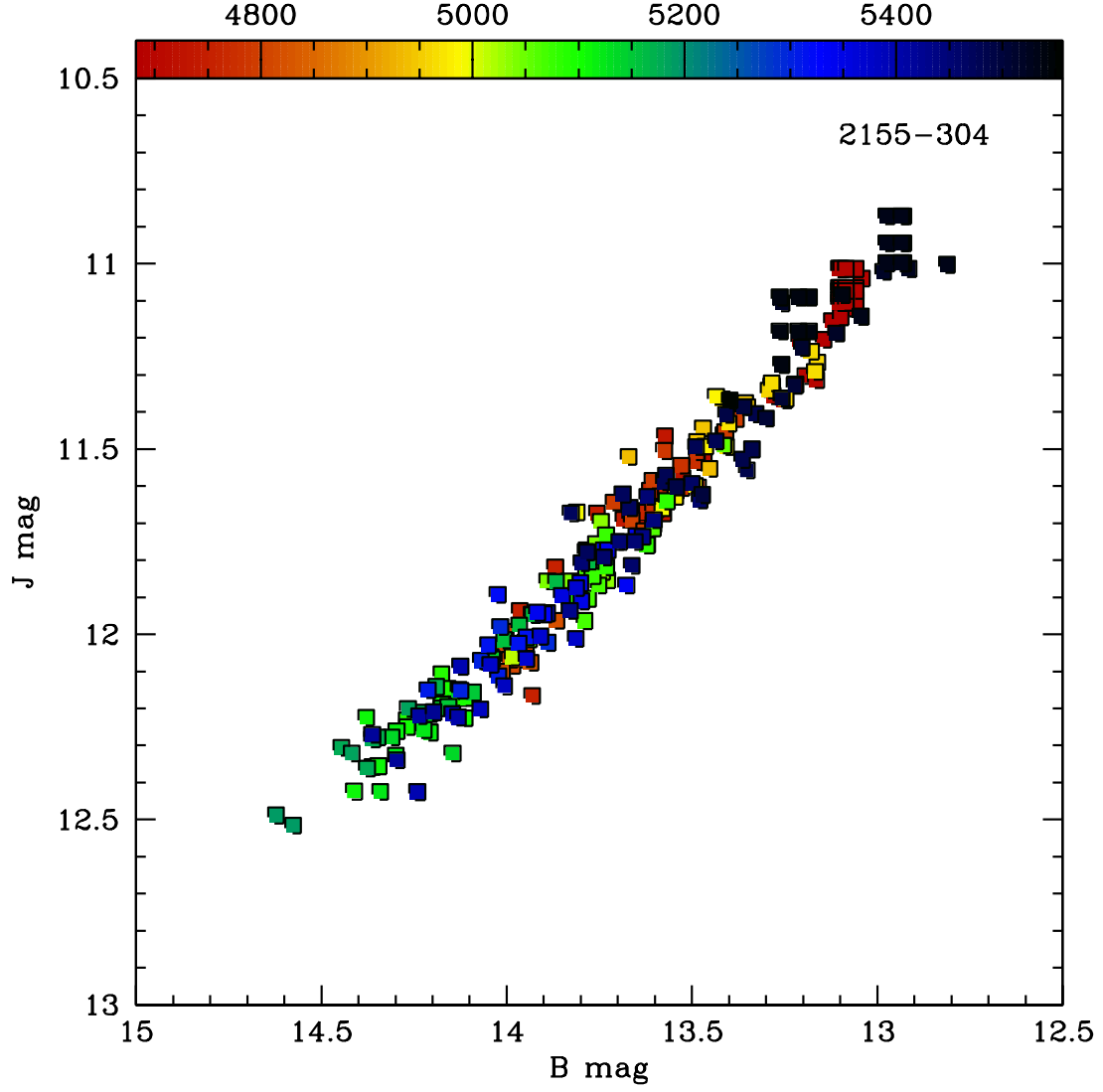


Fig. 3a: J -band vs B -band magnitude for the HBL PKS 2155-304. Color indicates the date of the observation, as shown in the top bar in MJD-50000. The tight correlation indicates that the optical and infrared emission vary together, with no significant delay.

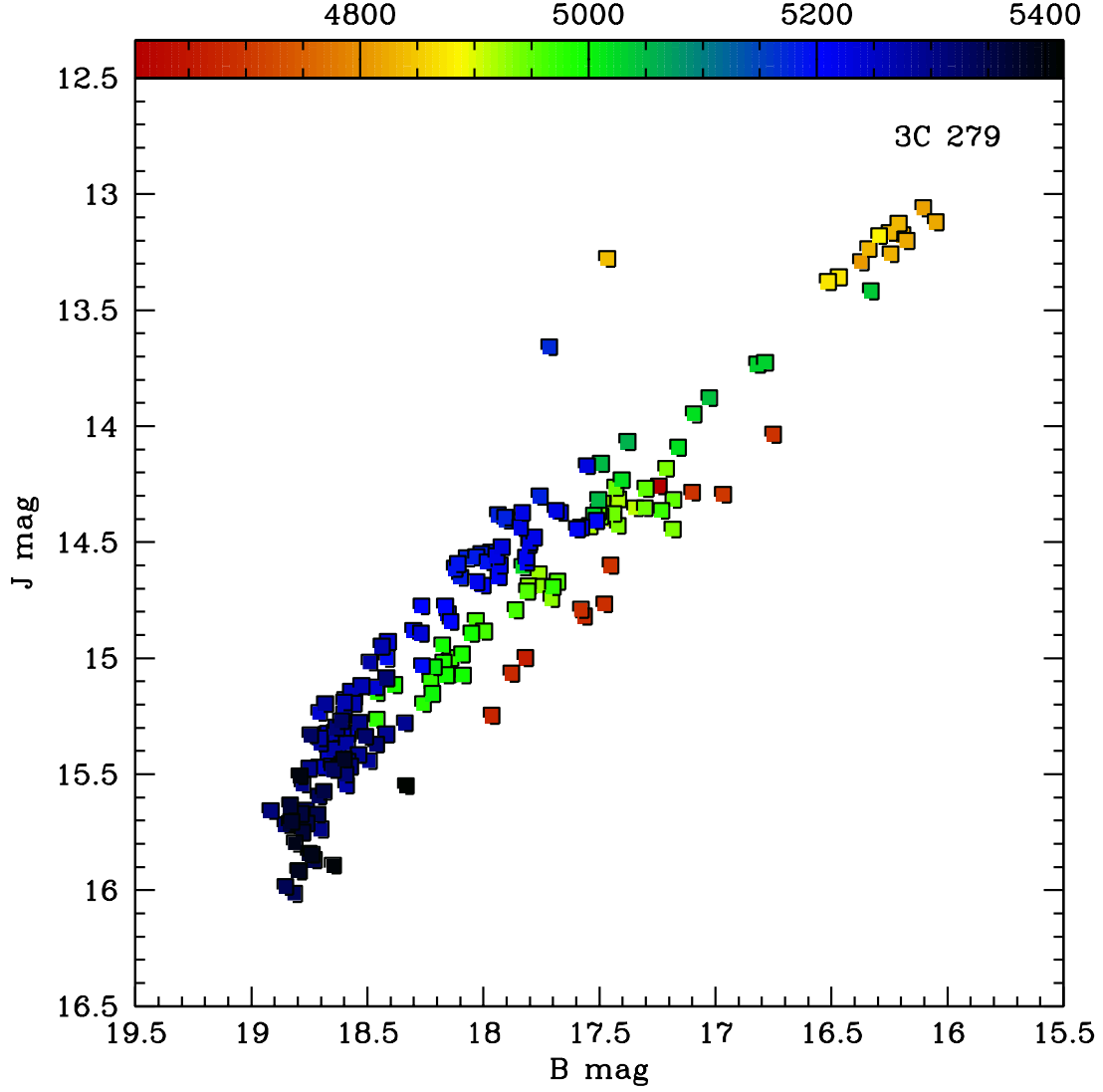


Fig. 3b: J -band vs B -band magnitude for the luminous FSRQ 3C 279, with colors as in Fig. 3a. As in all sources observed, optical and infrared emission varies together. The distinct tracks for the red, green, and blue reflect changes optical/IR spectral shape over time (*cf.* Fig. 5b).

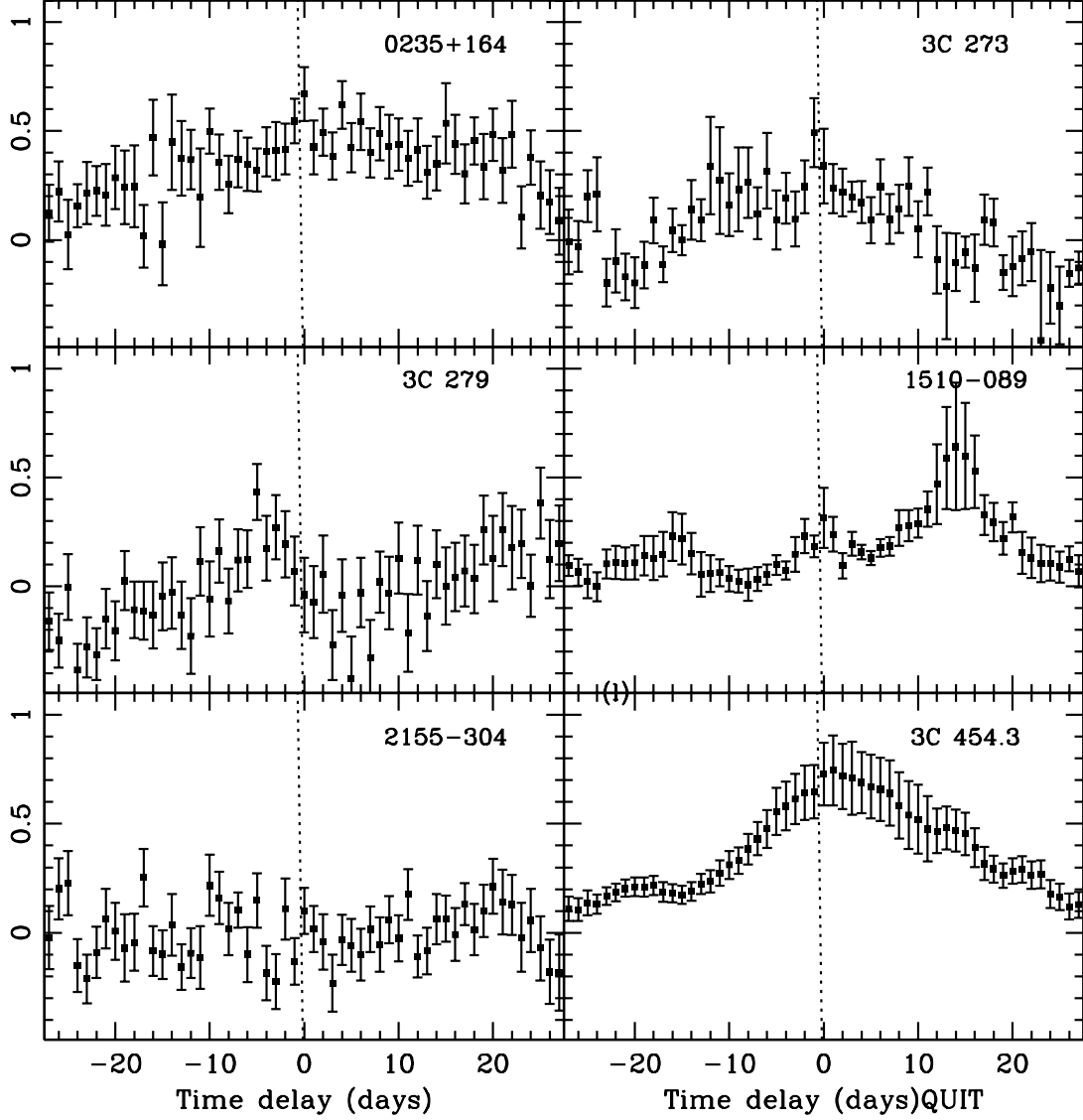


Fig. 4: Discrete correlation functions (DCF) for $\gamma - J$ -band light curves shown in Figure 1. A positive time delay corresponds to J band lagging the gamma-rays. In several sources (3C 454.3, most clearly) the emission is well correlated with little or no lag. In others, the DCF is flat, suggesting no strong correlation (PKS 2155-304). In PKS 1510-089, the gamma-rays appear to lead the J band by a couple of weeks.

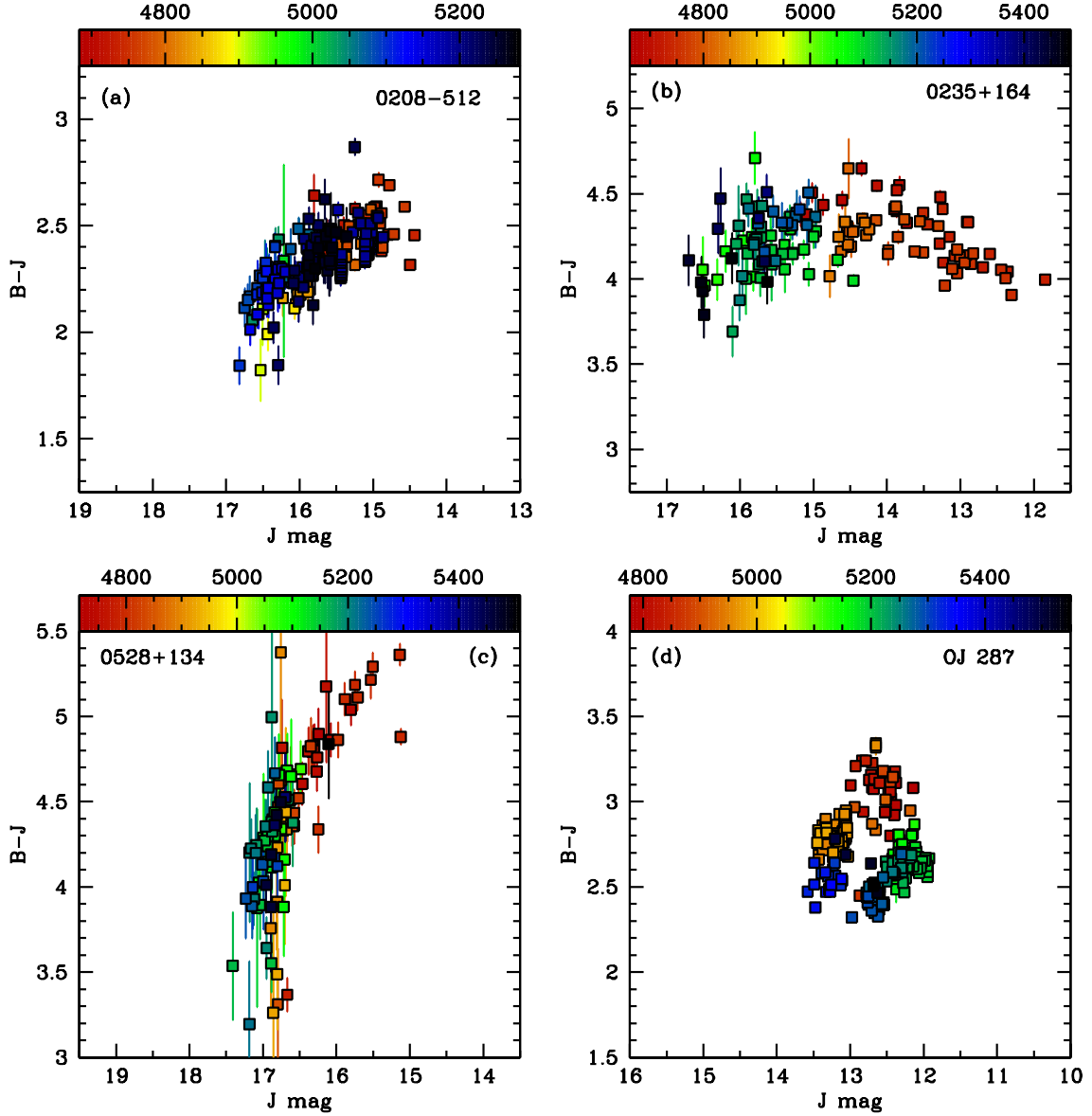


Fig. 5: $(B - J)$ color vs. J -band magnitude for FSRQs PKS 0208-512 and PKS 0528+134, and low-frequency peaked BL Lac objects AO 0235+164 and OJ 287. Color indicates the date of the observation, as shown in the top bar in MJD-50000. The FSRQs show an overall tendency to become bluer when fainter, which suggests the presence of a steady blue accretion disk component underlying the more variable jet emission. The two LBLs show more complicated behavior: AO 0235+164 shows some redder-when-brighter trend (blue-black points) but at early times (red-orange points) shows almost the opposite trend, getting bluer when brighter. During this bluer-when-brighter period, AO 0235+164 was very bright in gamma-rays and was easily detected by Fermi on daily time scales. When AO 0235+164 became fainter in the optical and was not detected in the daily LAT light curve, it shifted to the “normal” (for FSRQs) bluer-when-fainter trend. OJ 287 tends to move around on a circular locus in color-magnitude space where trends with brightness (including gamma-ray intensity) are not as easily definable.

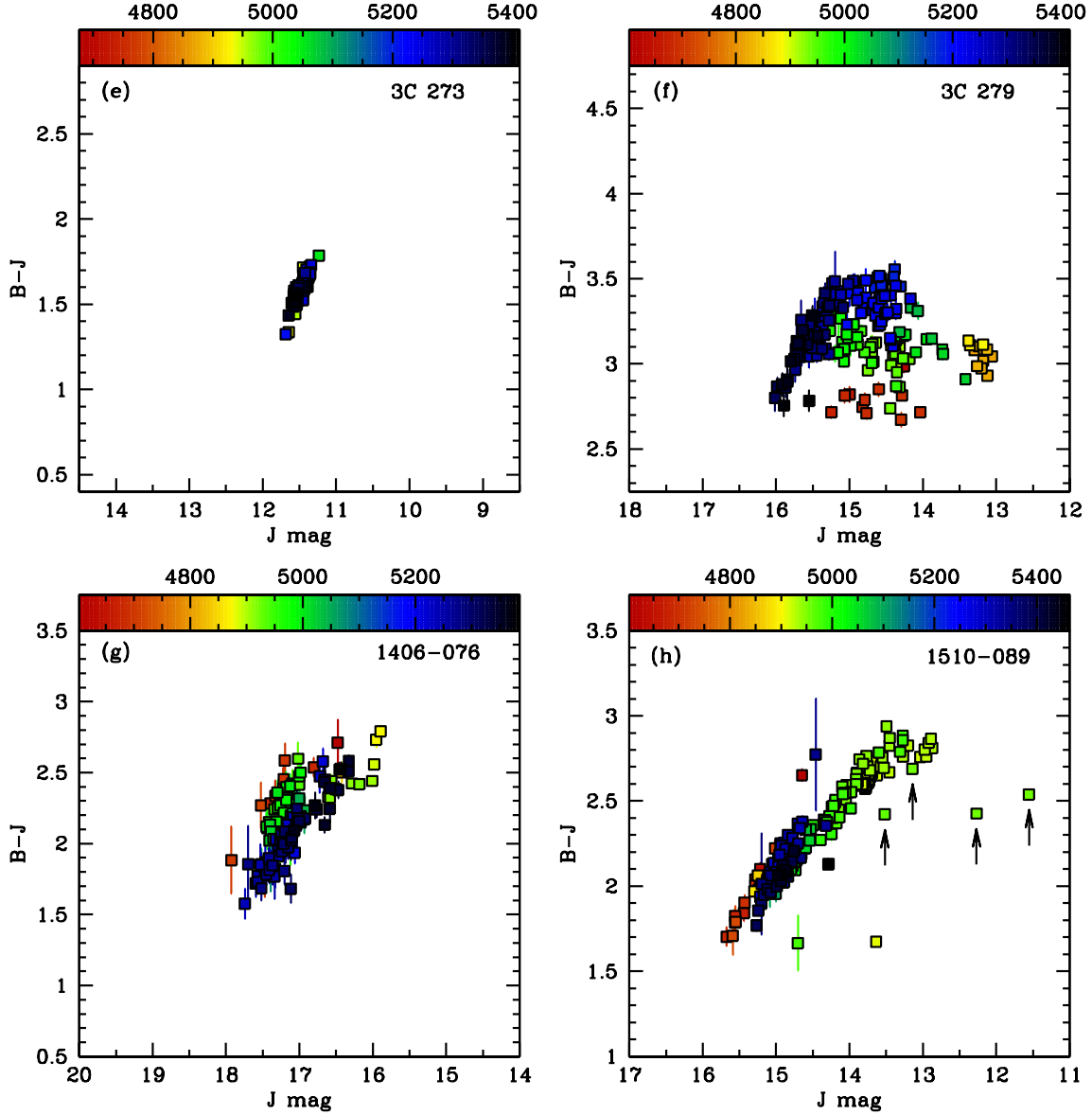


Fig. 5 (cont'd): $(B - J)$ color vs. J -band magnitude for FSRQs 3C 273, 3C 279, PKS 1406-076, and PKS 1510-089. Color indicates the date of the observation, as shown in the top bar in MJD-50000. All of these FSRQs show the overall redder-when-brighter (bluer-when-fainter) trend, consistent with a steady blue accretion disk component underlying the jet emission. Individual flares can behave differently; for example, the flare in PKS 1510-089 in May 2010 is achromatic (arrows indicate the 4 green points tracing a horizontal trend). The quasar 3C 279 shows compound behavior similar to AO 0235+164 (Fig. 5b), with the red-light green points tracing a horizontal loop in the color-magnitude figure before and just up to a period of bright gamma-ray activity (cf. Fig. 1f).

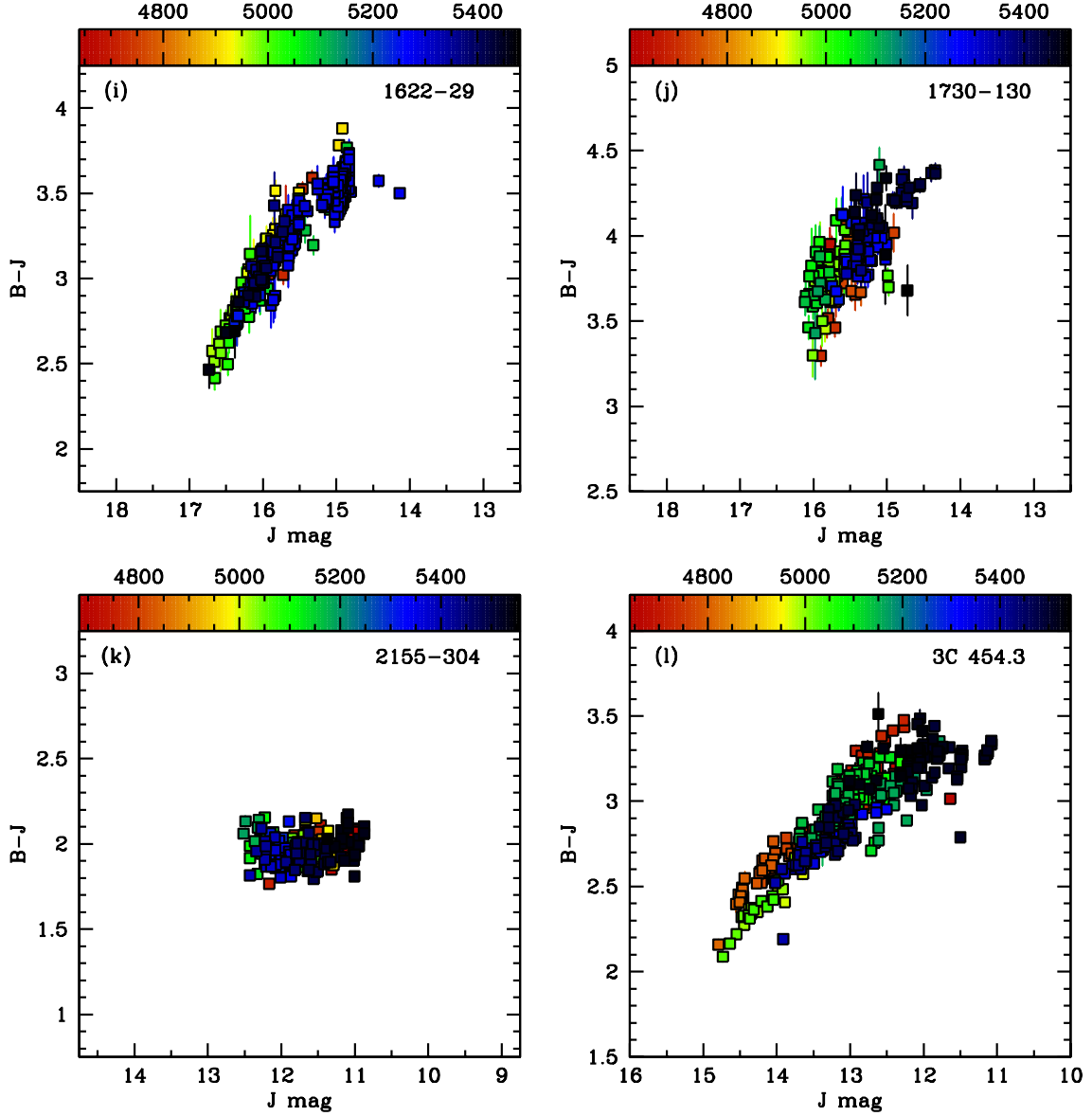


Fig. 5 (cont'd): $(B - J)$ color vs. J -band magnitude for FSRQs PKS 1622-29, PKS 1730-130, and 3C 454.3, and the HBL PKS 2155-304. Color indicates the date of the observation, as shown in the top bar in MJD-50000. The FSRQs show the redder-when-brighter trend. However, for the HBL, the brightness and spectral changes are relatively small, and there is no trend of color with magnitude. This may be because the HBL both lacks a luminous accretion disk and the optical jet emission in this object is below the synchrotron peak, thus optically thick and not highly variable.

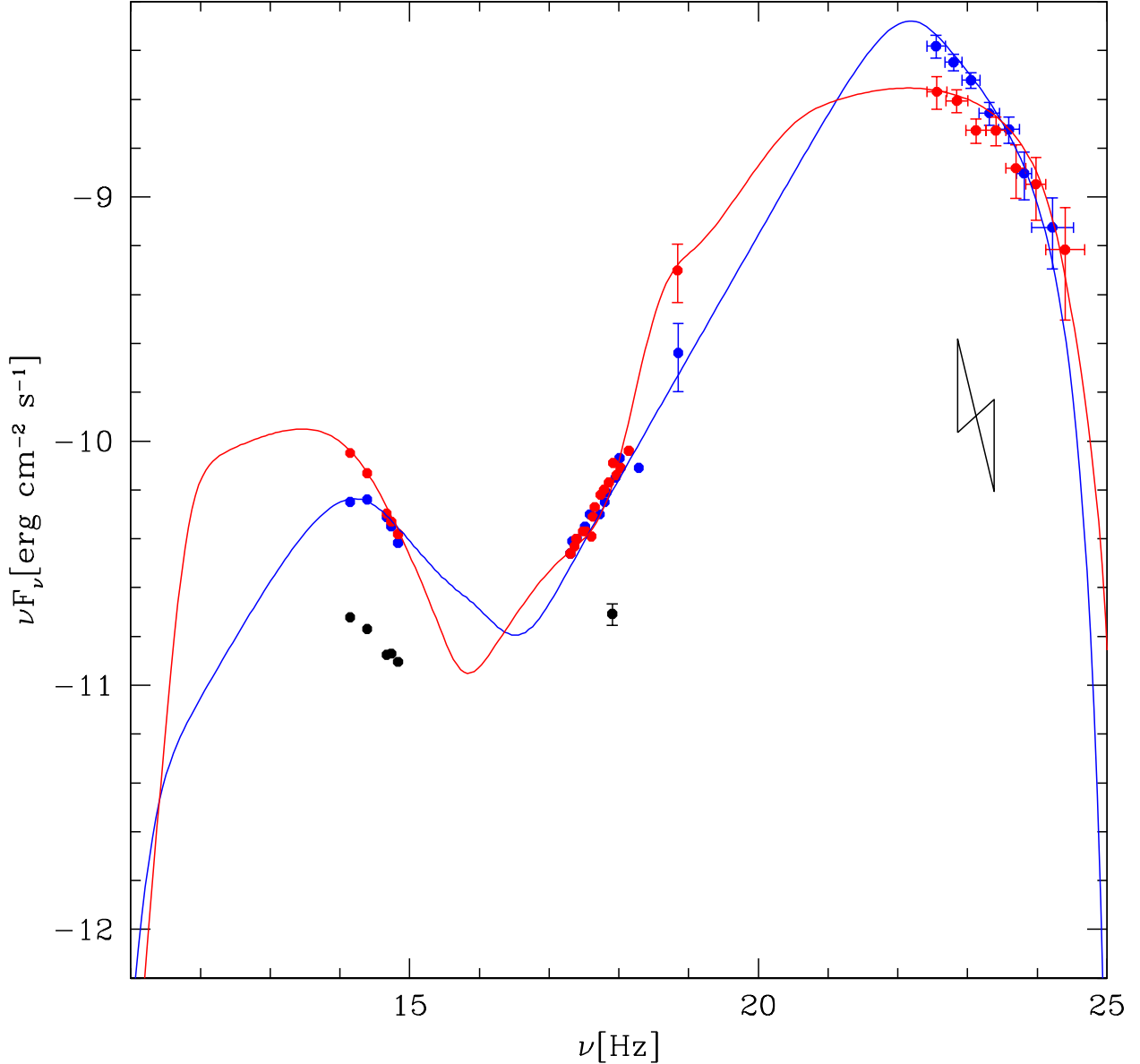
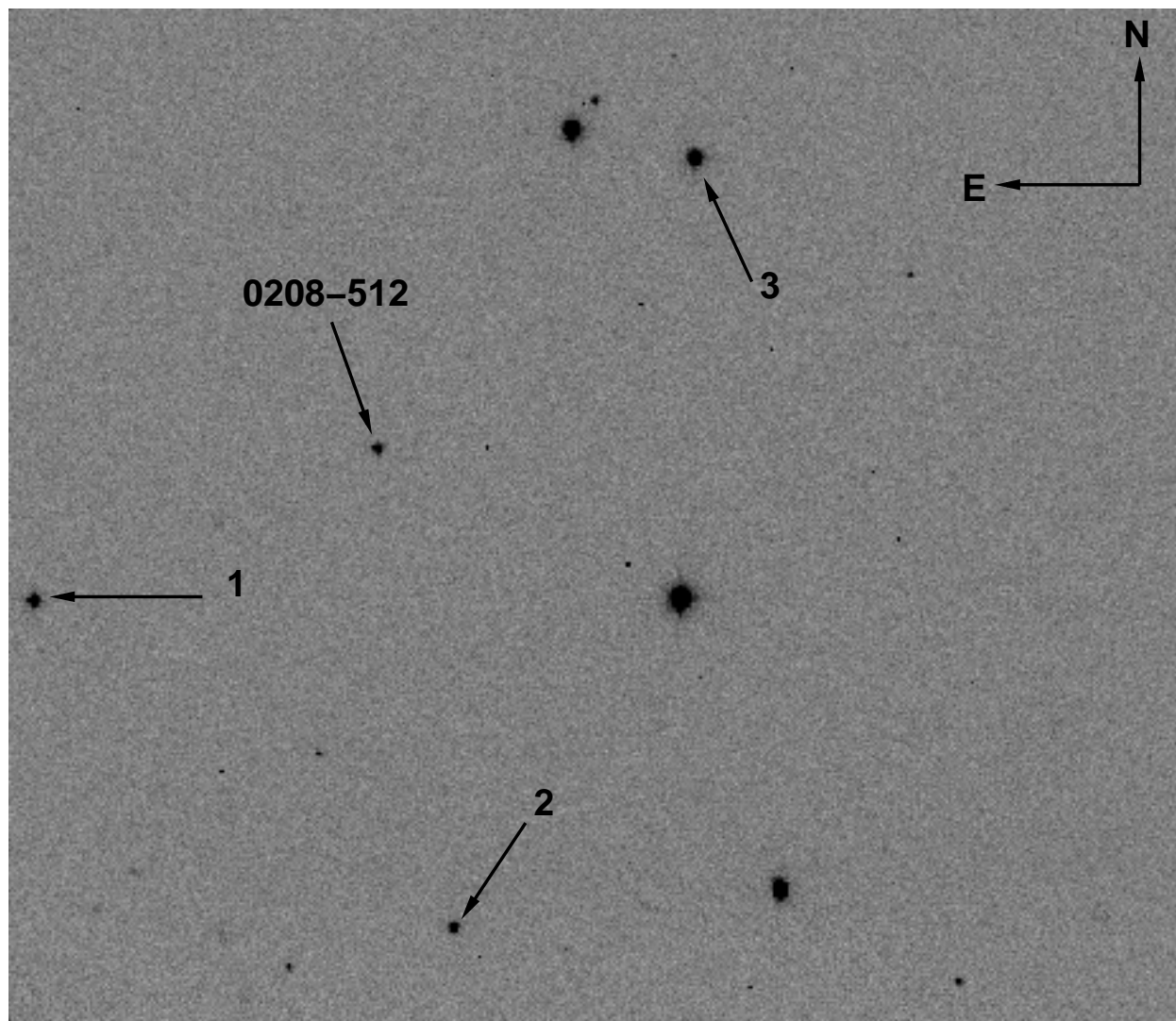


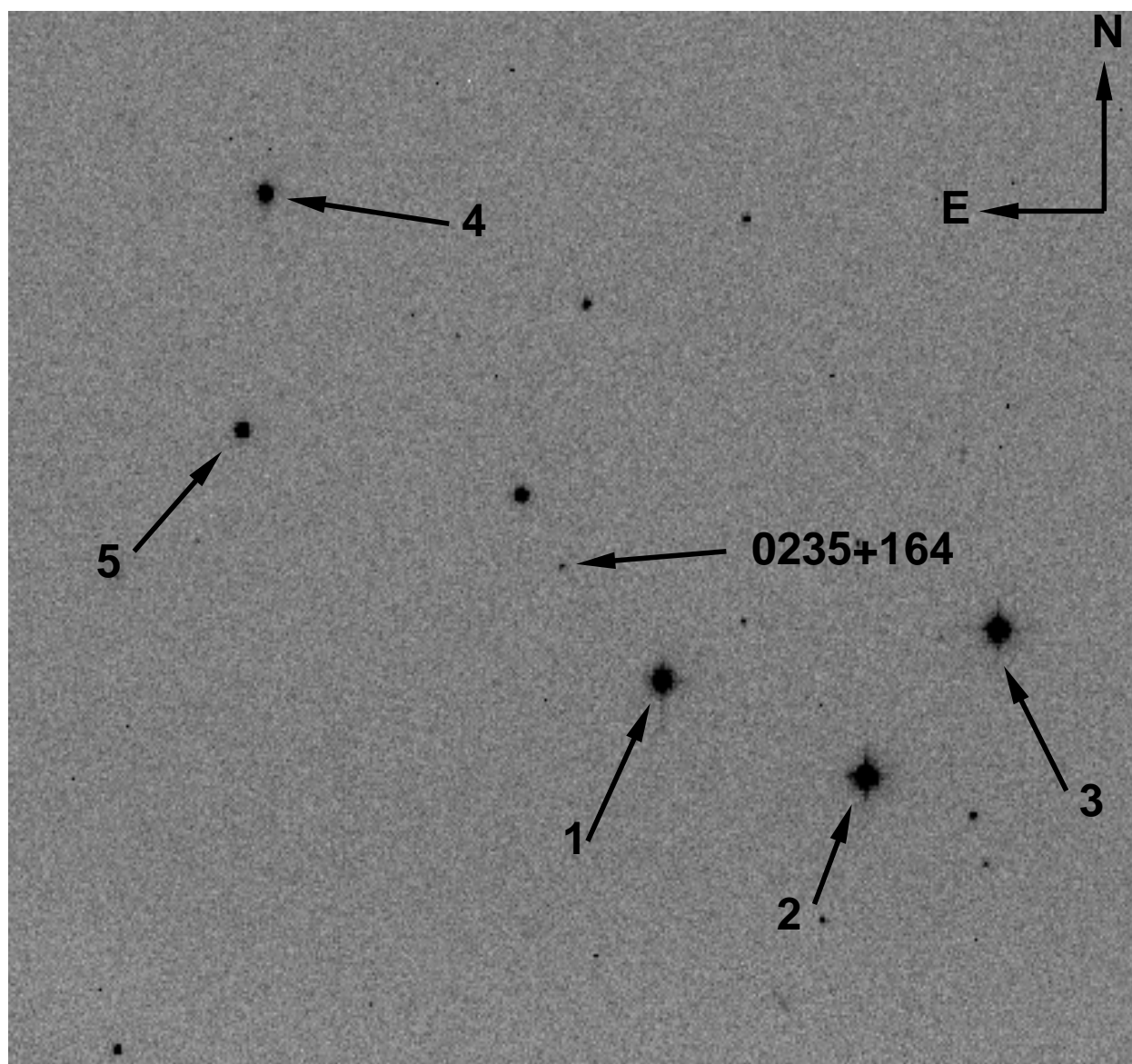
Fig. 6: Spectral energy distribution of 3C 454.3 from data obtained during the bright flare on UT Dec 03, 2009 (*blue points*) and UT Dec 04, 2009 (*red points*), and in a low state on UT Aug 12, 2009 (*black points*). Blue and red *lines* are model fits to the entire dataset using the one-zone code of Coppi (1992). Error bars on the optical and NIR points are smaller than the plotting symbol. The infrared SMARTS data clearly shows a change in synchrotron peak energy between December 3 and 4; modeling this together with the changing gamma-ray peak and slope poses challenges for simple single-zone models. However, these simple fits are sufficient to indicate that Klein-Nishina effects are likely important and that the optical-IR is produced by higher energy electrons than are producing the gamma rays.

A. Optical Finding Charts

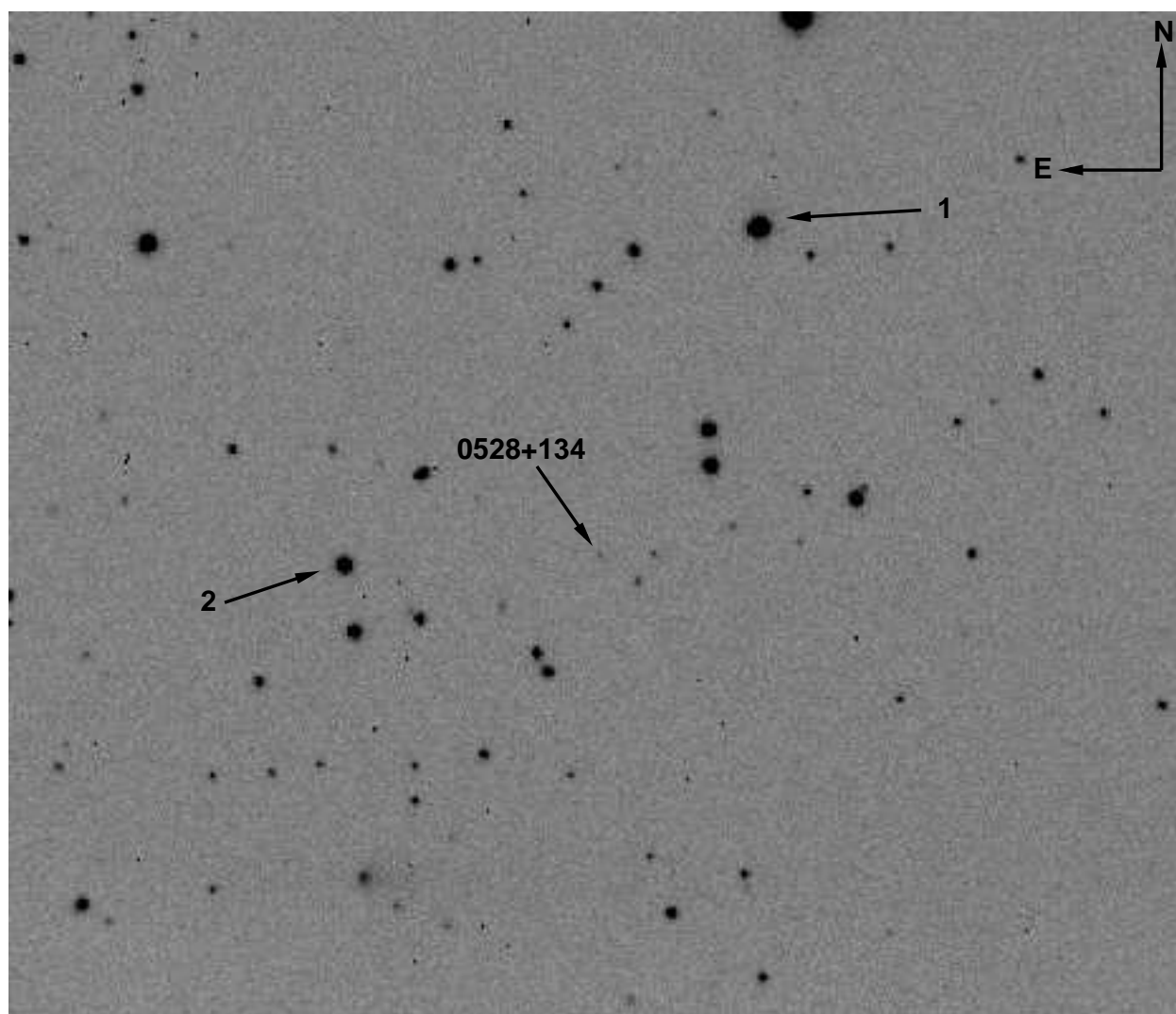
We present optical finding charts for each of the 12 SMARTS-monitored blazars discussed in this paper. All figures are V -band. Field of view is approximately $6' \times 6'$. North is at top of image, East is to the left. Comparison stars are numbered; calibrated magnitudes for our comparison stars are given in Appendix C.



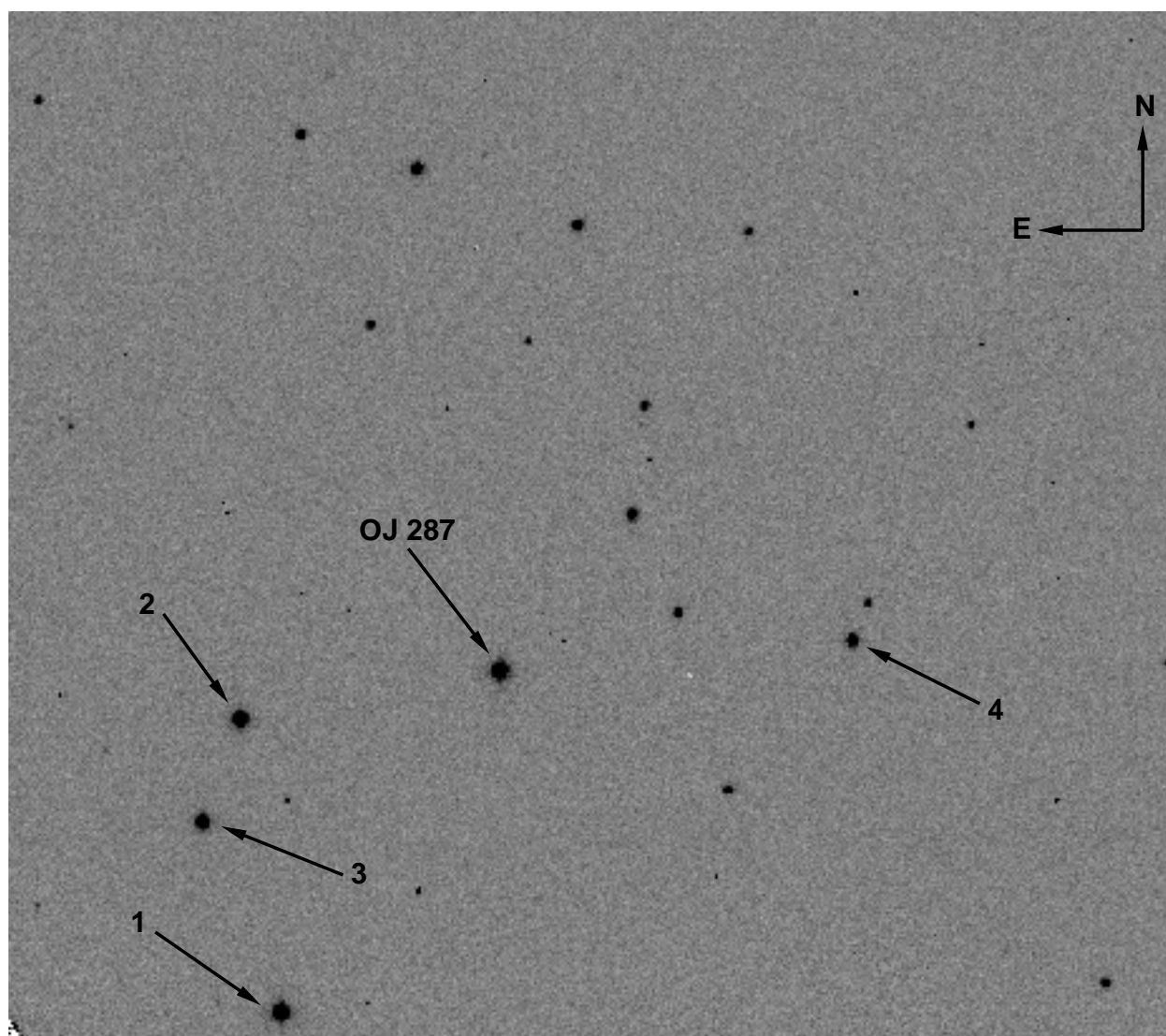
A.1: PKS 0208–512.



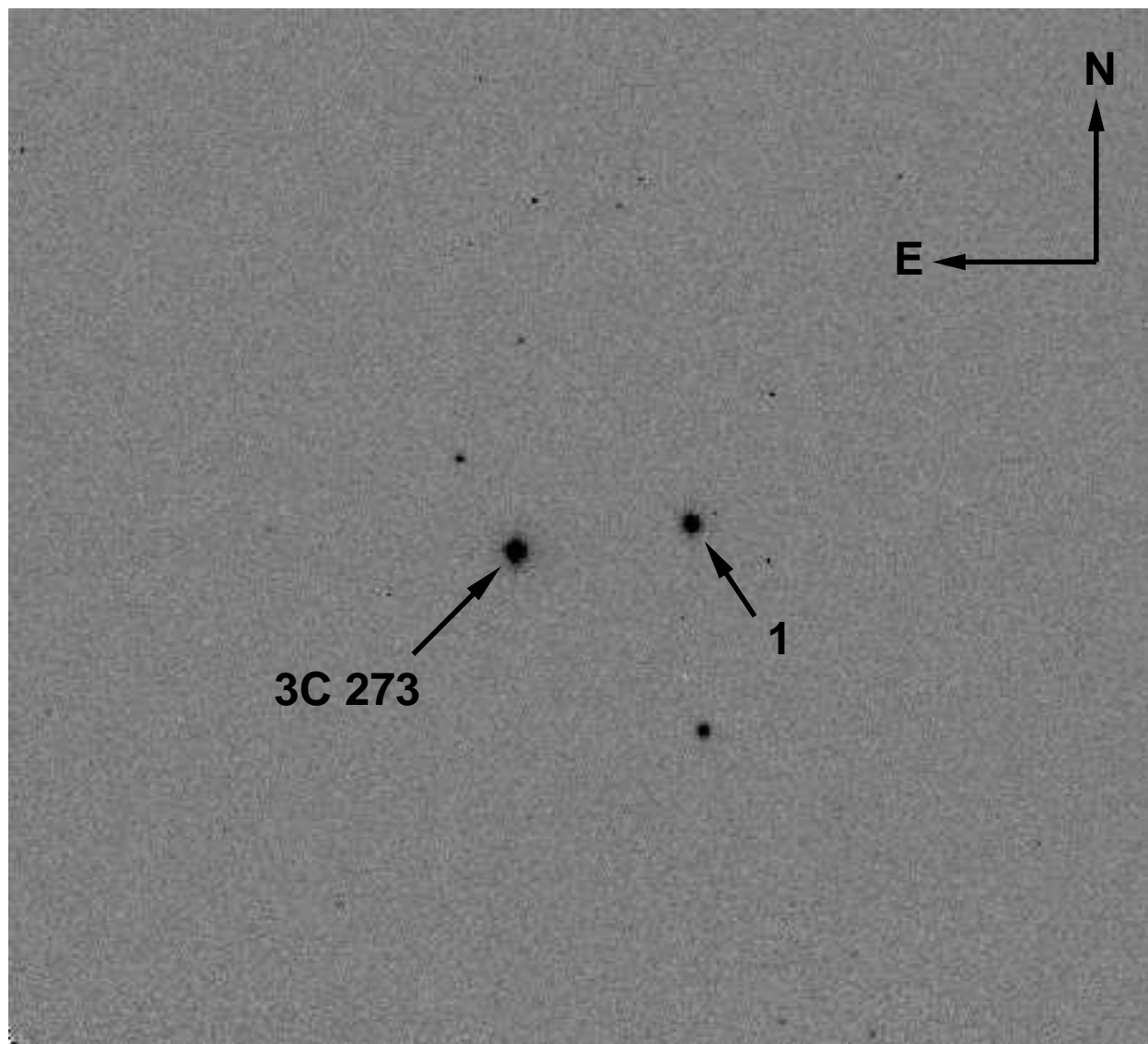
A.2: AO 0235+164.



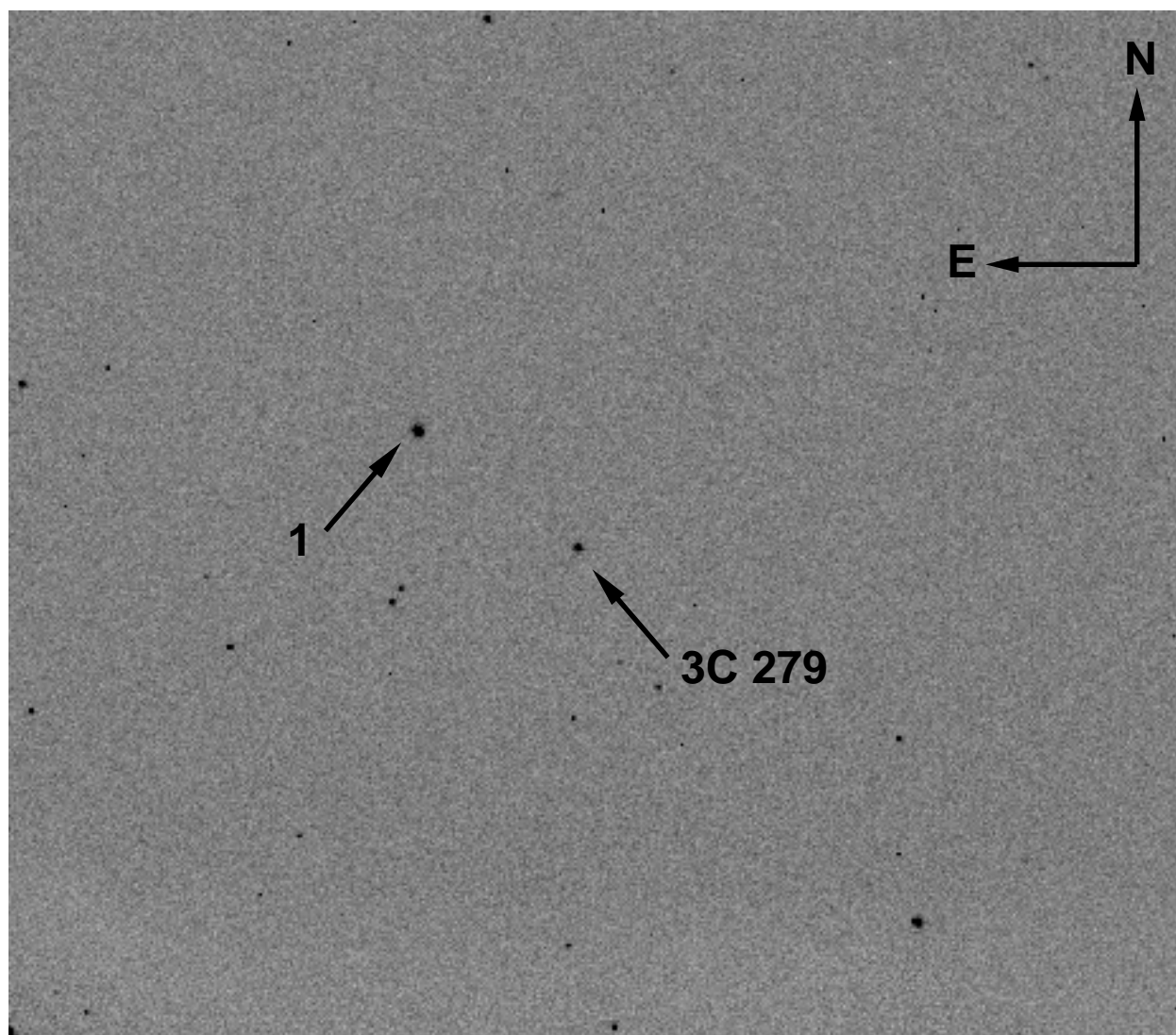
A.3: PKS 0528+134.



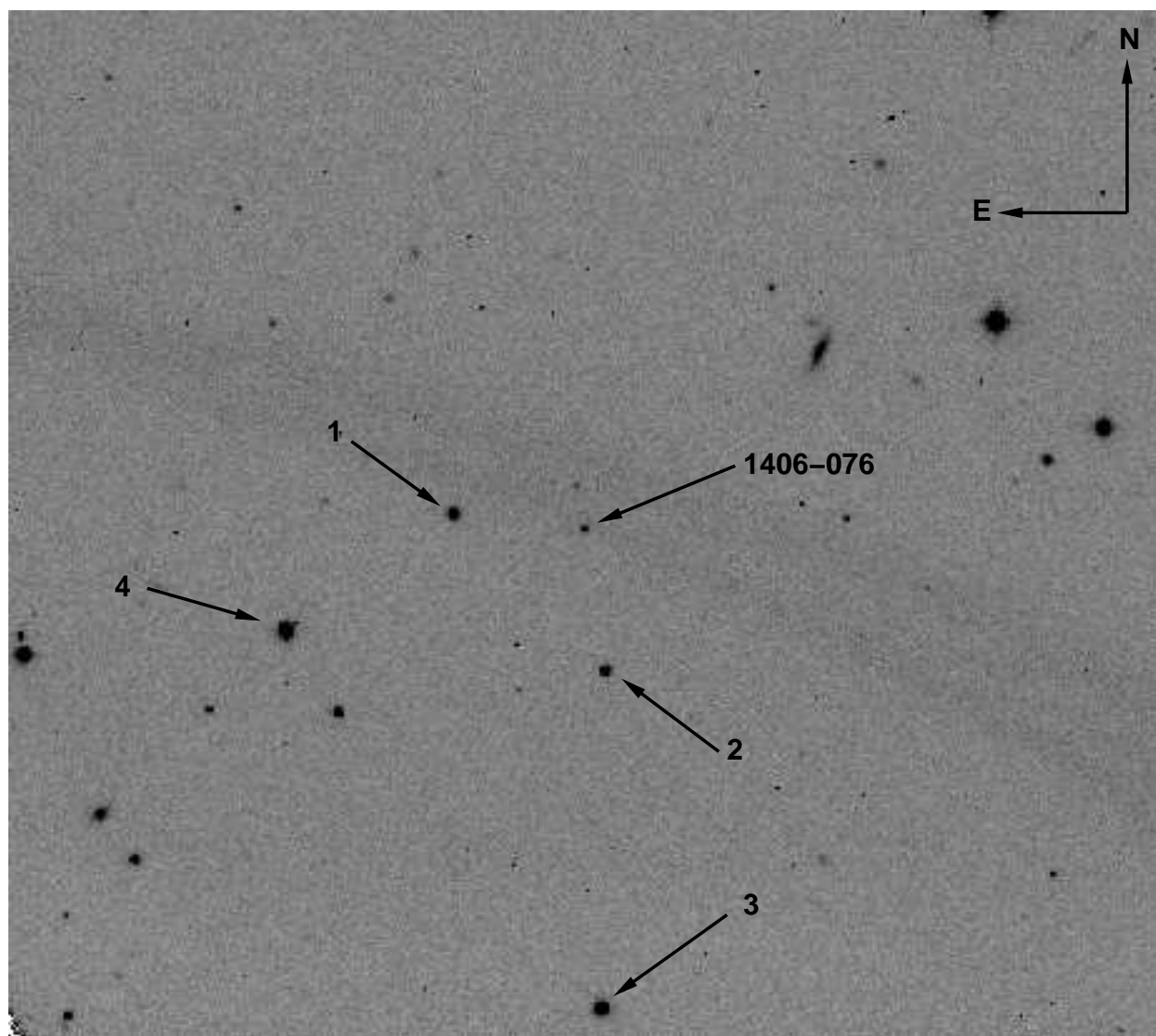
A.4: OJ 287.



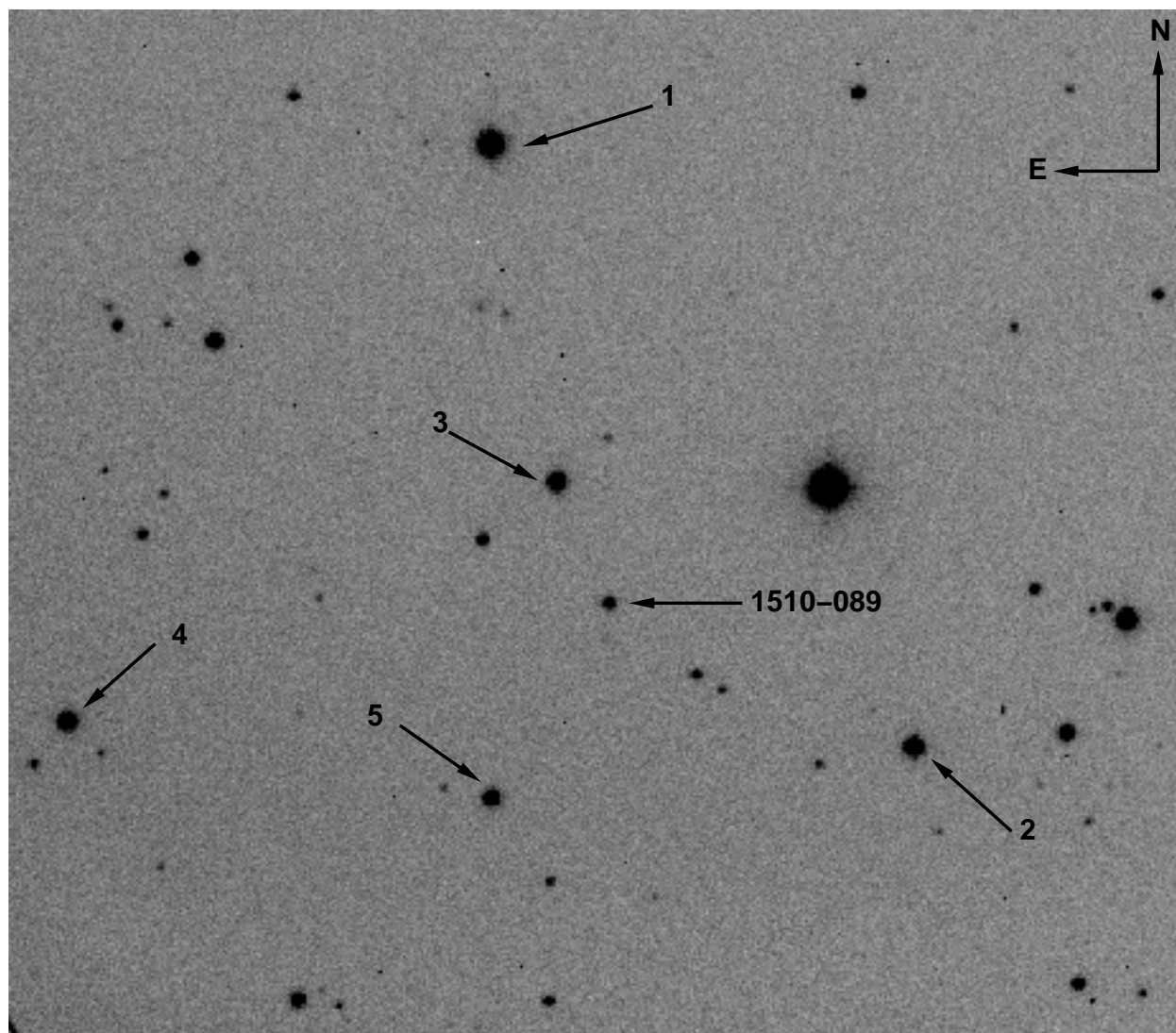
A.5: 3C 273.



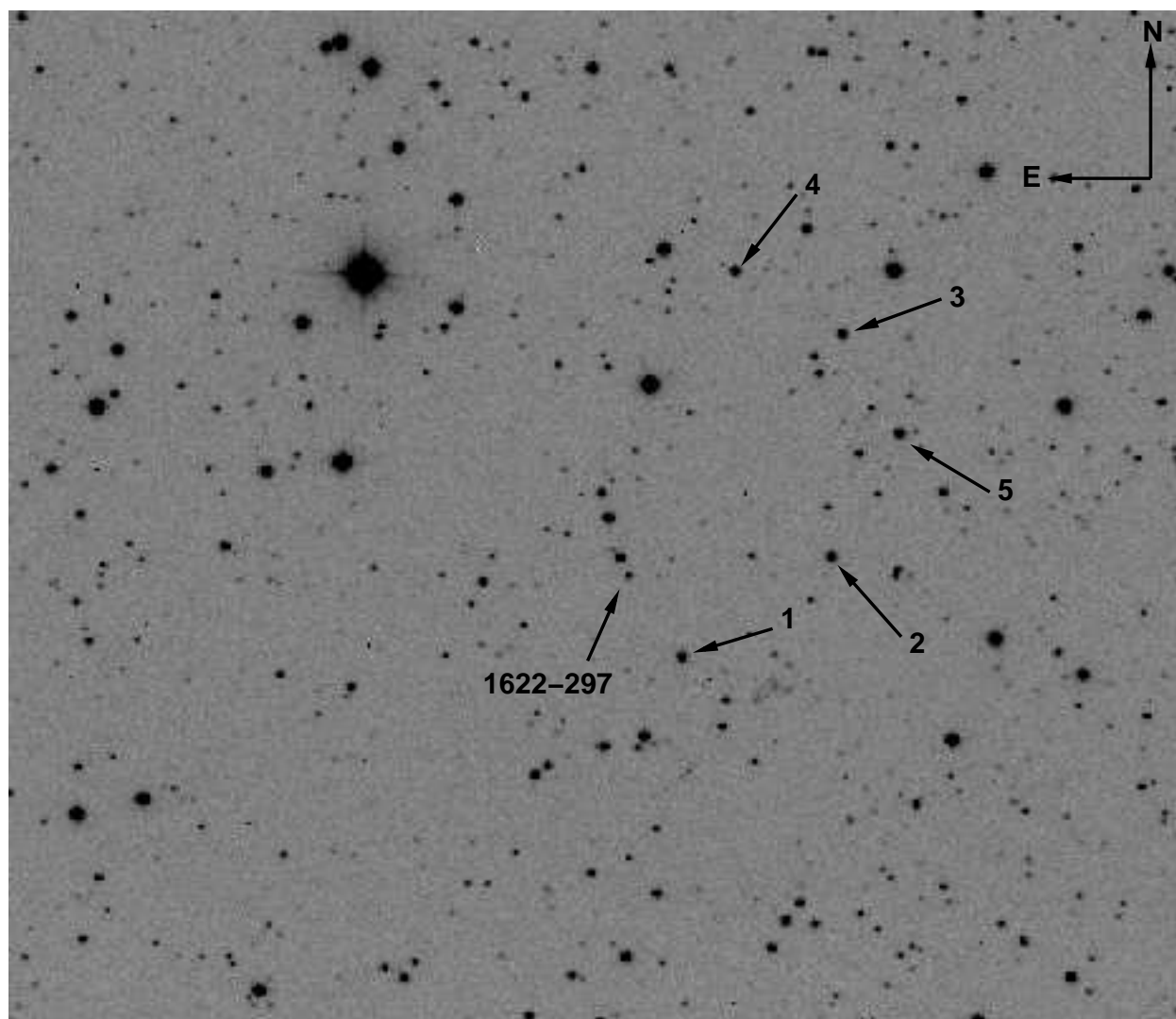
A.6: 3C 279.



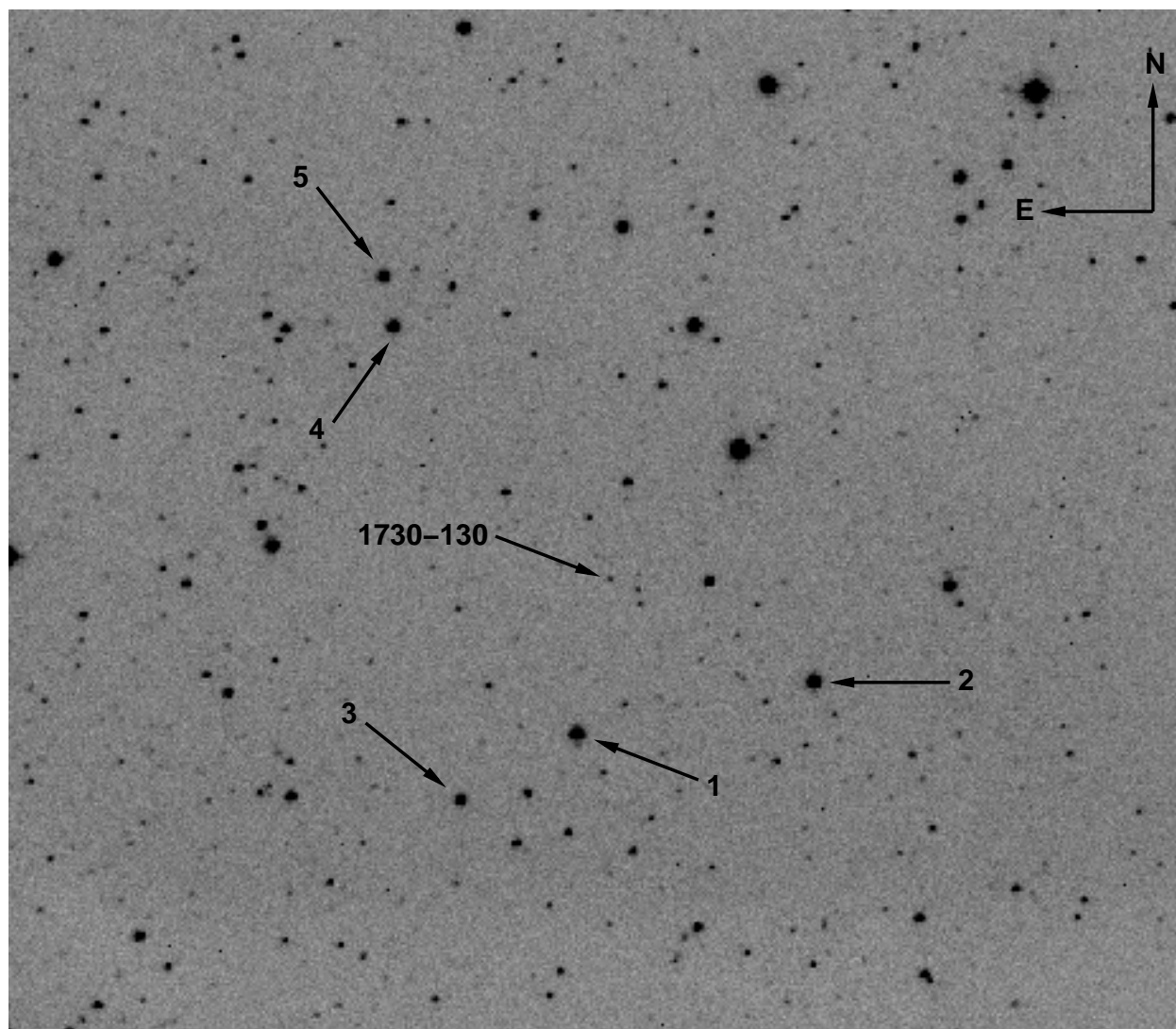
A.7: PKS 1406–076.



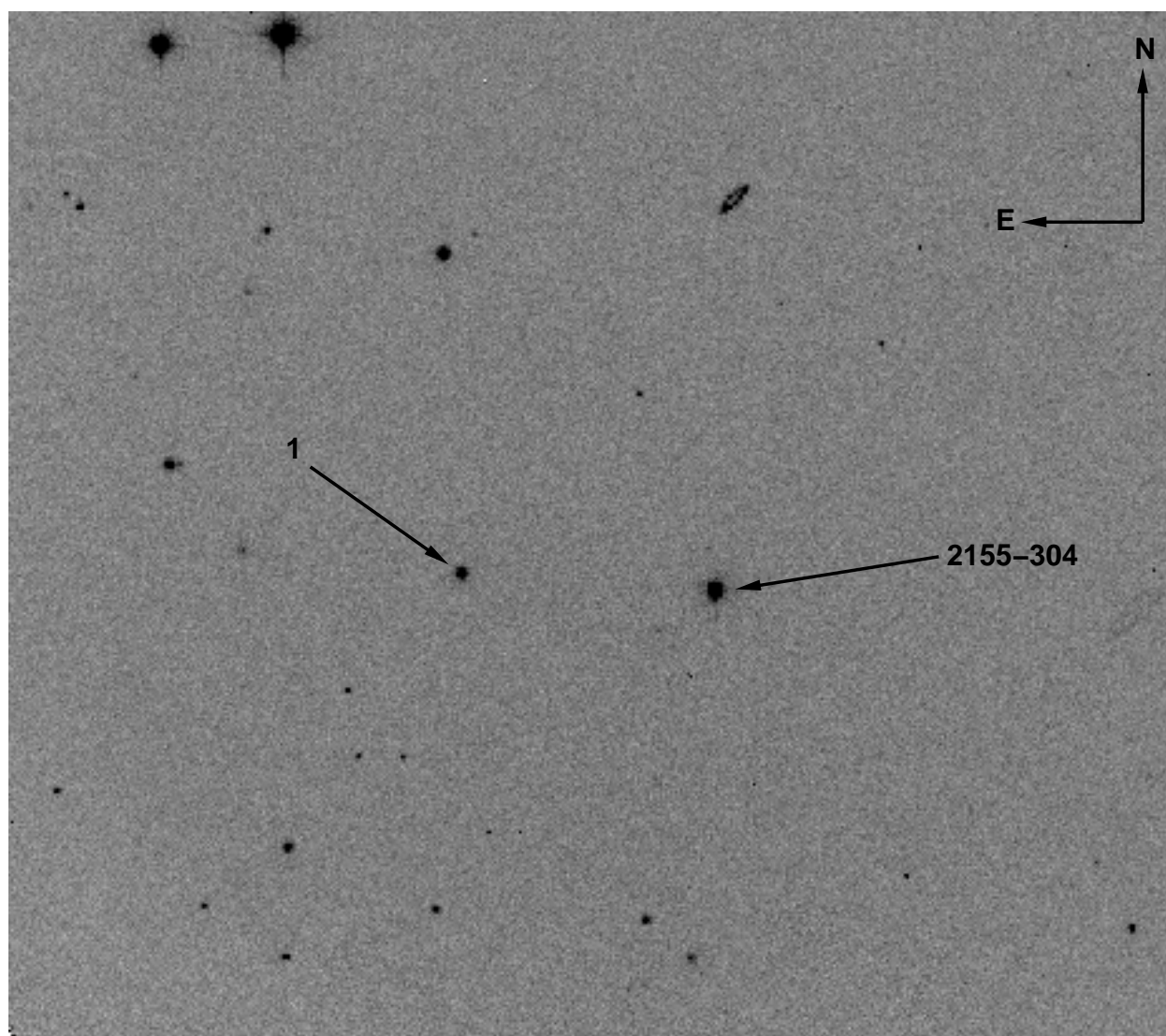
A.8: PKS 1510–089.



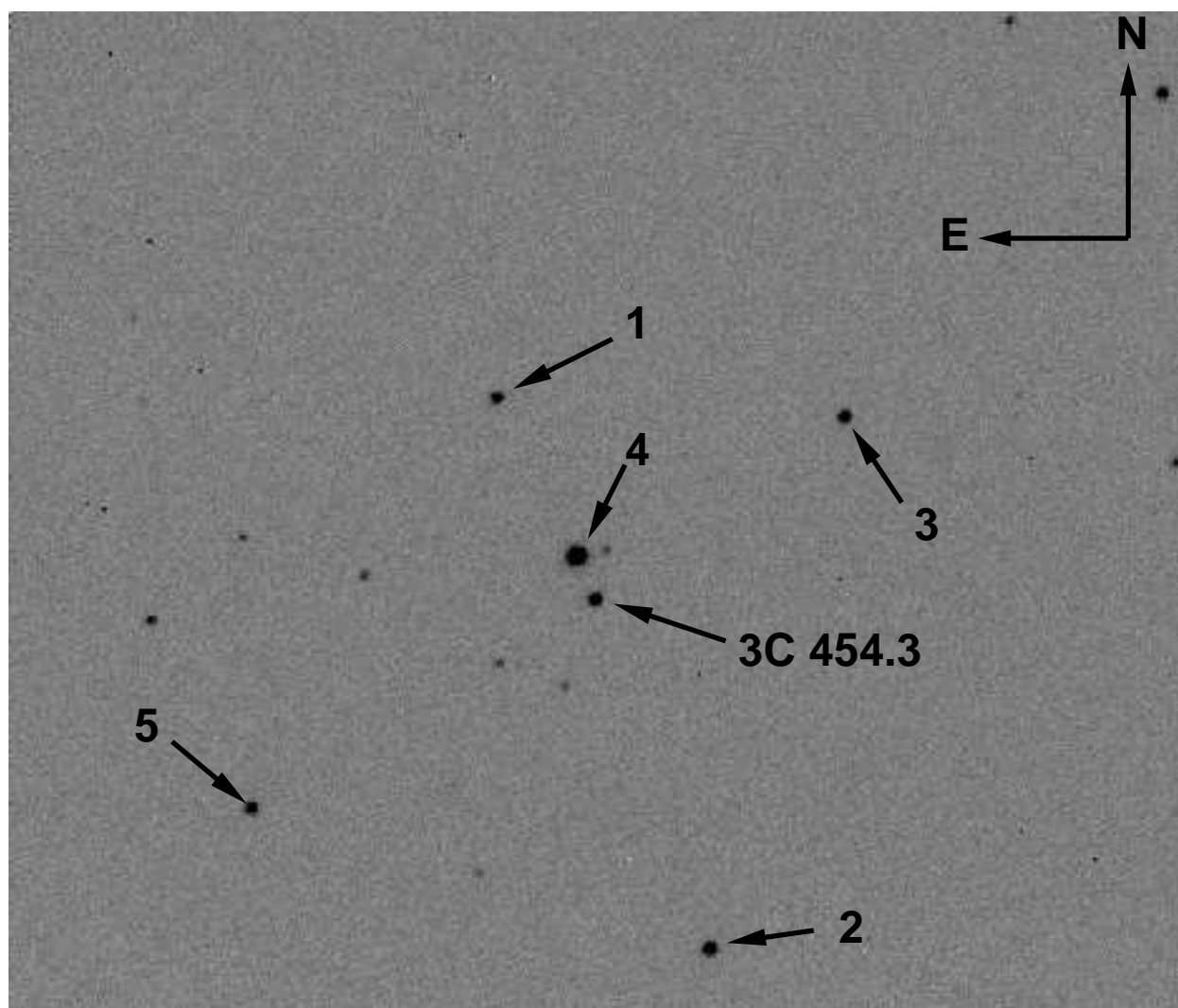
A.9: PKS 1622–297.



A.10: PKS 1730–130.



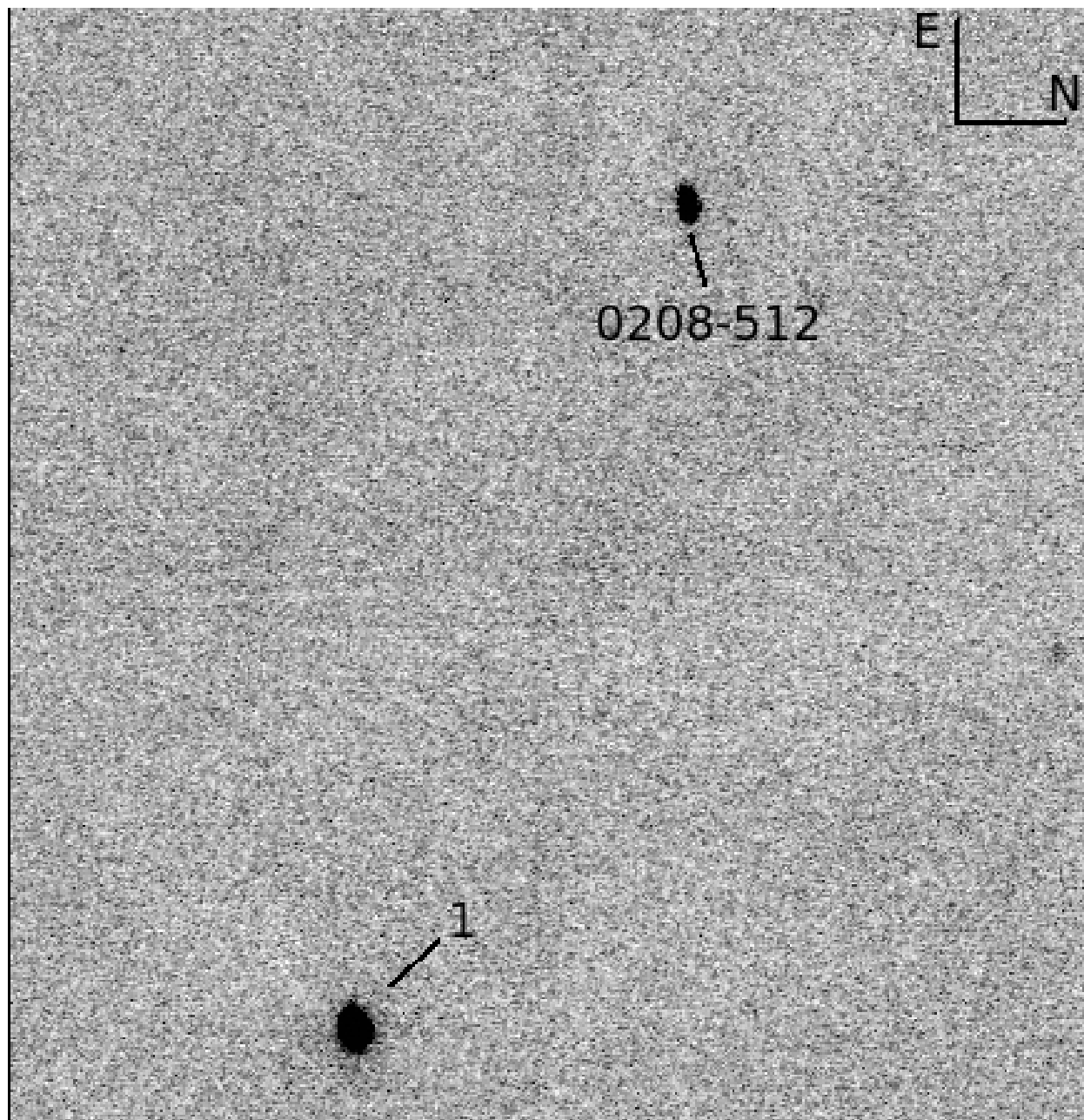
A.11: PKS 2155–304.



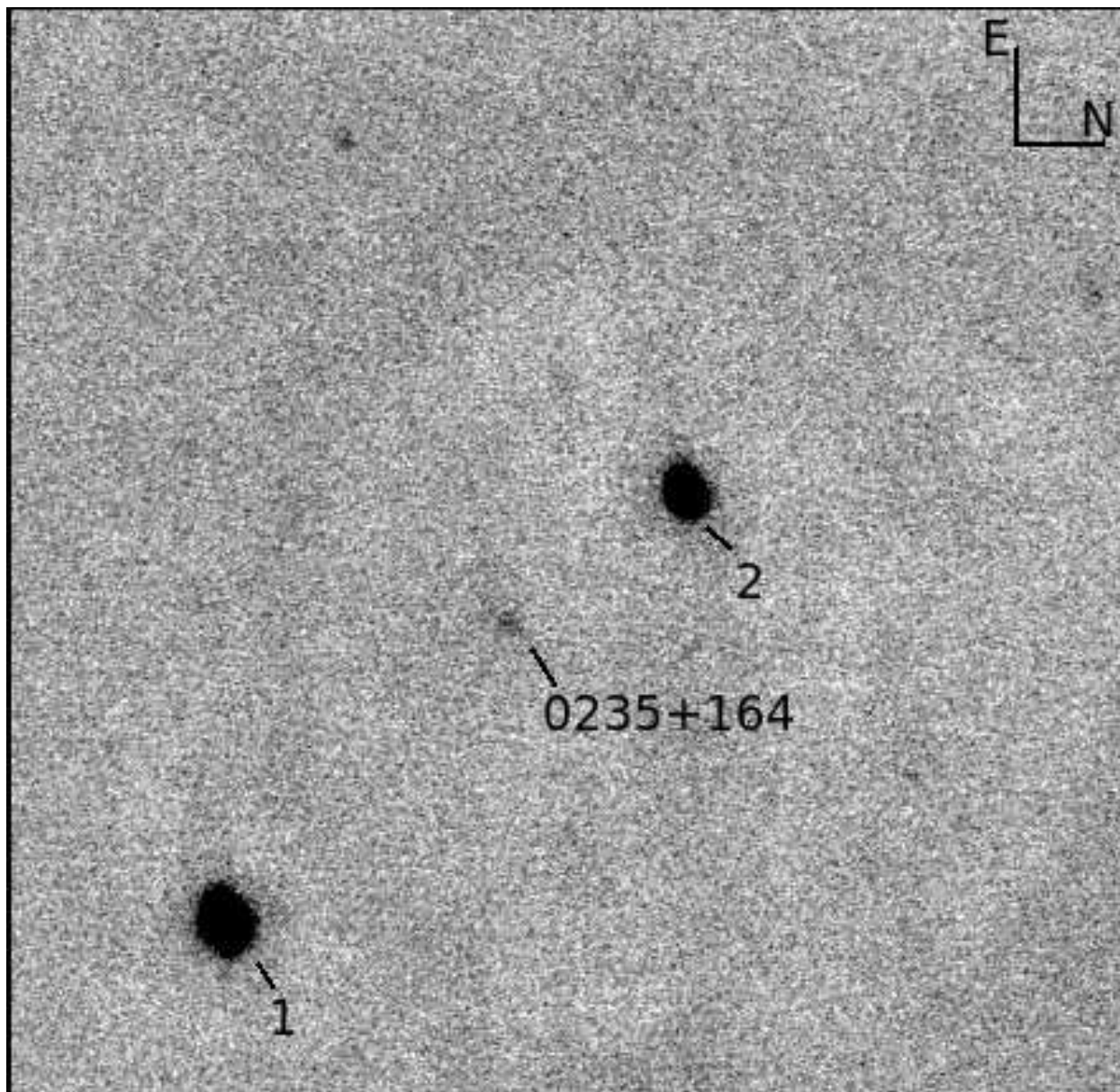
A.12: 3C 454.3.

B. Near-Infrared Finding Charts

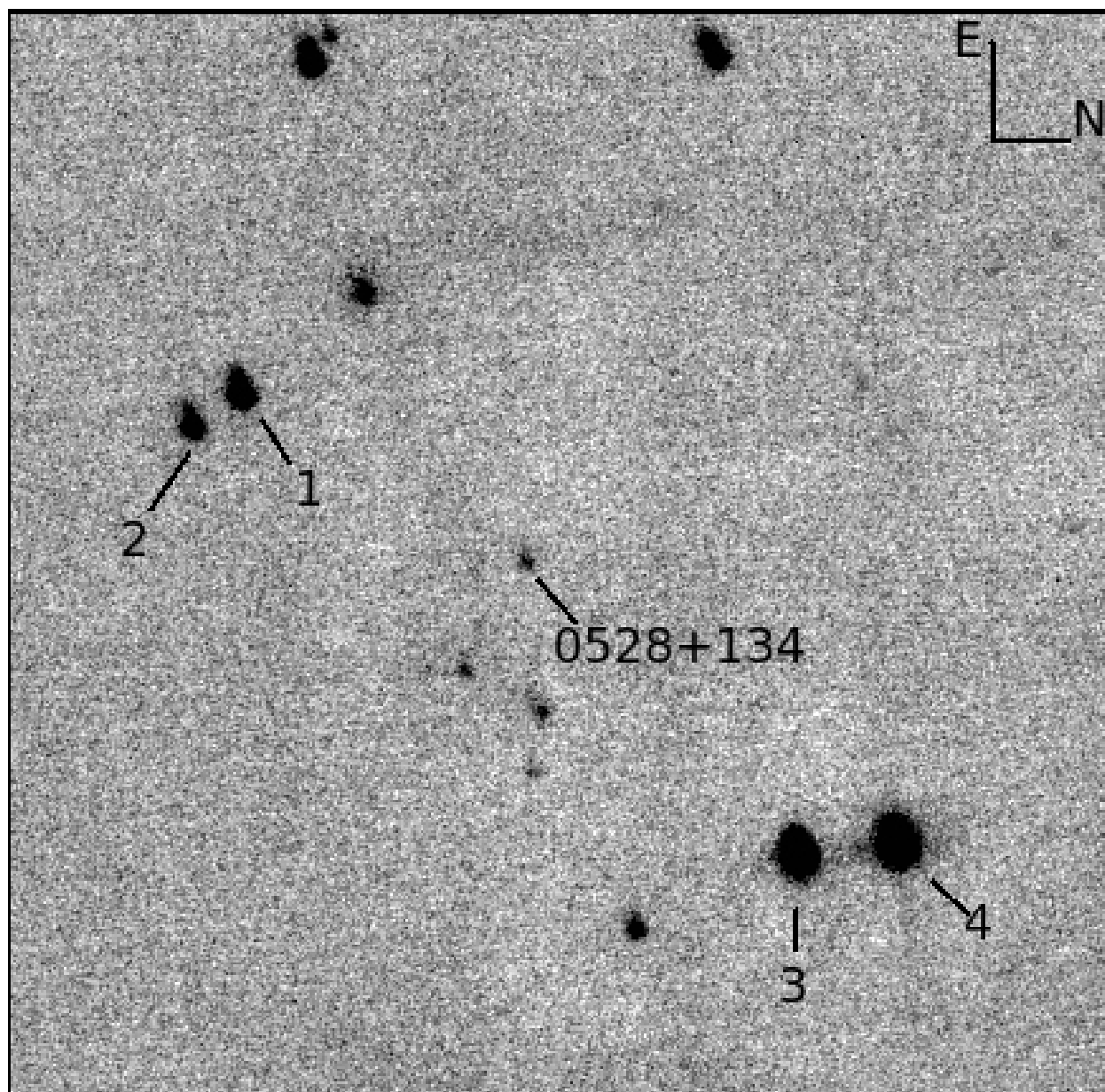
We present near-infrared finding charts for each of the 12 SMARTS-monitored blazars discussed in this paper. All figures are J -band. Field of view is approximately $2' \times 2'$. North is to the right of image, East is at the top. Comparison stars are numbered; calibrated magnitudes for our comparison stars are given in Appendix C.



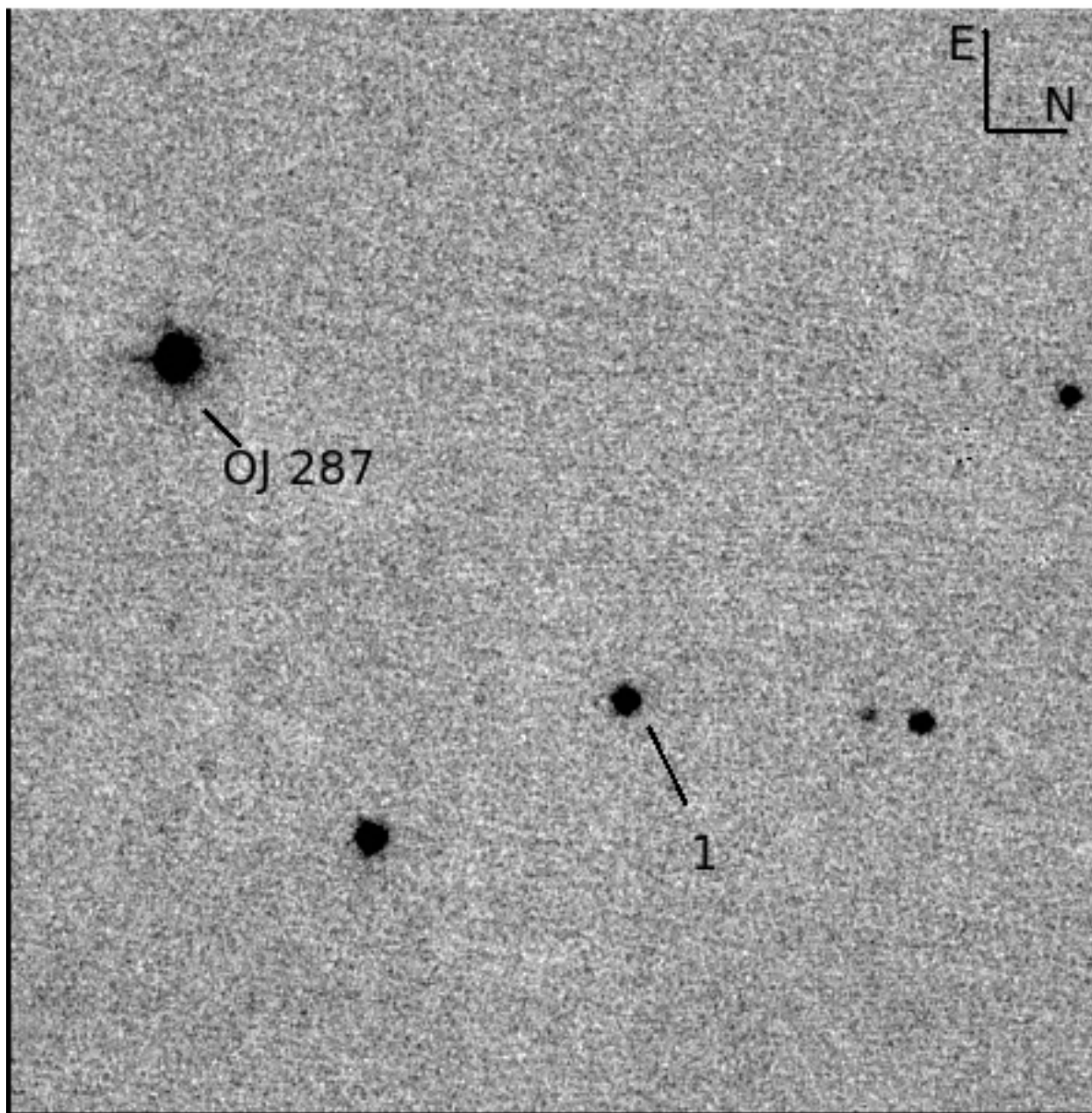
B.1: PKS 0208–512.



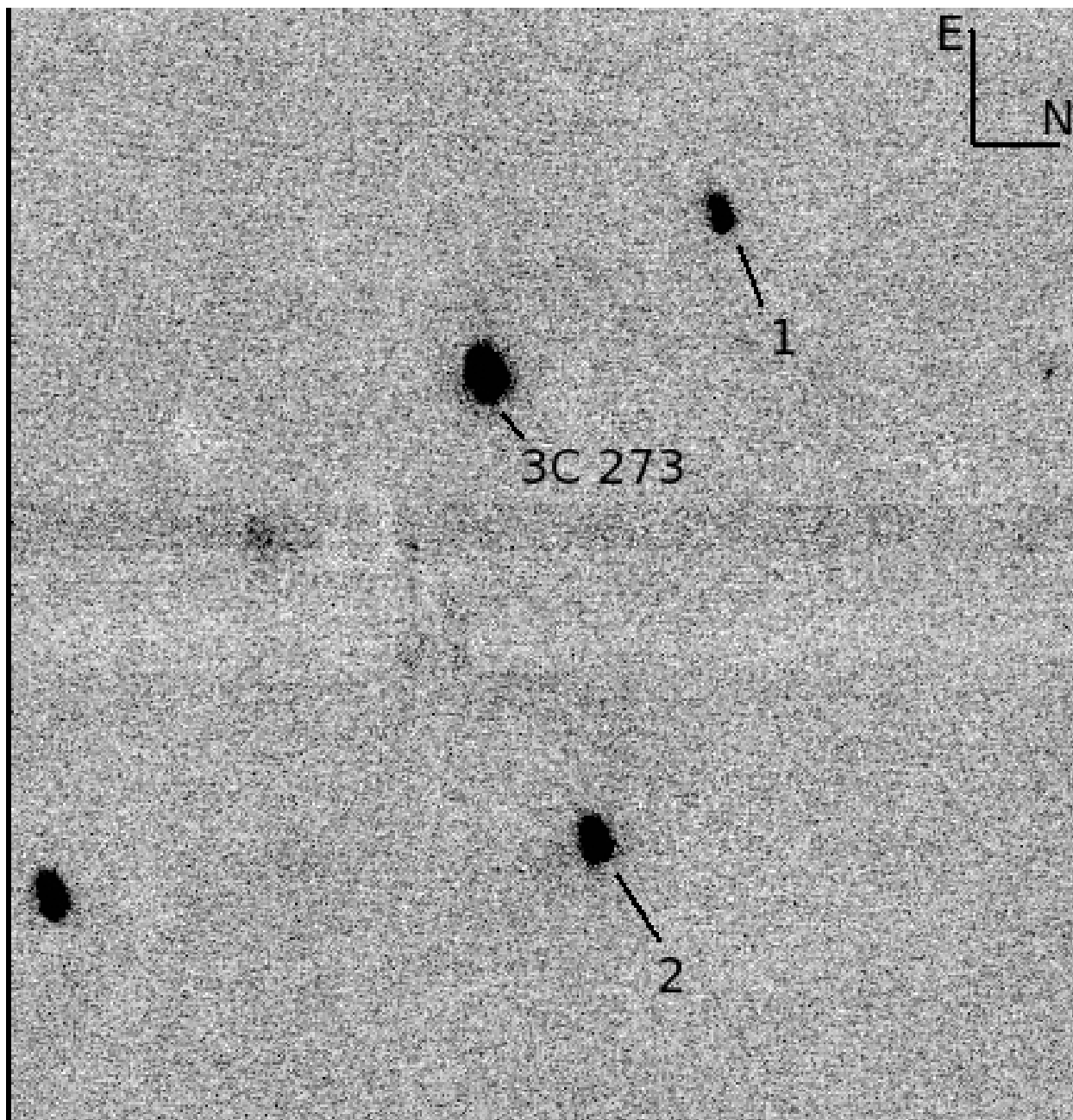
B.2: AO 0235+164.



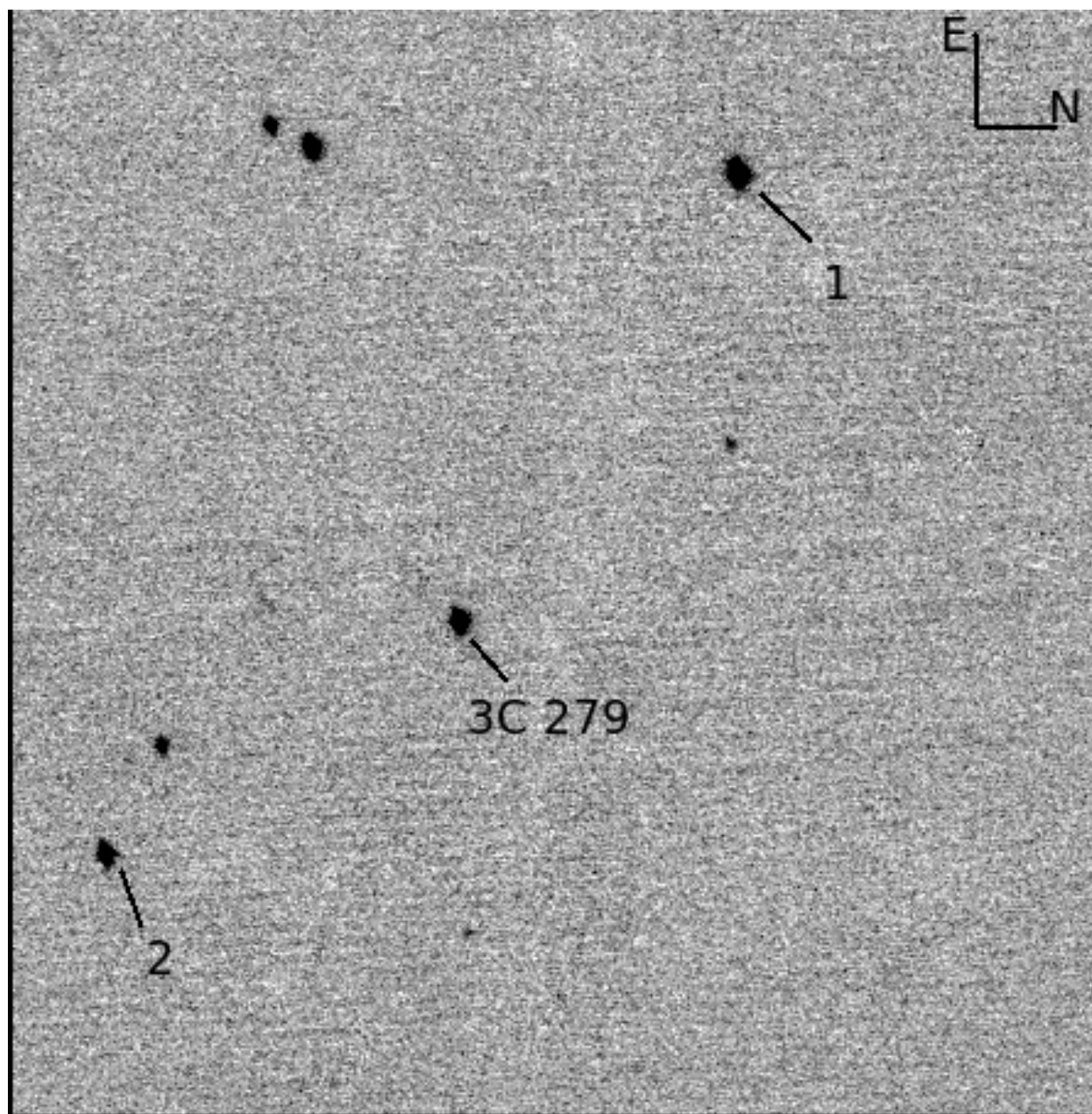
B.3: PKS 0528+134.



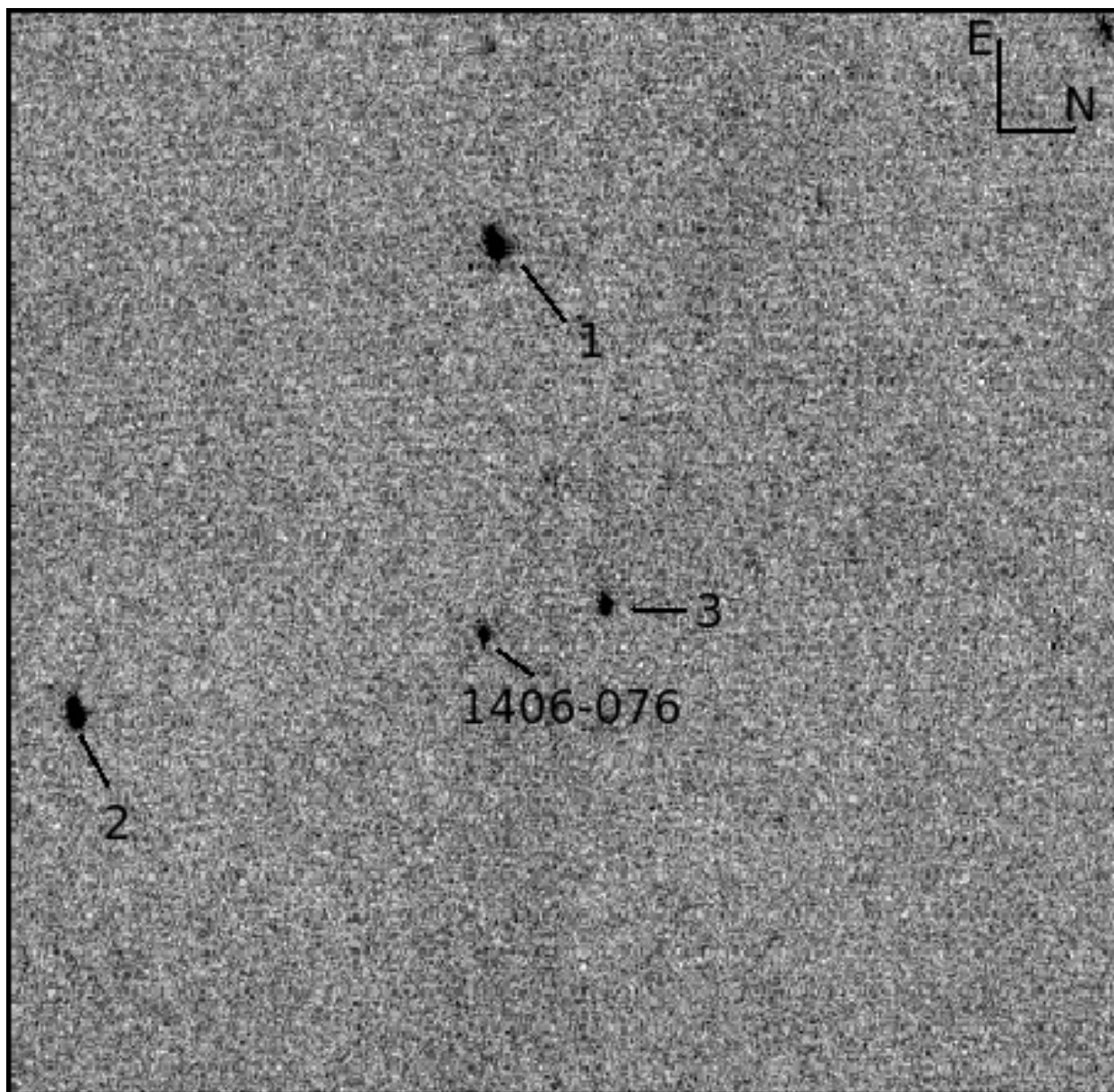
B.4: OJ 287.



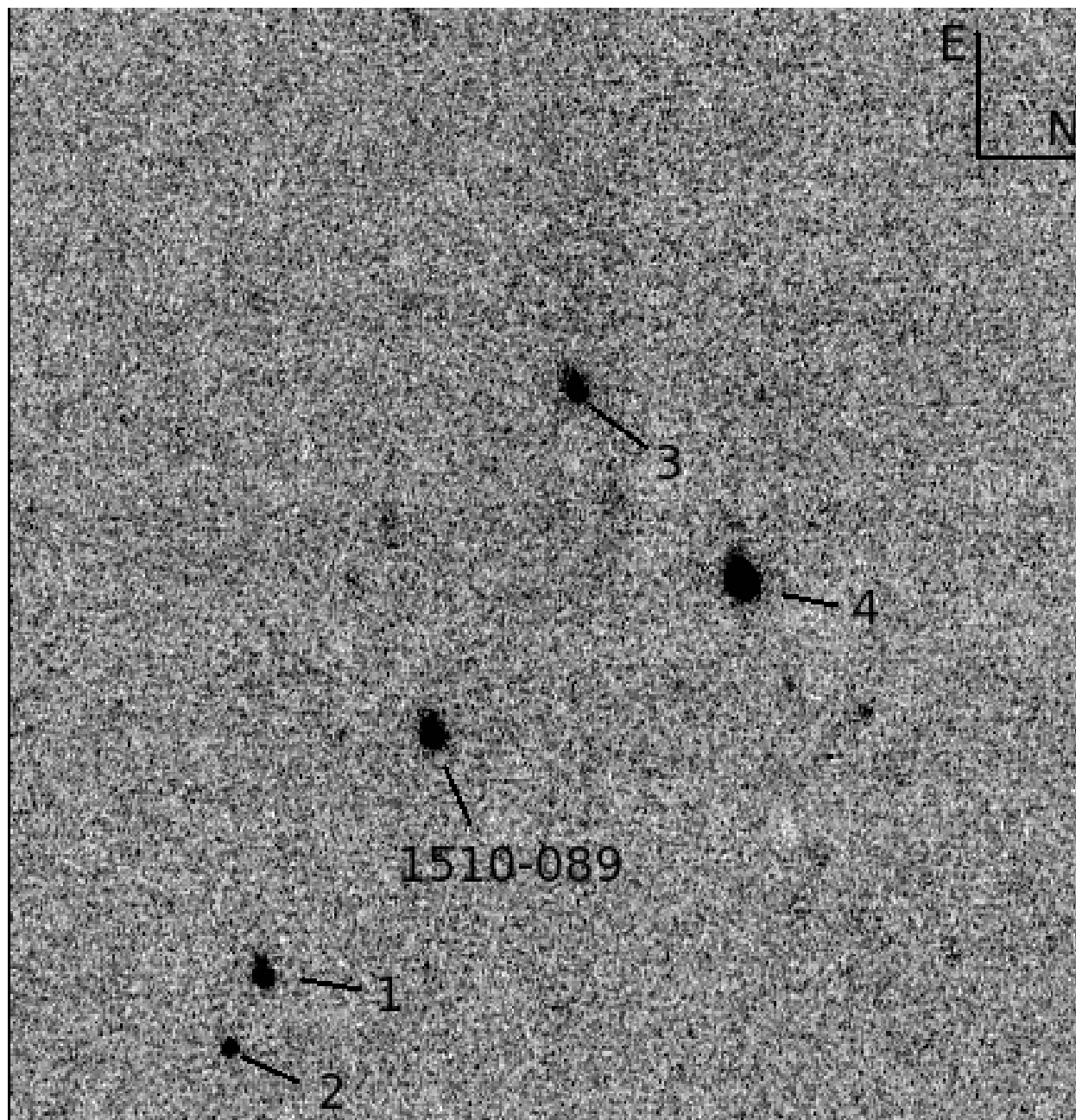
B.5: 3C 273.



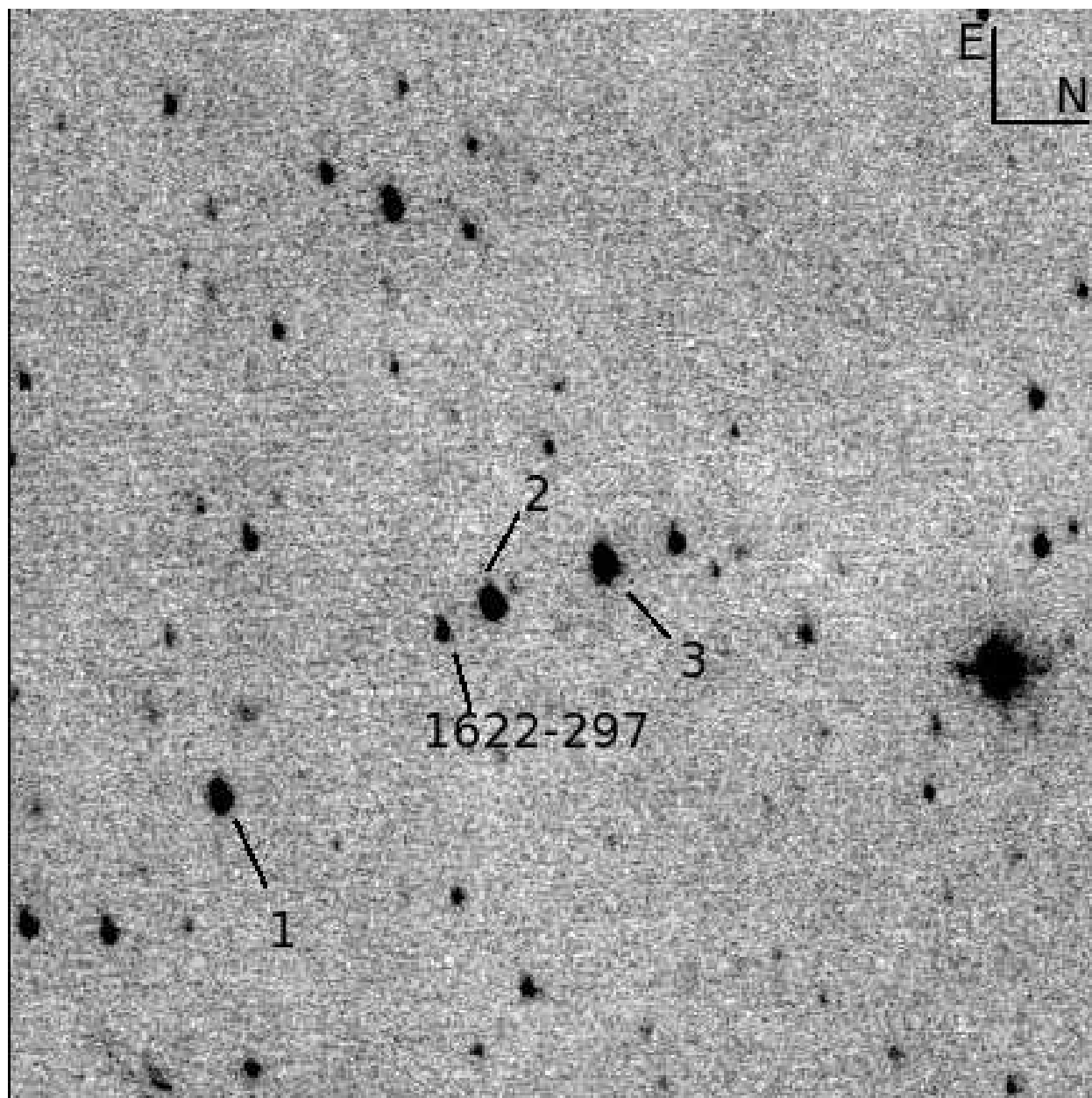
B.6: 3C 279.



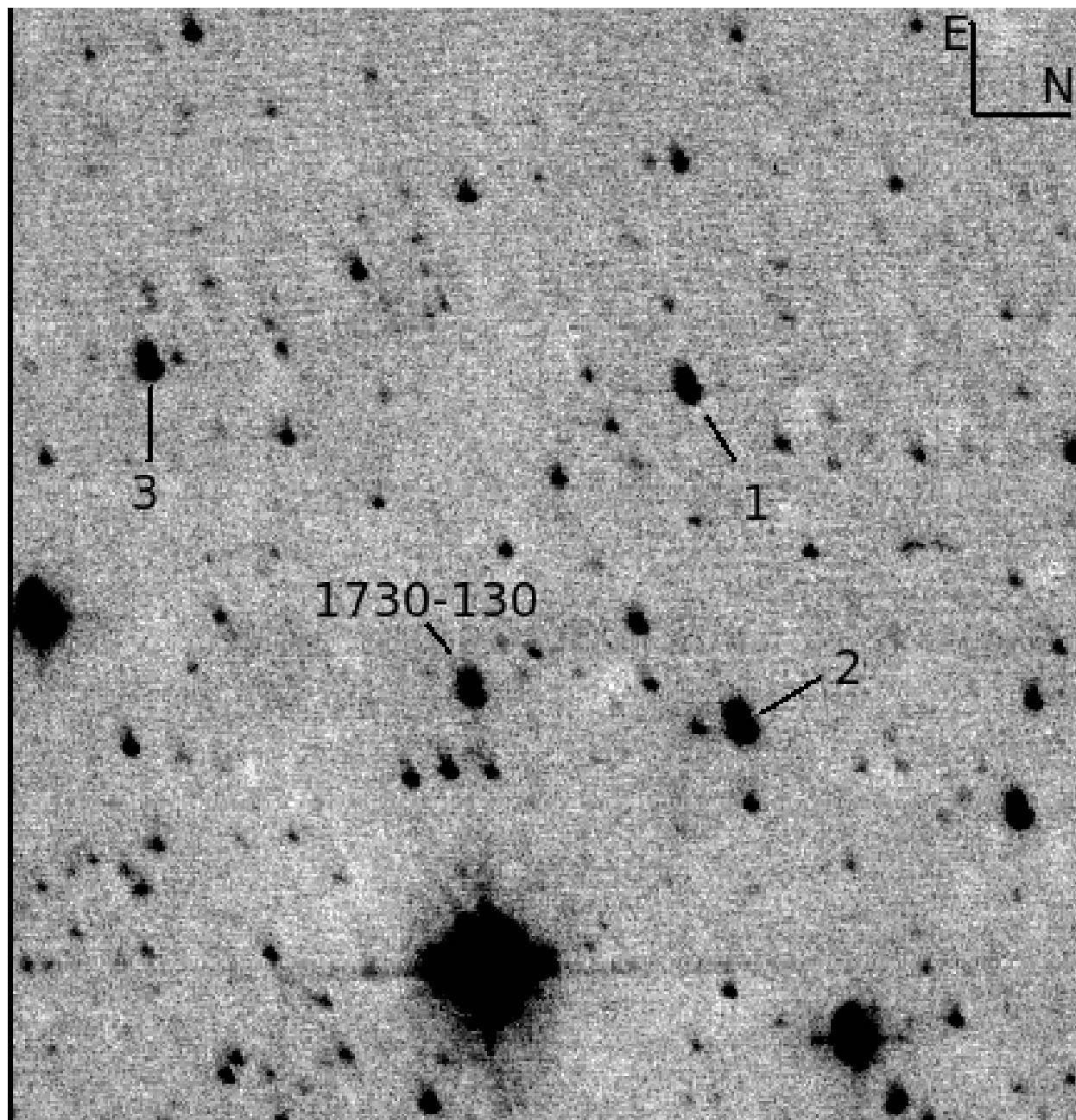
B.7: PKS 1406–076.



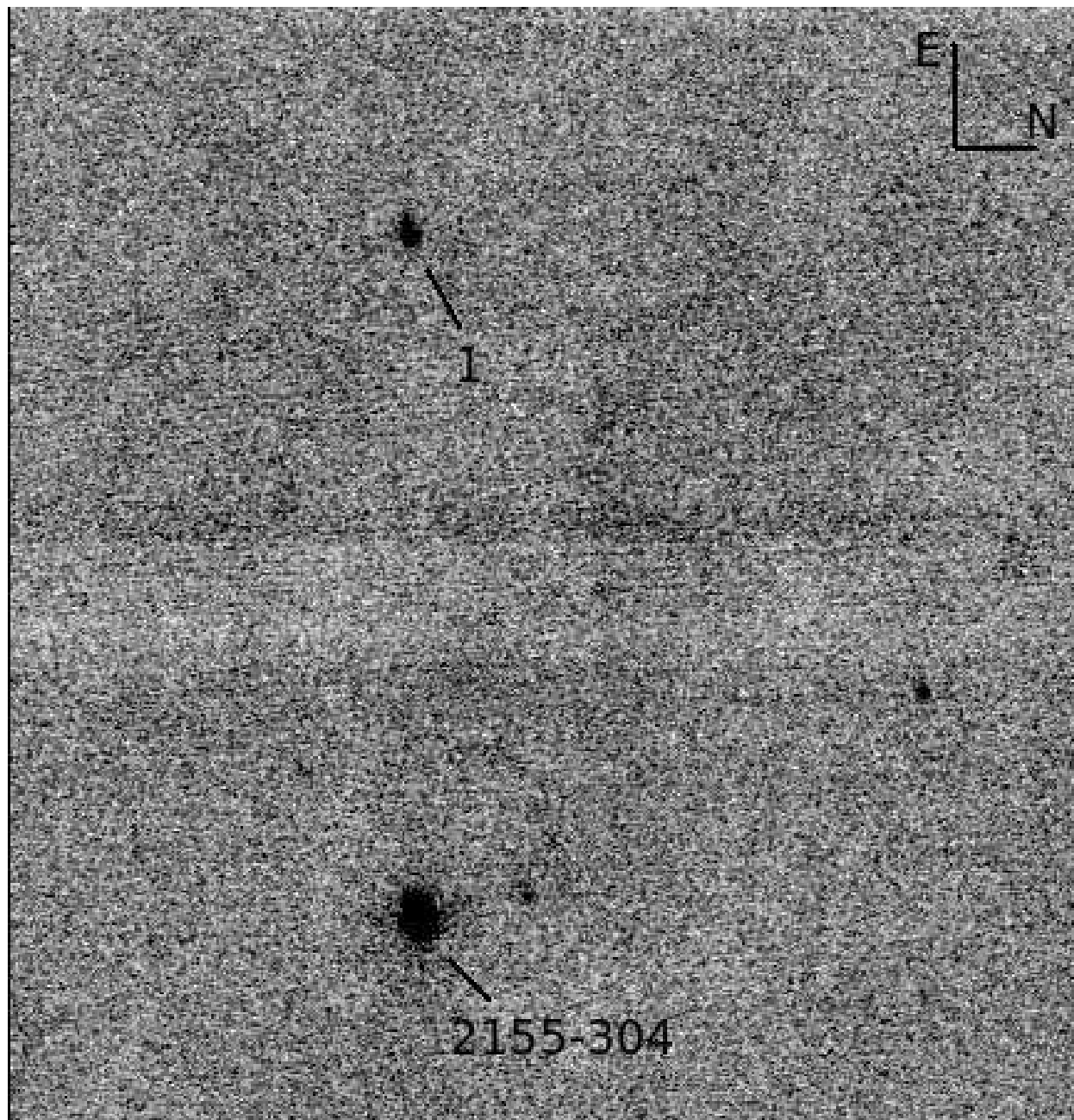
B.8: PKS 1510–089.



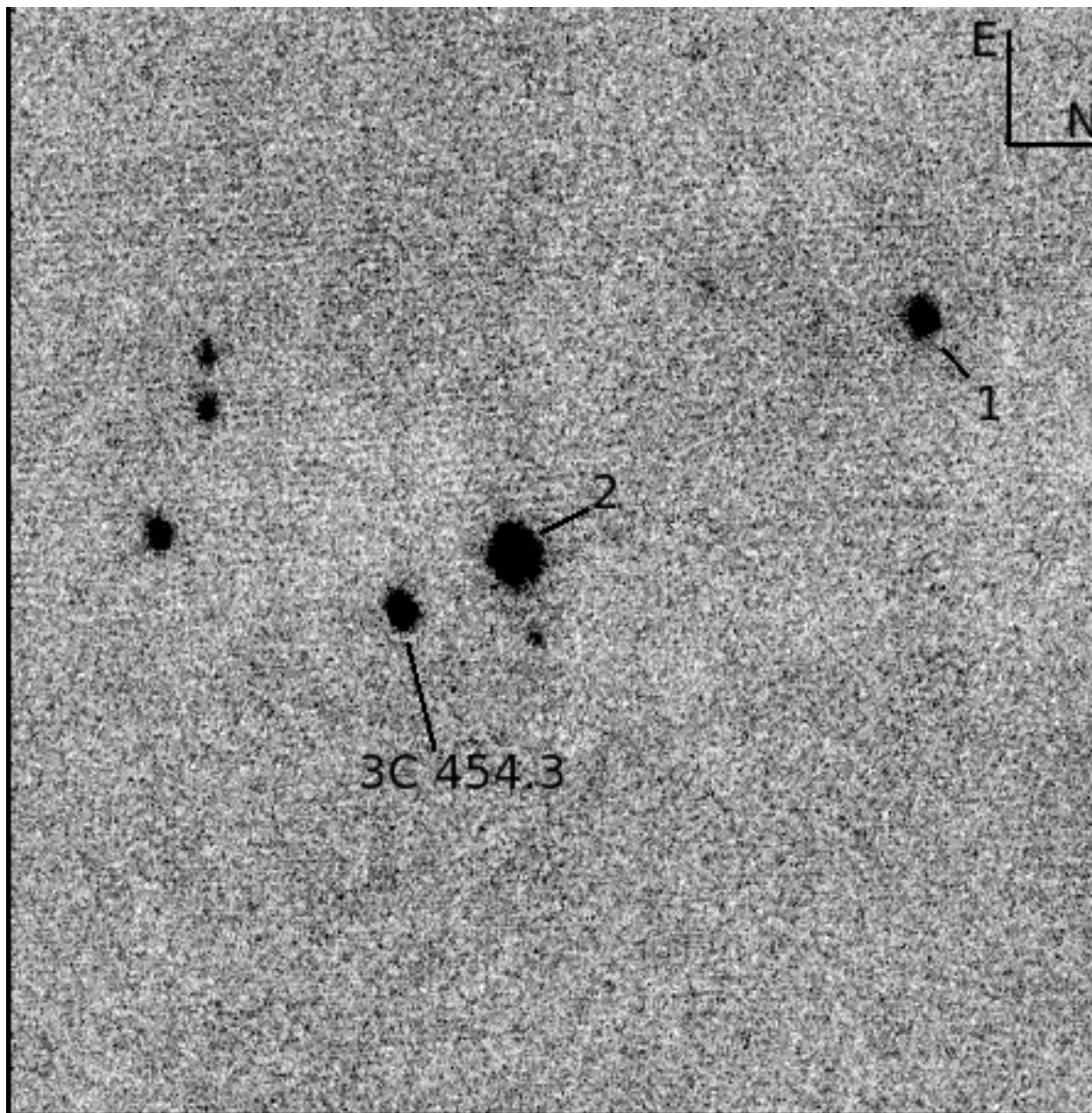
B.9: PKS 1622–297.



B.10: PKS 1730–130.



B.11: PKS 2155–304.



B.12: 3C 454.3.

C. Comparison Star Magnitudes

Here we present calibrated magnitudes for comparison stars indicated in the finding charts presented in Appendixes A and B used as secondary standards for our differential photometry.

The error in calibrating the secondary star magnitudes was found by calculating the $1\text{-}\sigma$ standard error of the mean over the number of photometric nights on which data for the star were taken. Results that were greater than $\pm 3\sigma$ from the mean were rejected and the mean and σ were recalculated. This procedure was repeated until no more rejections were made. The resulting $1\text{-}\sigma$ errors are given in the following tables. Table C.1 gives BVR magnitudes for comparison stars used in optical photometry. Table C.2 gives JK magnitudes for comparison stars used in the infrared photometry.

Table 3:: Comparison star optical magnitudes. Errors are 1- σ .

Source	Star	B	V	R
PKS 0208-512	1	16.43 ± 0.03	15.72 ± 0.03	15.27 ± 0.04
	2	16.90 ± 0.04	16.24 ± 0.04	15.79 ± 0.03
	3	15.43 ± 0.04	14.69 ± 0.03	14.29 ± 0.03
AO 0235+164	1	13.61 ± 0.03	13.05 ± 0.03	12.60 ± 0.02
	2	13.55 ± 0.04	12.75 ± 0.03	12.26 ± 0.03
	3	13.72 ± 0.04	12.98 ± 0.03	12.55 ± 0.03
	4	14.70 ± 0.04	14.05 ± 0.03	13.64 ± 0.03
	5	15.74 ± 0.03	14.80 ± 0.03	14.22 ± 0.03
PKS 0528+134	1	15.90 ± 0.05	14.79 ± 0.03	13.99 ± 0.05
	2	16.81 ± 0.03	15.80 ± 0.03	15.09 ± 0.03
OJ 287	1	15.03 ± 0.05	14.25 ± 0.04	13.69 ± 0.05
	2	15.18 ± 0.04	14.65 ± 0.04	14.26 ± 0.04
	3	15.53 ± 0.05	14.97 ± 0.04	14.55 ± 0.04
	4	16.67 ± 0.05	15.94 ± 0.04	15.43 ± 0.04
3C 273	1	14.14 ± 0.04	13.53 ± 0.04	13.14 ± 0.03
3C 279	1	16.76 ± 0.04	15.92 ± 0.03	15.35 ± 0.03
PKS 1406-076	1	17.67 ± 0.05	16.89 ± 0.03	16.31 ± 0.03
	2	17.96 ± 0.05	17.23 ± 0.04	16.71 ± 0.03
	3	16.55 ± 0.05	15.74 ± 0.03	15.22 ± 0.03
	4	16.04 ± 0.04	15.40 ± 0.05	14.96 ± 0.03
PKS 1510-089	1	13.82 ± 0.04	13.29 ± 0.03	12.96 ± 0.02
	2	15.16 ± 0.05	14.44 ± 0.03	13.98 ± 0.03
	3	15.32 ± 0.04	14.66 ± 0.03	14.24 ± 0.03
	4	15.55 ± 0.04	14.82 ± 0.03	14.36 ± 0.03
	5	16.18 ± 0.04	15.23 ± 0.03	14.59 ± 0.02
PKS 1622-297	1	17.79 ± 0.06	16.66 ± 0.05	16.00 ± 0.03
	2	17.83 ± 0.06	16.68 ± 0.05	15.89 ± 0.05
	3	18.21 ± 0.06	17.06 ± 0.05	16.24 ± 0.04
	4	18.16 ± 0.06	17.04 ± 0.04	16.20 ± 0.03
	5	17.41 ± 0.05	16.59 ± 0.05	16.04 ± 0.03
PKS 1730-130	1	16.11 ± 0.04	14.50 ± 0.03	13.46 ± 0.03
	2	15.71 ± 0.05	14.28 ± 0.03	13.37 ± 0.03
	3	16.83 ± 0.05	15.36 ± 0.03	14.41 ± 0.03
	4	15.76 ± 0.05	14.68 ± 0.03	13.98 ± 0.03
	5	16.60 ± 0.05	15.05 ± 0.04	14.04 ± 0.02
PKS 2155-304	1	15.97 ± 0.03	15.33 ± 0.04	14.94 ± 0.03
3C 454.3	1	16.76 ± 0.05	15.87 ± 0.04	15.29 ± 0.04
	2	15.82 ± 0.05	15.17 ± 0.05	14.74 ± 0.03
	3	16.89 ± 0.05	15.71 ± 0.05	14.92 ± 0.03
	4	14.57 ± 0.05	13.65 ± 0.04	13.09 ± 0.03

Table 4:: Comparison star near-infrared magnitudes. Errors are 1- σ .

Source	Star	J	K
PKS 0208-512	1	12.16 ± 0.04	11.81 ± 0.07
AO 0235+164	1	11.96 ± 0.04	11.68 ± 0.06
	2	12.97 ± 0.04	12.14 ± 0.09
PKS 0528+134	1	14.03 ± 0.08	
	2	12.72 ± 0.06	
	3	12.32 ± 0.05	
OJ 287	1	14.58 ± 0.080	13.79 ± 0.10
3C 273	1	13.64 ± 0.06	
	2	12.29 ± 0.05	
3C 279	1	14.41 ± 0.07	13.86 ± 0.12
	2	15.47 ± 0.14	13.94 ± 0.20
PKS 1406-076	1	15.32 ± 0.07	14.84 ± 0.16
	2	15.77 ± 0.11	15.30 ± 0.47
PKS 1510-089	1	15.61 ± 0.13	14.71 ± 0.27
	2	15.57 ± 0.11	14.44 ± 0.32
	3	13.49 ± 0.05	12.77 ± 0.12
PKS 1622-297	1	14.43 ± 0.11	13.47 ± 0.14
	2	13.83 ± 0.11	12.69 ± 0.12
	3	13.53 ± 0.08	12.67 ± 0.11
PKS 1730-130	1	14.37 ± 0.07	13.17 ± 0.10
	2	13.06 ± 0.07	11.96 ± 0.06
	3	14.60 ± 0.07	13.48 ± 0.10
PKS 2155-304	1	14.30 ± 0.06	13.72 ± 0.14
3C 454.3	1	14.26 ± 0.10	13.49 ± 0.15
	2	11.88 ± 0.07	11.31 ± 0.61

REFERENCES

- Abdo, A. A., Ackermann, M., Ajello, M., Axelsson, M., Baldini, L., Ballet, J., Barbiellini, G., Bastieri, D., Baughman, B. M., Bechtol, K., & et al. 2010, *Nature*, 463, 919
- Agudo, I., Marscher, A. P., Jorstad, S. G., Larionov, V. M., Gómez, J. L., Lähteenmäki, A., Smith, P. S., Nilsson, K., Readhead, A. C. S., Aller, M. F., Heidt, J., Gurwell, M., Thum, C., Wehrle, A. E., Nikolashvili, M. G., Aller, H. D., Benítez, E., Blinov,

- D. A., Hagen-Thorn, V. A., Hiriart, D., Jannuzi, B. T., Joshi, M., Kimeridze, G. N., Kurtanidze, O. M., Kurtanidze, S. O., Lindfors, E., Molina, S. N., Morozova, D. A., Nieppola, E., Olmstead, A. R., Reinthal, R., Roca-Sogorb, M., Schmidt, G. D., Sigua, L. A., Sillanpää, A., Takalo, L., Taylor, B., Tornikoski, M., Troitsky, I. S., Zook, A. C., & Wiesemeyer, H. 2011, *ApJ*, 735, L10+
- Alcock, C., Allsman, R. A., Alves, D. R., Axelrod, T. S., Becker, A. C., Bennett, D. P., Cook, K. H., Dalal, N., Drake, A. J., Freeman, K. C., Geha, M., Griest, K., Lehner, M. J., Marshall, S. L., Minniti, D., Nelson, C. A., Peterson, B. A., Popowski, P., Pratt, M. R., Quinn, P. J., Stubbs, C. W., Sutherland, W., Tomaney, A. B., Vandehei, T., & Welch, D. 2000, *ApJ*, 542, 281
- Angione, R. J. 1971, *AJ*, 76, 412
- Beckwith, S., Evans, II, N. J., Becklin, E. E., & Neugebauer, G. 1976, *ApJ*, 208, 390
- Bessell, M. S., Castelli, F., & Plez, B. 1998, *A&A*, 333, 231
- Bonning, E. W., Bailyn, C., Urry, C. M., Buxton, M., Fossati, G., Maraschi, L., Coppi, P., Scalzo, R., Isler, J., & Kaptur, A. 2009, *ApJ*, 697, L81
- Bonnoli, G., Ghisellini, G., Foschini, L., Tavecchio, F., & Ghirlanda, G. 2011, *MNRAS*, 410, 368
- Böttcher, M. 2007, *Ap&SS*, 309, 95
- Burbidge, E. M., Beaver, E. A., Cohen, R. D., Junkkarinen, V. T., & Lyons, R. W. 1996, *AJ*, 112, 2533
- Cardelli, J. A., Clayton, G. C., & Mathis, J. S. 1989, *ApJ*, 345, 245
- Cohen, R. D., Smith, H. E., Junkkarinen, V. T., & Burbidge, E. M. 1987, *ApJ*, 318, 577
- Coppi, P. S. 1992, *MNRAS*, 258, 657
- DePoy, D. L., Atwood, B., Belville, S. R., Brewer, D. F., Byard, P. L., Gould, A., Mason, J. A., O’Brien, T. P., Pappalardo, D. P., Pogge, R. W., Steinbrecher, D. P., & Teiga, E. J. 2003, in *Society of Photo-Optical Instrumentation Engineers (SPIE) Conference Series*, Vol. 4841, *Society of Photo-Optical Instrumentation Engineers (SPIE) Conference Series*, ed. M. Iye & A. F. M. Moorwood, 827–838
- Dermer, C. D. & Schlickeiser, R. 1993, *ApJ*, 416, 458

- Edelson, R., Turner, T. J., Pounds, K., Vaughan, S., Markowitz, A., Marshall, H., Dobbie, P., & Warwick, R. 2002, *ApJ*, 568, 610
- Edelson, R. A. & Krolik, J. H. 1988, *ApJ*, 333, 646
- Fiorucci, M. & Tosti, G. 1996, *A&AS*, 116, 403
- Fiorucci, M., Tosti, G., & Rizzi, N. 1998, *PASP*, 110, 105
- Fossati, G., Maraschi, L., Celotti, A., Comastri, A., & Ghisellini, G. 1998, *MNRAS*, 299, 433
- Ghisellini, G. & Celotti, A. 2001, *MNRAS*, 327, 739
- Ghisellini, G., Foschini, L., Tavecchio, F., & Pian, E. 2007, *MNRAS*, 382, L82
- Ghisellini, G. & Madau, P. 1996, *MNRAS*, 280, 67
- Ghisellini, G. & Tavecchio, F. 2010, *MNRAS*, 409, L79
- González-Pérez, J. N., Kidger, M. R., & Martín-Luis, F. 2001, *AJ*, 122, 2055
- Hagen-Thorn, V. A., Marchenko, S. G., Takalo, L. O., Sillanpää, A., Pursimo, T., Boltwood, P., Kidger, M., & Gonzalez-Perez, J. N. 1998, *A&AS*, 133, 353
- Hamuy, M. & Maza, J. 1989, *AJ*, 97, 720
- Jones, T. W., O’dell, S. L., & Stein, W. A. 1974, *ApJ*, 188, 353
- Junkkarinen, V. T., Cohen, R. D., Beaver, E. A., Burbidge, E. M., Lyons, R. W., & Madejski, G. 2004, *ApJ*, 614, 658
- Kataoka, J., Takahashi, T., Makino, F., Inoue, S., Madejski, G. M., Tashiro, M., Urry, C. M., & Kubo, H. 2000, *ApJ*, 528, 243
- Konigl, A. 1981, *ApJ*, 243, 700
- Landolt, A. U. 1992, *AJ*, 104, 340
- Lehto, H. J. & Valtonen, M. J. 1996, *ApJ*, 460, 207
- Maccarone, T. J. & Coppi, P. S. 2003, *MNRAS*, 338, 189
- Malkan, M. A. 1983, *ApJ*, 268, 582

- Marscher, A. P., Jorstad, S. G., Larionov, V. M., Aller, M. F., Aller, H. D., Lähteenmäki, A., Agudo, I., Smith, P. S., Gurwell, M., Hagen-Thorn, V. A., Konstantinova, T. S., Larionova, E. G., Larionova, L. V., Melnichuk, D. A., Blinov, D. A., Kopatskaya, E. N., Troitsky, I. S., Tornikoski, M., Hovatta, T., Schmidt, G. D., D’Arcangelo, F. D., Bhattarai, D., Taylor, B., Olmstead, A. R., Manne-Nicholas, E., Roca-Sogorb, M., Gómez, J. L., McHardy, I. M., Kurtanidze, O., Nikolashvili, M. G., Kimeridze, G. N., & Sigua, L. A. 2010, *ApJ*, 710, L126
- Moderski, R., Sikora, M., Coppi, P. S., & Aharonian, F. 2005a, *MNRAS*, 364, 1488
- . 2005b, *MNRAS*, 363, 954
- Monet, D. G., Levine, S. E., Canzian, B., Ables, H. D., Bird, A. R., Dahn, C. C., Guetter, H. H., Harris, H. C., Henden, A. A., Leggett, S. K., Levison, H. F., Luginbuhl, C. B., Martini, J., Monet, A. K. B., Munn, J. A., Pier, J. R., Rhodes, A. R., Riepe, B., Sell, S., Stone, R. C., Vrba, F. J., Walker, R. L., Westerhout, G., Brucato, R. J., Reid, I. N., Schoening, W., Hartley, M., Read, M. A., & Tritton, S. B. 2003, *AJ*, 125, 984
- Mücke, A. & Protheroe, R. J. 2001, *Astroparticle Physics*, 15, 121
- Mücke, A., Protheroe, R. J., Engel, R., Rachen, J. P., & Stanev, T. 2003, *Astroparticle Physics*, 18, 593
- Nandra, K., George, I. M., Mushotzky, R. F., Turner, T. J., & Yaqoob, T. 1997, *ApJ*, 476, 70
- Nilsson, K., Charles, P. A., Pursimo, T., Takalo, L. O., Sillanpää, A., & Teerikorpi, P. 1996, *A&A*, 314, 754
- Persson, S. E., Murphy, D. C., Krzeminski, W., Roth, M., & Rieke, M. J. 1998, *AJ*, 116, 2475
- Pian, E., Vacanti, G., Tagliaferri, G., Ghisellini, G., Maraschi, L., Treves, A., Urry, M., Fiore, F., Giommi, P., Palazzi, E., Chiappetti, L., & Sambruna, R. M. 1998, *ApJ*, 492, L17+
- Raiteri, C. M., Villata, M., Ibrahimov, M. A., Larionov, V. M., Kadler, M., Aller, H. D., Aller, M. F., Kovalev, Y. Y., Lanteri, L., Nilsson, K., Papadakis, I. E., Pursimo, T., Romero, G. E., Teräsranta, H., Tornikoski, M., Arkharov, A. A., Barnaby, D., Berdyugin, A., Böttcher, M., Byckling, K., Carini, M. T., Carosati, D., Cellone, S. A., Ciprini, S., Combi, J. A., Crapanzano, S., Crowe, R., di Paola, A., Dolci, M., Fuhrmann, L., Gu, M., Hagen-Thorn, V. A., Hakala, P., Impellizzeri, V., Jorstad, S.,

- Kerp, J., Kimeridze, G. N., Kovalev, Y. A., Kraus, A., Krichbaum, T. P., Kurtanidze, O. M., Lähteenmäki, A., Lindfors, E., Mingaliev, M. G., Nesci, R., Nikolashvili, M. G., Ohlert, J., Orio, M., Ostorero, L., Pasanen, M., Pati, A., Poteet, C., Ros, E., Ros, J. A., Shastri, P., Sigua, L. A., Sillanpää, A., Smith, N., Takalo, L. O., Tosti, G., Vasileva, A., Wagner, S. J., Walters, R., Webb, J. R., Wills, W., Witzel, A., & Xilouris, E. 2005, *A&A*, 438, 39
- Raiteri, C. M., Villata, M., Lanteri, L., Cavallone, M., & Sobrito, G. 1998, *A&AS*, 130, 495
- Raiteri, C. M., Villata, M., Larionov, V. M., Aller, M. F., Bach, U., Gurwell, M., Kurtanidze, O. M., Lähteenmäki, A., Nilsson, K., Volvach, A., Aller, H. D., Arkharov, A. A., Bachev, R., Berdyugin, A., Böttcher, M., Buemi, C. S., Calcidese, P., Cozzi, E., di Paola, A., Dolci, M., Fan, J. H., Forné, E., Foschini, L., Gupta, A. C., Hagen-Thorn, V. A., Hooks, L., Hovatta, T., Joshi, M., Kadler, M., Kimeridze, G. N., Konstantinova, T. S., Kostov, A., Krichbaum, T. P., Lanteri, L., Larionova, L. V., Lee, C.-U., Leto, P., Lindfors, E., Montagni, F., Nesci, R., Nieppola, E., Nikolashvili, M. G., Ohlert, J., Oksanen, A., Ovcharov, E., Pääkkönen, P., Pasanen, M., Pursimo, T., Ros, J. A., Semkov, E., Sigua, L. A., Smart, R. L., Strigachev, A., Takalo, L. O., Torii, K., Torniainen, I., Tornikoski, M., Trigilio, C., Tsunemi, H., Umana, G., & Valcheva, A. 2008, *A&A*, 480, 339
- Raiteri, C. M., Villata, M., Larionov, V. M., Pursimo, T., Ibrahimov, M. A., Nilsson, K., Aller, M. F., Kurtanidze, O. M., Foschini, L., Ohlert, J., Papadakis, I. E., Sumitomo, N., Volvach, A., Aller, H. D., Arkharov, A. A., Bach, U., Berdyugin, A., Böttcher, M., Buemi, C. S., Calcidese, P., Charlot, P., Delgado Sánchez, A. J., di Paola, A., Djupvik, A. A., Dolci, M., Efimova, N. V., Fan, J. H., Forné, E., Gomez, C. A., Gupta, A. C., Hagen-Thorn, V. A., Hooks, L., Hovatta, T., Ishii, Y., Kamada, M., Konstantinova, T., Kopatskaya, E., Kovalev, Y. A., Kovalev, Y. Y., Lähteenmäki, A., Lanteri, L., Le Campion, J.-F., Lee, C.-U., Leto, P., Lin, H.-C., Lindfors, E., Mingaliev, M. G., Mizoguchi, S., Nicastro, F., Nikolashvili, M. G., Nishiyama, S., Östman, L., Ovcharov, E., Pääkkönen, P., Pasanen, M., Pian, E., Rector, T., Ros, J. A., Sadakane, K., Selj, J. H., Semkov, E., Sharapov, D., Somero, A., Stanev, I., Strigachev, A., Takalo, L., Tanaka, K., Tavani, M., Torniainen, I., Tornikoski, M., Trigilio, C., Umana, G., Vercellone, S., Valcheva, A., Volvach, L., & Yamanaka, M. 2007, *A&A*, 473, 819
- Ramos, E., Kafatos, M., Fruscione, A., Bruhweiler, F. C., McHardy, I. M., Hartman, R. C., Titarchuk, L. G., & von Montigny, C. 1997, *ApJ*, 482, 167
- Remillard, R. A. & McClintock, J. E. 2006, *ARA&A*, 44, 49

- Schlegel, D. J., Finkbeiner, D. P., & Davis, M. 1998, *ApJ*, 500, 525
- Sikora, M., Begelman, M. C., & Rees, M. J. 1994, *ApJ*, 421, 153
- Sikora, M. & Madejski, G. 2000, *ApJ*, 534, 109
- Sillanpaa, A., Haarala, S., Valtonen, M. J., Sundelius, B., & Byrd, G. G. 1988, *ApJ*, 325, 628
- Sillanpaa, A., Takalo, L. O., Pursimo, T., Nilsson, K., Heinamaki, P., Katajainen, S., Pietila, H., Hanski, M., Rekola, R., Kidger, M., Boltwood, P., Turner, G. W., Robertson, J. W., Honeycutt, R. K., Efimov, Y. S., Shakhovskoy, N., Fiorucci, M., Tosti, G., Ghisellini, G., Raiteri, C. M., Villata, M., de Francesco, G., Lanteri, L., Chiaberge, M., Peila, A., & Heidt, J. 1996, *A&A*, 315, L13
- Smith, D. M., Dawson, D. M., & Swank, J. H. 2007, *ApJ*, 669, 1138
- Smith, P. S. & Balonek, T. J. 1998, *PASP*, 110, 1164
- Smith, P. S., Balonek, T. J., Heckert, P. A., Elston, R., & Schmidt, G. D. 1985, *AJ*, 90, 1184
- Sun, W. & Malkan, M. A. 1989, *ApJ*, 346, 68
- Tavecchio, F., Maraschi, L., Sambruna, R. M., & Urry, C. M. 2000, *ApJ*, 544, L23
- Urry, C. M. & Mushotzky, R. F. 1982, *ApJ*, 253, 38
- Urry, C. M. & Padovani, P. 1995, *PASP*, 107, 803
- Vaughan, S., Edelson, R., Warwick, R. S., & Uttley, P. 2003, *MNRAS*, 345, 1271
- Villforth, C., Nilsson, K., Heidt, J., Takalo, L. O., Pursimo, T., Berdyugin, A., Lindfors, E., Pasanen, M., Winiarski, M., Drozd, M., Ogloza, W., Kurpinska-Winiarska, M., Siwak, M., Koziel-Wierzbowska, D., Porowski, C., Kuzmich, A., Krzesinski, J., Kundera, T., Wu, J.-H., Zhou, X., Efimov, Y., Sadakane, K., Kamada, M., Ohlert, J., Hentunen, V.-P., Nissinen, M., Dietrich, M., Assef, R. J., Atlee, D. W., Bird, J., Depoy, D. L., Eastman, J., Peebles, M. S., Prieto, J., Watson, L., Yee, J. C., Liakos, A., Niarchos, P., Gazeas, K., Dogru, S., Donmez, A., Marchev, D., Coggins-Hill, S. A., Mattingly, A., Keel, W. C., Haque, S., Aungwerojwit, A., & Bergvall, N. 2010, *MNRAS*, 402, 2087
- White, R. J. & Peterson, B. M. 1994, *PASP*, 106, 879
- Yanny, B., York, D. G., & Gallagher, J. S. 1989, *ApJ*, 338, 735

